# Electroporation and peripheral nerve stimulation

Borja Mercadal Cavaller

TESI DOCTORAL UPF / 2019

Director:

Dr. Antoni Ivorra Cano

Department of Information and Communication Technologies
Universitat Pompeu Fabra

This work was carried out in the Department of Information and Communication Technologies (DTIC) at Universitat Pompeu Fabra (UPF), Barcelona, Spain.

Borja Mercadal Cavaller was supported by a Predoctoral Research Contract from the DTIC (UPF).

The work done within this thesis was supported by the Ministry of Economy and Competitiveness of Spain (grant TEC2014-52383-C3-2-R) and by the European Research Council (ERC) under the European Union's Horizon 2020 research and innovation programme (grant agreement No 724244).

*A la meva família*

# Acknowledgements

First of all I would like to express my gratitude to my supervisor Dr. Antoni Ivorra for his empathy, patience and his ability to motivate and transmit knowledge. His positive attitude and his faith in my abilities gave me the strength to overcome the obstacles I faced throughout this years. His guidance, wise advice and careful editing have greatly contributed in the production of this thesis.

I would also like to thank all my teammates at the BERG research group for creating a nice working environment and for all the interesting and amusing talks during our breaks. Special thanks to Quim and Laura who have been there since the beginning and whose feedback and advice have been of great help.

My sincere gratitude to Prof. Davalos for allowing me to join his team and spend some time working in their laboratory. Part of the knowledge that I acquired throughout this years and the research that was conducted in this thesis would have not been possible without that opportunity. I would also like to thank all the students in his team, specially Natalie and Kenneth for their help with my experiments and also Daniel, Elisa, Tim, Melvin, Andrea, Temple, Phillip and Nastaran for all the interesting scientific discussions and the funny moments outside the lab. They all made my stay in Virginia very pleasant.

I also have to express my gratitude to the Molecular Physiology lab and the Complex system lab at the PRBB for allowing me to use their equipment. A special mention to Dr. Vicente who introduced my into the *in vitro* experimentation, and Cristina Plata who shared with me her knowledge in cell culture and helped me to quickly learn how to

work at the PRBB facilities. I am also grateful to the staff of the Flow Cytometry unit at the PRBB for their immense knowledge and their willingness to help improving the quality of my experiments.

Finally, I would like to thank all my friends for their support and for helping me to unwind from work, which is necessary but often difficult for those who work in research. Thanks to Ana for making me smile in the bad days and making me put things in perspective in those moments when my self confidence was decaying. She helped me in countless ways along this journey and gave me the courage to continue working hard. Last but not least, thanks to my family for always believing in me and supporting my decisions in life. Also, thanks to my parents for teaching me the importance of knowledge and raising me with a love for science.

# Abstract

Electroporation and electrical stimulation of peripheral nerves are two promising research fields due to their medical applications. This thesis aimed at addressing questions within these fields and, in particular, those that arise from the interaction between the two phenomenona.

There are various studies in the field of electroporation that report results that apparently contradict the common knowledge of the phenomenon. Within this thesis a numerical study was performed to provide a theoretical explanation to those results.

The interaction between electroporation and peripheral nerve stimulation is studied from two different perspectives in this thesis. On the one hand, electroporation can have various direct and indirect effects in the neuronal functions. This thesis explores the possibility that electroporation plays a role in pulsed radiofrequency treatments for chronic pain through an in vitro study. These treatments are routinely used in the clinical practice; however, the exact mechanism of action is unknown. On the other hand, during electroporation based treatments, electrical stimulation of peripheral nerves appears as an unwanted effect causing muscle contractions and acute pain. In the last years it has been shown that this could be mitigated by replacing the commonly used monopolar pulses by bursts of short bipolar pulses. In this thesis, a numerical study was performed in order to provide a better understanding on how bipolar pulses can help mitigating electrical stimulation during electroporation based treatments. Bipolar pulses have been mostly tested in irreversible electroporation, which consists on the use of electroporation for the non thermal ablation of solid tumors. The introduction of a different waveform raises the question of whether or not the cell dead mechanisms remain the same. In this thesis this question was addressed by performing an in vitro study to investigate potential differences in death mechanisms.

Finally, the modeling scheme created previously was expanded to generate a realistic muscle innervation model in order to study the recruitment patterns in intramuscular electrical stimulation.

# Resum

L'electroporació i l'estimulació elèctrica dels nervis perifèrics són dos camps de recerca molt prometedors en quant a les seves aplicacions mèdiques. Aquesta tesi tenia com a objectiu resoldre qüestions en aquests camps i sobretot en concret aquelles qüestions que es deriven de l'interacció entre els dos fènomens.

A la literatura es poden trobar diversos estudis en el camp de l'electroporació que entren en aparent contradicció amb el nostre coneixement del fenòmen. Per tal de donar una explicació aquests resultats es va portar a terme un estudi numèric.

En aquesta tesi, l'interacció entre l'electroporació i l'estimulació dels nervis perifèrics s'estudia des de dues perspectives diferents. Per una banda, l'electroporació pot causar diversos efectes, de forma directa o indirecta, en les funcions neuronals. En aquesta tesi s'explora el possible paper de l'electroporació en els tractaments de radiofreqüència polsada contra el dolor crònic. Aquests tractaments són utilitzats de forma rutinària en l'àmbit mèdic però el seu mecanisme d'acció és actualment desconegut. Per altra banda, durant els tractaments mèdics basats en l'electroporació, com a efecte secundar no desitjat es produeix l'estimulació elèctrica dels nervis perifèrics provocant contraccions musculars i dolor. En els darrers anys s'ha demostrat que es poden mitigar aquests efectes si es fan servir ràfegues de polsos bipolar curts en comptes dels polsos monopolar que típicament s'utilitzen. En aquesta tesi s'ha fet un estudi numèric per tal de proporcionar un marc teòric que expliqui com aquestes ràfegues poden reduir l'estimulació durant els tractaments basats en l'electroporació. Els polsos bipolars han estat utilitzat majoritàriament en tractaments d'electroporació irreversible, que consisteix en l'ús de l'electroporació com a tècnica d'ablació per tractar tumors sòlids. L'ús d'una forma d'ona diferent de les típicament utilitzades planteja l'incògnita de si els mecanismes

de mort cel·lular es mantenen. En aquesta tesi s'ha portat a terme un estudi in vitro per tal d'investigar les potencials diferències en els mecanismes de mort cel·lular degut a la diferent forma d'ona.

Finalment, els models numèrics generats prèviament es van extendre per tal de generar un model neuromuscular realista que permeti simular la resposta del múscul a l'estimulació elèctrica mitjançant elèctrodes intramusculars.

# Contents

# Acronyms and abbreviations

| | |
|---|---|
| ATCC | American Type Culture Collection |
| AC | Alternating current |
| $Ca^{2+}$ | Calcium ion |
| $Cl^{-}$ | Chloride ion |
| ERC | European Research Council |
| DC | Direct current |
| DNA | Deoxyribonucleic acid |
| DTIC | Department of Information and Communication Technologies |
| FEM | Finite element method |
| FES | Functional electrical stimulation |
| H-FIRE | High frequency irreversible electroporation |
| IRE | Irreversible electroporation |
| $K^{+}$ | Potassium ion |
| MU | Motor unit |
| $Na^{+}$ | Soudium ion |
| NMJ | Neuromuscular junction |
| PBS | Phosphate buffered saline |
| PI | Propidium iodide |
| PRF | Pulsed radiofrequency |
| ROI | Region of interest |
| RPA | Relative pore area |
| TMV | Transmembrane voltage |
| UPF | Universitat Pompeu Fabra |

Chapter 1

# Introduction

## 1.1 Introduction

Electric field effects in biological tissues have been an object of study for many years. The interest in this matter emerged in the eighteenth century with the experiments performed by Luigi Galvani [1]. Ever since these experiments our knowledge has largely evolved. Nowadays, the electrical properties of the biological tissues and the cells have been largely characterized and several processes within the human body that rely on electric signals have been described. In addition, multiple effects of the electric fields in biological tissues have been identified and medical applications based on these effects have been developed.

The effects of electric fields in tissues depend on the magnitude of these fields as well as their temporal features (duration and frequency). Setting aside thermal effects due to tissue heating by Joule effect, electric fields can act either in the cellular membrane, in the internal cell structures or in the extracellular environment (electrochemical reactions). In addition, the forces produced by the electric fields may cause movements or deformations of cells. This thesis focuses specifically on effects of the electric fields that happen at the cell membrane.

The exposure of a tissue to an electric field induces a voltage difference across the membranes of the cells. Excitable cells such as the neural cells in peripheral nerves have ion channels embedded in their membranes that are sensitive to this voltage difference. If the voltage difference induced across their membranes exceeds a certain value ($\sim$ 20 mV), an action potential is initiated [2]. This can lead to various effects such as pain sensation or muscle contractions. In fact, the electrical stimulation of peripheral nerves to artificially trigger action potentials has a broad range of applications in medicine such as rehabilitation after an injury or the restoration of the muscle functions [3].

When a tissue is exposed to an electric field with a sufficiently large magnitude, another phenomenon known as electroporation can take place. Similarly to the initiation of action potentials this phenomenon occurs when the voltage difference across the membrane exceeds a certain value (0.2-1 V). Electroporation is characterized by a transient increase in the membrane permeability to ions and macromolecules. This phenomenon is the basis of various medical treatments. On the one hand, the transient permeability increase can be used to to enhance the uptake of chemotherapeutic agents or to introduce DNA into cells. On the other hand, electroporation can result in a loss of

homeostasis causing cell death which can be used as a method to kill cells through a non-thermal electrical mechanism [4].

This thesis focuses on the interaction between the two aforementioned phenomena from two different perspectives. First, the electroporation phenomenon can have multiple effects in the normal functions of excitable cells and second, electrical stimulation of peripheral nerves appears as non-desired effect during electroporation based treatments in medicine.

The generation and conduction of action potentials in excitable cells relies on the selective permeability of their membranes to ions. Thus the non-selective increase in membrane permeability caused by electroporation can block the generation and conduction of action potentials. In addition, the massive ion influx that occurs during this period of increased permeability can lead to longer term effects in the cell functions after the membrane integrity has been restored.

In electroporation based treatments, high voltage pulses are delivered to the tissues in order to produce the desired outcome. The high electric currents that flow through the body during the delivery of these pulses can initiate action potentials in the excitable tissues in the surrounding areas or even in distant locations. Thus, stimulation of peripheral nerves appear as a side effect causing several clinical complications. Ever since the emergence of medical applications of electroporation this has been a concern among researchers and various solutions have been explored [5].

## 1.2 Research goal

The main goal of this thesis is to address questions in the fields of electroporation and peripheral nerve stimulation and, in particular, those questions that arise from the interaction between these two phenomena.

Electroporation is known to cause multiple direct and indirect effects on peripheral nerves. One of the goals of this thesis is to investigate the possible role of electroporation in medical treatments based on the delivery of electric currents. In particular, this thesis aims to study the potential role of electroporation in pulsed radiofrequency for chronic pain, a treatment applied to peripheral nerves and whose mechanism of action is unknown [6].

To overcome the issues related to electrical stimulation during electroporation based treatments, in the last years it has been proposed to change the temporal features of the delivered electric pulses. In the present, this is the approach that has showed the best results, in fact, it was demonstrated that by applying bursts of short bipolar pulses it is possible to minimize muscle contractions while maintaining the treatment efficacy [7]. One of the goals of this thesis is to analyze the rationale of such approach and its implications.

## 1.3 Dissertation outline

Chapter 2 provides an overview of the two phenomenona that are the center of this thesis. Namely, electroporation and peripheral nerve stimulation. It is intended to help understanding the work that has been done within this thesis and its significance.

The work detailed in Chapter 3 was motivated by the discovery of various studies reporting results that were in apparent contradiction with a common belief within the field of electroporation. This chapter presents a theoretical study that provides an explanation to those experiments.

Pulsed radiofrequency treatments for chronic pain are routinely used in the clinical practice, however, the mechanism of action of these treatments is currently unknown. Chapter 4 explores the possible role of electroporation in these treatments. Specifically, it describes a series of *in vitro* experiments that were performed to study the possible participation of electroporation in the effects of the treatment that have been reported in the literature.

Chapters 5 and 6 focus on the use of bipolar pulses for irreversible electroporation treatments. Chapter 5 presents a numerical modeling study that provides a theoretical framework to understand how bipolar pulses can help minimizing neurostimulation during irreversible electroporation treatments. Then, Chapter 6 discusses the potential differences on cell death dynamics and mechanisms between conventional irreversible electroporation treatments and treatments using bipolar pulses. This is done on the basis of an *in vitro* study.

The modeling framework generated in Chapter 5 is further extended in Chapter 7 in order to develop a suitable modeling scheme to simulate intramuscular electrical stimulation.

Finally, Chapter 8 overviews the main conclusions that can be extracted from this thesis and discusses the future directions concerning the research done.

Chapter 2

# Background

## 2.1 Electric fields in biological tissues: basic concepts

When a voltage difference between two points of a material is applied it induces an electric field. If the material contains charges that are free to move, the electric field causes a flow of electric charges between the points where the potential difference has been applied (i.e. electric current). In aqueous solutions the charges that are free to move are the ions dissolved in them. Thus, the electric current in aqueous solutions implies the transport of charged atoms and small molecules.

Biological tissues are highly complex structures, however, from an electrical perspective they can be simplified as a group of cells embedded in an aqueous solution. In addition, cells can be regarded as a thin membrane enclosing another aqueous solution. The aqueous solution surrounding the cells (i.e. extracellular medium) mostly contains sodium ($Na^+$) and chloride ($Cl^-$) ions whereas the solution inside the cell (i.e. intracellular medium) mostly contains potassium ions ($K^+$). The cell membrane, in contrast, consists mostly of phospholipids that are arranged in two layers oriented opposite to each other forming what is known as the lipid bilayer. The lipid bilayer although is partially permeable to ions and water molecules, is almost impermeable to most ions. In fact, these characteristics of the membrane are essential in maintaining cell homeostasis [8].

Taking into account the aforementioned, the cell and its surrounding environment can be modeled by representing the cell membrane as a dielectric layer and the intracellular and extracellular media as conductive materials. This model was proposed by Fricke in 1925 [9] and is still considered to be a good approximation of the passive electrical properties of a single cell for frequencies up to several megahertz. According to this model, every infinitesimal portion of the intracellular and extracellular mediums act as a resistor and every infinitesimal portion of the cell membrane acts as a capacitor.

In normal conditions the extracellular medium contains slightly more positive ions than the intracellular medium creating a voltage difference between both sides of the membrane. This transmembrane voltage (TMV) is usually referred to as the resting TMV of the cell. When a cell is exposed to an electric field, ions of opposite sign in intracellular and extracellular media accumulate at both sides of the membrane until an equilibrium is reached, usually after a short time period($\approx 1\mu s$). This accumulation of charges generates a TMV that

is added to the resting TMV.

For simple cell geometries and uniform electric fields, it is possible to calculate the induced TMV analytically. For instance, in the case of a spherical cell with radius $r$, and treating the membrane as a perfect insulator, the induced TMV at each point along the membrane can be calculated by Schwann's equation [10]:

$$TMV = \frac{3}{2}|E_{ext}|r\cos\theta \tag{2.1}$$

where $|E_{ext}|$ is the electric field, and $\theta$ is the angle between the electric field direction and the direction defined by the center of the sphere and the point in the membrane at which the voltage is calculated (see Figure 2.1). Note that the TMV is not uniform along the membrane, it will be maximum in the areas where $\theta \approx 0$ and zero in the areas where $\theta \approx \pm\pi$.

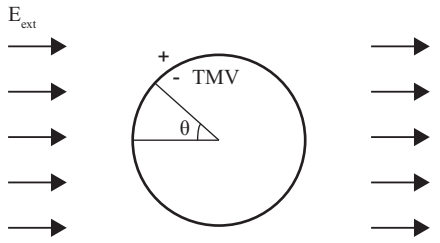


**Figure 2.1:** An external electric field induces a TMV.

Eq. 2.1 can provide an approximation of the TMV induced in cells in suspension as they tend to have round shapes and other spheriodal geometries can be solved analytically [11] as well. Adhered cells or cells inside tissues tend to have much more complex geometries. In those cases, numerical methods such as the finite elements method (FEM) can be used to calculate the induced TMV [12].

When a tissue, or multiple cells in an *in vitro* experiment are exposed to an electric field, the induced TMV on each cell depends on its shape and orientation relative to the electric field. In addition, the electric field is distorted around cells, which is particularly relevant in tissues as the space between cells is very small. Thus, in practice, calculating the induced TMV is either not possible (due to the lack of knowledge on the cell shapes and orientations) or requires a tedious process. For this reason, when dealing with effects that are known to depend on the TMV, either at a tissue level or with multiple cells *in vitro*, these

effects are systematically studied using the macroscopic electric field as a reference.

## 2.2 Electroporation

### 2.2.1 Overview

Electroporation is a biophysical phenomenon in which the cell membrane, when exposed to high electric fields, increases its permeability to ions and macromolecules. Electroporation is usually induced by exposing cells to short (from a few nanoseconds to a few milliseconds) electric field pulses in order to avoid thermal damage to the cellular structures due to Joule heating. The effects of electroporation can be transient (reversible electroporation) and the membrane can recover its integrity. After that, cell can recover homeostasis and its viability is not compromised. On the other hand, depending on the magnitude of the field, the duration of pulses, the number of pulses, and to a lesser extent, the pulse repetition frequency, electroporation can result in cell death (irreversible electroporation). This cell death can be either a consequence of a permanent damage to the membrane or due to the inability of the cell to recover homeostasis after membrane integrity has been restored [13].

Although scientific descriptions of the phenomenon can be identified in reports from the 18th century[14], the first scientific report that linked the observed effects of high intensity electric fields with an electric breakdown of the cell membrane was published by Stämpfli and Willi in 1957 [15]. One year later, Stämpfli also showed that this breakdown could be either reversible or irreversible under certain conditions [16]. A few years later, in 1967, Sale and Hamilton published a series of seminal papers that set the basis for many future studies [17–19]. By studying the bactericidal effect of short DC pulses, they showed that pulsed electric fields killed the cells through the irreversible loss of membrane integrity. In addition, they linked this effect with the TMV induced by the electric fields. A few years later, Neumann and Rosenheck showed that electric field pulses could transiently increase the permeability of vesicle membranes [20]. Five years later, in 1977, Kinosita and Tsong proposed for the first time that membrane permeabilization was due to the creation of small pores in the membrane [21]. At this point the interest in the phenomenon had growth, and a few years later, in 1982, Neumann and his colleagues coined the term electroporation in a study that demonstrated the in-

troduction of genes into cells by means of electroporation [22]. These studies from the late 70's and begining of the 80's raised a great interest and the knowledge on the phenomenon as well as the number of applications have been growing until nowadays.

As we stated previously, quite early electroporation was linked to the induced TMV in the cells. Nowadays it is widely accepted that in order to trigger electroporation, the TMV induced by an external electric field has to reach a certain threshold. Indeed, there are several evidences supporting that [23–28]. The value of this threshold depends on multiple factors such as the characteristics of the pulse or the detection method. In general values between 200 mV and 1 V are reported [29].

### 2.2.2 Electroporation dynamics

In the last decades there have been several advances in the understanding of the electroporation phenomenon. Nevertheless the mechanisms involved in the whole process are yet not clear. This section summarizes the observed dynamics of the phenomenon and the current theoretical framework to explain them (see Figure 2.2).

First, after the pulse onset and once the TMV reaches the threshold value, electroporation occurs in a few nanoseconds and membrane conductivity rapidly increases [30–32]. It is thought that this initial and rapid increase in membrane conductivity is due to the formation of hydrophobic pores in the lipid bilayer that create new conductive paths across the membrane. This hypothesis is supported by molecular dynamics simulations [33, 34].

Second, the sudden and rapid increase in conductivity is followed by a slower and mild increase during the rest of the pulse [25, 35]. Recent studies suggest that at least two dynamics occur during the pulse that lead to the formation of two different defects in the membrane [36–42]. First the aforementioned population of conductive hydrophobic pores is created. Second, a given fraction of these pores transitions into a more stable lipid organization generating a second population of membrane defects. The nature of these defects is yet not clear neither its relation with the conductive hydrophobic pores. It is believed that some of the hydrophobic pores transition into more stable hydrophilic pores that can expand [43]. Another hypothesis is that there is an oxidation of the lipids in the membrane increasing its fluidity [44].

After the pulse two distinct phases can be identified: first, a sudden

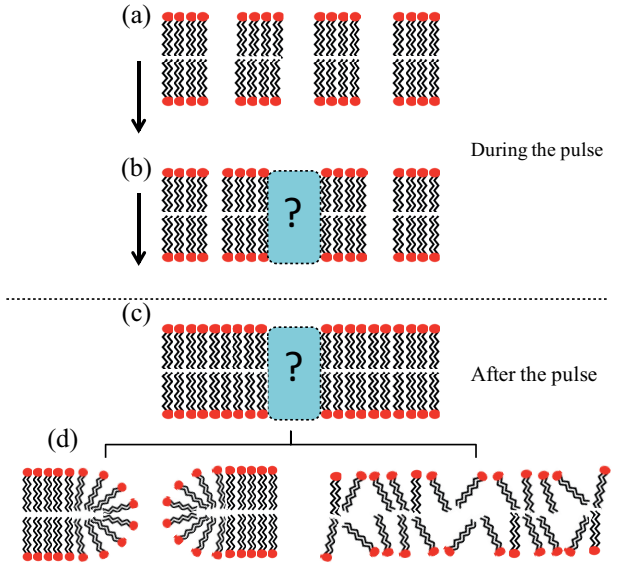


**Figure 2.2:** Current model of the electroporation phenomenon dynamics. (a) A few nanoseconds after the pulse onset a large number of hydrophobic pores are created in the membrane and the membrane becomes highly conductive. (b) Some of the hydrophobic pores suffer a structural change creating stable defects in the membrane (represented with a ?) (c) After the pulse, hydrophobic pores shrink in a matter of microseconds (or very few milliseconds) while stable defects remain in the membrane. Membrane conductivity has decreased significantly compared to its levels during the pulse although the membrane permeability is still significantly altered. (d) Two hypotheses for the nature of the stable defects: stable hydrophilic pores associated with a reorganization of the lipids (left); disorganization and alteration of the lipids (maybe oxidation) (right). These stable defects diffuse along the membrane homogenizing the permeability of the membrane; membrane recovers its initial conditions after several seconds or minutes, probably through active biological processes.

decrease in membrane conductivity during the first microseconds or very few milliseconds after the pulse [24, 35, 37, 38, 45]. It is suggested that this first stage of membrane recovery is completely passive and is due to the shrinkage of the conductive hydrophobic pores, which is consistent with molecular dynamics simulations [34, 46]. The initial sudden decrease is followed by one or more slower phases that tend to return to the initial membrane conductivity before electroporation. Studies based on the cell uptake of ions or molecules report that the membrane permeability stays altered for a period of time that ranges from several seconds [45, 47, 48] to a few minutes [21, 49, 50]. This suggests that the second population of defects is the one that plays a major role in the transmembrane transport of ions and molecules due to electroporation. In fact, most of this transport takes place after the

pulse [45, 51–54]. The processes occurring during this second phase of the membrane recovery are believed to be: first, a re-organization of the stable defects driven by diffusion along the membrane [39], and second, active biological processes.

### 2.2.3 Electroporation detection methods

The small scale of the phenomenon and its fast dynamics make it extremely challenging to perform direct measurements of electroporation. For this reason electroporation experiments are based on indirect measures of its effects.

Some of the most common methods to assess electroporation *in vitro* rely on the detection of transport through the membrane of ions or molecules that are impermeant in normal conditions. Fluorescent probes such as Propidium Iodide (PI) are commonly used to detect membrane permeabilization by measuring cell fluorescence with imaging techniques. Similarly, fluorescent ion indicators are used to monitor the intracellular concentration of a specific ion in order to detect an influx or an efflux through the membrane. Besides fluorescent markers, cytotoxic agents that in normal conditions cannot enter the cell are sometimes used to detect electroporation by the assessment of the cell viability [55].

Another method to detect electroporation is based on the membrane conductivity changes. Electrical impedance measurements can be used to monitor these changes and detect electroporation. During the application of electroporation pulses, the membrane conductivity changes can be estimated by measuring the current-voltage relation. In addition, by applying alternating currents, impedance measurements at single frequencies can be made before and after the electroporation pulses to evaluate the changes in the impedance spectrum [56].

Finally, patch clamp techniques can provide direct measurements of the current across the membrane. This techniques are routinely used in electrophysiology to study the membrane currents through ion channels. In electroporation, patch clamp can be used to detect membrane conductivity changes in a single cell from the current-voltage recordings [57].

### 2.2.4 Medical applications of electroporation

Various medical applications of electroporation exist nowadays. On the one hand, reversible electroporation is used to enhance the cellular

uptake of chemotherapeutic agents and as a transfection mechanism by facilitating the introduction of genes into the cytoplasm. On the other hand, irreversible electroporation (IRE) is used as a non thermal ablation technique for the treatment of solid tumors. This section provides a brief overview of these treatments.

### Electrochemotherapy

Electrochemotherapy relies on electroporation to introduce chemotherapeutic agents into the cells [58, 59]. Drugs that can hardly penetrate into the cell such as Bleomycin or Cysplatin are infused either locally or systemically and electroporation is induced in the area of tissue being treated. Electrochemotherapy has proved to be safe and effective [60, 61] and after the publication of the standard operating procedures [62] electrochemotherapy was widely accepted in Europe. Only in 2012 more than 3,000 patients were treated with electrochemotherapy the European Union in 2012 [63].

### Non-thermal Tissue Ablation

In 2005 Davalos and colleagues proposed the use of irreversible electroporation for the non-thermal ablation of solid tumors [64] and their theoretical predictions were later confirmed in animal studies [65, 66]. IRE kills the cells within a tissue while the extracellular matrix remains intact [67]. This offers several advantages compared to other ablation techniques that rely on temperature changes. It has been shown that due to the non-thermal nature of IRE treatments, vital structures such as large blood vessels and bile ducts are preserved within the ablated regions in liver [65, 68] and in prostate [69, 70]. In addition, the preservation of the tissue architecture and its vasculature can accelerate post-treatment healing [66]. Various clinical trials on the use of IRE as an ablation technique have been performed [71] and in the present there are 80 ongoing clinical trials (clinicaltrials.gov).

### Gene threapy

After the first report on gene transfection by means of electroporation [22] it became a widely used technique for *in vitro* experimentation. In medicine, it has been tested clinically as a cancer treatment in melanomas[72] or prostate cancer [73] among others. It is also used as an alternative to viral methods to increase the transfection efficiency in DNA vaccination [74]. DNA vaccination is being tested against infectious diseases and as a regenerative therapy [4].

## 2.3 Electrical stimulation of peripheral nerves

### 2.3.1 Overview

Peripheral nerves are the structures that connect the central nervous system with the peripheral organs or muscles. The communication between the central nervous system and the peripheral organs through the peripheral nervous system enables the body to perform many functions: 1) The information from the sensory receptors is transmitted to the central nervous system can be eventually transduced into sensations. 2)The connection with the central nervous system allows the regulation of the skeletal muscle contractions, which makes possible the controlled movement of the body. 3)Communication between the central nervous system and the smooth muscles of the internal organs allows the central nervous system interfering in the functioning of these organs. 4)The central nervous system can control some glands of the body through the peripheral nervous system by regulating their secretion [75].

The transmission of information through the peripheral nervous system relies on the conduction of electric signals within the nerves. These electric signals can be artificially initiated under the action of an external electric field, which implies that we can act on peripheral nerves to produce a response in the body. In fact, there are medical applications that use electrical stimulation of peripheral nerves for different purposes such as rehabilitation after a stroke [3] or restoration of muscle functions after a spinal cord injury [76].

### 2.3.2 Excitable cells

When the cell membrane was introduced in section 2.1, it was only mentioned the lipid bilayer. However, embedded in this thin layer there are a large number of proteins and molecules that play a key role in maintaining the cell homeostasis. Among these proteins, the ion channels are complex structures that can change its conformation allowing diffusion of ions across the membrane. Several types of ion channels have been identified with different degrees of selectivity. While some of them allow the diffusion of any ion, others have a high selectivity and are only permeable to a specific ion and impermeable to the rest. The activation or inactivation of ion channels can be driven by a wide range of internal and external stimulus such as elec-

trical, chemical or mechanical; and ion channels are usually classified depending on the stimulus that activates them [77].

The transport through ion channels is completely passive, which means that it is only driven by the concentration gradient between the intracellular and the extracellular media. However, other types of proteins can be found in the membrane that involve the active transport of ions. These proteins are known as ion pumps and allow the exchange of ions between the intracellular and the extracellular media against the concentration gradient.

Ion channels and ion pumps are crucial in the function of excitable cells. The membranes of excitable cells contain a family of ion channels whose activation is driven by the TMV, the voltage gated ion channels. These channels confer excitable cells the ability to generate and propagate electrical impulses and makes them susceptible to be excited by an external electrical stimulus. Examples of excitable cells are neurons and muscle cells.

### 2.3.3 Action potentials

The generation and propagation of electric signals in excitable cells takes place through a process called action potential. Within this process $Na^+$ and $K^+$ ions play a key role as well as its associated voltage gated ion channels and ion pumps. Action potentials consist in a rapid increase in the TMV (depolarization) followed by a decrease that tends to return the TMV to its initial value (repolarization).

Action potentials are triggered when there is a depolarization that increases the TMV above a certain threshold. This depolarization can be caused by an external stimulus or by the depolarization of a nearby patch of membrane. Indeed, the electric signals propagate along the membrane because once an action potential is initiated in a localized patch of the membrane, the depolarization acts as a stimulus for the nearby areas of the membrane [2].

The stages of an action potential are as follow (see also Figure 2.3):

- Resting state. In the absence of any alteration or stimulus excitable cells have a constant TMV (resting voltage), that depends on the intracellular and extracellular ionic concentrations as well as their permeabilities through the membrane.
- Depolarization. Once the membrane is depolarized above the threshold and an action potential is initiated, membrane perme-

ability to $Na^+$ rapidly increases (opening of the sodium channels) allowing a large number of $Na^+$ to enter the cell. This generates a positive feedback effect: the entry of $Na^+$ raises the TMV and at the same time, an increase in the TMV causes more channels to open, thus, further increasing the influx.

- Repolarization. Once the TMV reaches the peak of the action potential, sodium channels begin to close while at the same time, potassium channels — which need a larger time to open — are still opening. Therefore, the positive feedback of the depolarization stage is stopped and there is an efflux of $K^+$ ions to the extracellular medium that causes a decrease in the TMV, returning it to the initial resting value.

- Refractory period. After an action potential, there is a period of time in which it is impossible to generate an action potential (absolute refractory period) followed by a period in which a larger stimulus than usual is required to generate an action potential (relative refractory period).

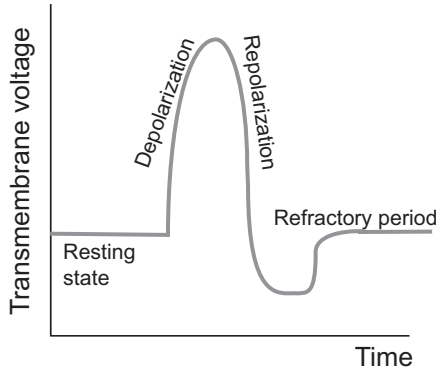


**Figure 2.3:** Typical time course of the TMV during an action potential

The absolute refractory period is originated by a peculiarity of the sodium channels, which is that, besides the resting and the active states, these channels have an inactive state in which they cannot be activated by a depolarization. On the other hand, the relative refractory period is related to a delay in the closure of the potassium channels in combination with a delay of the sodium channels to return

to their resting state. During this period, some potassium channels remain open and some sodium channels remain inactive which causes that a larger stimulus is required in order to depolarize the membrane to the threshold voltage.

Finally, it is worth mentioning the important role of the ion pumps in the normal function of excitable cells. Action potential generation is based on the diffusion of $Na^+$ and $K^+$ through the cell membrane. This disturbs the concentration gradients of these ions which can result in a cell homeostasis loss. At this point, the active transport through the ion pumps come into play by restoring the initial concentration gradient.

### 2.3.4 Neurons in peripheral nerves

In the peripheral nervous system information is transmitted by the propagation of action potentials through the neurons that are contained in the nerves. The main parts of a typical neuron are depicted in Figure 2.4. The cell body of a neuron (soma) is connected to two different types of thin fibers, the dendrites and the axon. While the diameters of the cell body, the dendrites and the axon are typically in the order of ten micrometers, the lengths of the axon and the dendrites can be over one meter in the peripheral nerves.

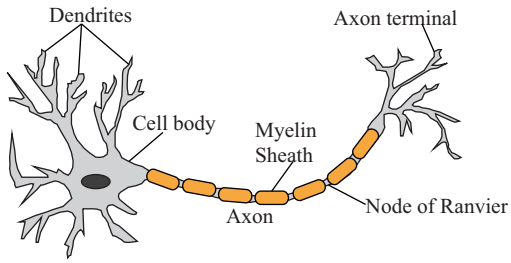


**Figure 2.4:** Schematic of a myelinated neuron

Neurons can receive signals from an organ, a muscle, another neuron or the central nervous system. This signals are received by the dendrites and generate an action potential that propagates along the axon whose termination is divided in several terminals which can transmit this signal again to an organ, another neuron or to the central nervous system (depending on the function of each particular neuron). The transmission of these signals takes place by a chemical process in which a neurotransmitter is released by one cell causing a depolar-

ization in the other cell. The gaps between cells where this process occurs are called synapses.

Neurons can be classified based on different criteria such as the direction in which they transmit the information, histologically or based on their size and conduction velocity.

Depending on the direction in which they transmit the electric signals, neurons can be classified as efferent or afferent. Efferent neurons transmit signals from the central nervous system to the peripheral organs or muscles. They are also referred as motor neurons because the signals they transmit are mainly intended to control the contraction of a muscle. Afferent neurons carry information from the tissues and organs to the central nervous system. They are also referred as sensory neurons because most of them are dedicated to receive the information from sensory receptors and deliver this information to the central nervous system.

Inside peripheral nerves usually travel a combination of axons (from efferent neurons) and dendrites (from afferent neurons) (Figure 2.5). For this reason, the term nerve fibers is commonly used to refer to both. Nerve fibers can be classified histologically as myelinated or unmyelinated depending on whether they are covered by myelin sheaths or not. The gaps between two myelin sheaths are called Nodes of Ranvier. Due to the electrical properties of myelin (highly insulating), the action potential propagation is significantly different between myelinated and unmyelinated neurons. While in unmyelinated axons the conduction is continuous along the membrane, in myelinated axons the electric signal propagates from one node to the next.

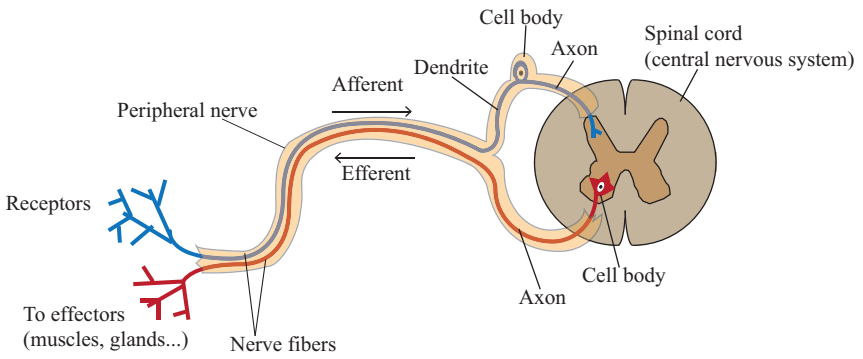


**Figure 2.5:** Peripheral nervous system.

Finally, a common classification criteria of nerve fibers is based on the diameter and the conduction velocity. This is known as the Erlanger-Gasser classification, named after the scientists who conceived it [78–80]. This classification is not ideal as recognized by one of its creators [81], however, nowadays it is universally used in the literature. The most common fiber types that can be found in peripheral nerves according to this classification are listed in Table 2.1.

**Table 2.1:** Some of the fiber types in the Erlanger-Gasser classification[82].

| Fiber type | Relative diameter/ myelination | Conduction | Function/examples |
|---|---|---|---|
| A-$\alpha$ | Large/myelinated | Fast | Motor neurons |
| A-$\beta$ | Medium/myelinated | Moderate | Touch, pressure |
| A-$\delta$ | Small/myelinated | Moderate | Fast pain, cold |
| C | Small/unmyelinated | Slow | Pain, temperature, mechanoreception |

### 2.3.5 Mathematical models for electrical stimulation

The first recording of an action potential was accomplished by Hodgkin and Huxley in 1939 [83]. Their research on the conduction and propagation of electric signals in nerves culminated with the first mathematical model of electrical stimulation of neurons[84]. In this seminal paper the authors provided a set of differential equations to describe the dynamics of the ion channels and the TMV. They modeled the current across the membrane as a parallel combination of a capacitive current, a $Na^+$ current, a $K^+$ current and a leak current (see Figure 2.6). The variable resistances $R_{Na}$ and $R_K$ depend on the number of $Na^+$ and $K^+$ channels that are open and the voltages sources $E_K$, $E_Na$ and $E_{Lk}$ are the ionic Nernst potentials that depend on the intracellular and extracellular concentration of each ion. More sophisticated neuronal models have been developed after Hodgkin and Huxley [85–87], however, the mathematical framework proposed by them is still being used nowadays.

Although the Hodgin and Huxley model provides a framework to model the membranes of excitable cells it is very limited to model external electrical stimulation. Nowadays most of the numerical models for external electrical stimulation are based on the work by Rall [88]. In the peripheral nervous system, action potentials are generated in very thin and long structures (either axons or dendrites). Thus, ex-

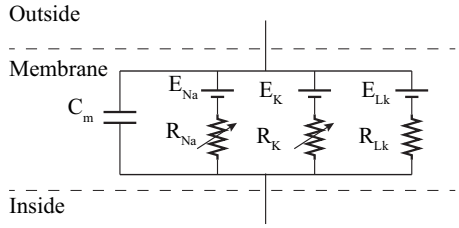


**Figure 2.6:** Hodgkin and Huxley membrane model

ternal electrical stimulation can be analyzed by modeling these nerve fibers as linear cables. This model assumes that at any longitudinal position along the cable, the TMV is the same in the entire circumference described by the membrane. Figure 2.7 shows the equivalent circuit for a myelinated nerve fiber [86].

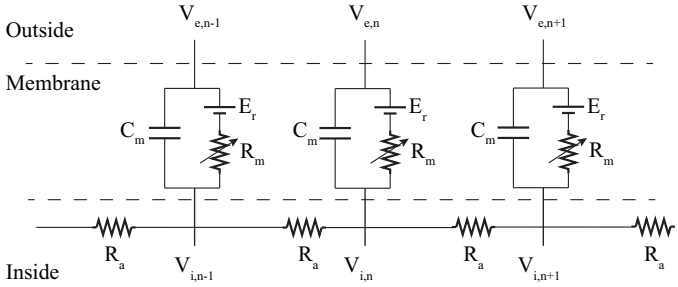


**Figure 2.7:** Equivalent circuit model for the membrane of a myelinated nerve fiber.

From the equivalent circuit an equation describes the time evolution of the TMV with the voltage under the presence of an external electrical stimulus is can be derived:

$$C_m \frac{dV_n}{dt} + I_{i,n} = \frac{1}{R_a} \left( V_{i,n-1} - 2V_{i,n} + V_{i,n+1} \right) \tag{2.2}$$

where $C_m$ is the membrane capacitance of the node, $R_a$ is the resistance between successive nodes (associated with the intracellular media), $V_n$ is the TMV at the nth node of Ranvier, $I_{i,n}$ is the ionic current at the node and $V_{i,n}$ is the internal voltage at the node. $V_n$ is taken relative to the resting TMV and can be expressed as $V_n = V_{i,n} - V_{e,n}$ in order to relate it with the external voltage $V_{e,n}$ generated by an external stimulus. Thus, for a given external voltage distribution it is possible to calculate the time course of the TMV.

The left side in Eq. 2.2 represents the capacitive and ionic currents that flow through the membrane and the right side represents internal

current between successive nodes. Most of the models for external electrical stimulation used nowadays are based on the cable model presented above. The limitations of this model will be addressed in section 5.4.2.

### 2.3.6 The neuromuscular system

As explained in section 2.3.4, muscles are controlled by the central nervous system through the connection established by the motor neurons.

Muscles are made up of a large number of contractile elements, the muscle fibers. The number of muscle fibers depends on the size of the muscle, in humans it ranges between a few thousands to a few millions [89]. When an action potential is initiated in a muscle fiber a complex mechanism takes place producing a contraction [75]. Muscle contractions are the result of several muscle fibers undergoing through this process and the strength of a contraction depends on the number of contracting fibers as well as their individual strengths [90].

When an action potential reaches the axon terminals, a neurotransmitter is released causing the depolarization of the muscle fibers. This points at which the motor neurons connect with the muscle fibers are known as the neuromuscular junctions (NMJ). Each muscle fiber has a single NMJ, meaning that it can only be activated by a single motor neuron. In contrast, when the axon of a motor neuron enters the muscle it branches innervating several muscle fibers. Each motor neuron in a muscle and the group of fibers innervated by it form a motor unit (MU) (Figure 2.8). The MU is the smallest functional structure of the muscle that can be controlled by the central nervous system. The diameter of a motor neuron is related to the MU size (number of fibers that contains) [91] and the number of muscle fibers in a MU varies largely between muscles and within MUs in the same muscle. In humans, this number can range between 3 and a few hundreds [75].

Under a voluntary muscle contraction, MUs are activated following a precise and asynchronous pattern. On the one hand, the force production is distributed temporally between different MUs in order to distribute the work load during a sustained contraction. On the other hand MUs are progressively recruited in ascending order. Namely, smaller MUs are activated first and larger MUs are progressively added depending on the force demanded [92]. This phenomenon, known as the "size principle", combined with the asynchronous re-

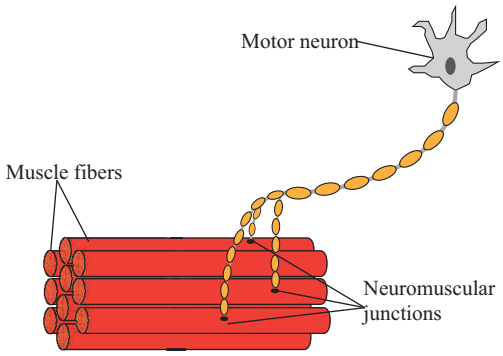


**Figure 2.8:** Motor unit

cruitment confers the central nervous system fine control of the muscle and at the same time minimizes the rate of muscle fatigue.

### 2.3.7 Functional electrical stimulation

Damage to the nervous system after an event such as stroke or spinal injury may impair the communication between the central nervous system and the muscles and, as a consequence, voluntary muscle control may be lost or significantly reduced. However, in most of these cases the neuromuscular systems remain intact and electrical stimulation can be applied in order to artificially trigger muscle contractions. This approach, known as functional electrical stimulation (FES), is used to restore muscle function, support rehabilitative therapeutic, and prevent medical complications associated with muscle paralysis [76].

The main challenges that hinder the widespread use of FES are poor control over the muscle force production and rapid onset of muscle fatigue. These problems derive from differences in the recruitment patterns of muscle fibers between voluntary and electrically evoked muscle contractions. The recruitment order in electrical stimulation is the opposite to that of a voluntary contraction [93] and is completely synchronous. Due to the axonal membrane charging dynamics, thicker axons require lower currents in order to depolarize and initiate an action potential. Therefore, since large MUs are associated to thicker axons they are more easily activated by an electric stimulus. This causes jerky contractions and significantly increases the rate of muscle fatigue.

Most FES systems utilize surface electrodes usually placed targeting the motor point, which is the point where the strongest response to stimulation is obtained. This approach implies the recruitment of all large MUs in every stimulus and leads to rapid muscle fatigue. In order to minimize fatigue production, different strategies have been tested based on the stimulus waveform and the electrode placement [94, 95]. However, although the optimization of the stimulus waveform and the stimulation frequency may improve the results in some applications, it has been demonstrated that the most effective strategy to reduce fatigue and improve muscle control is based on the use of multiple electrodes for selective activation of muscle subunits [96]. This approach, known as interleaved stimulation, is based on spatially and temporally distributing the force production across the muscle maintaining a controlled force production over a longer time.

## 2.4 Electroporation and peripheral nerve stimulation

### 2.4.1 Peripheral nerve stimulation in electroporation based treatments

As explained in the previous sections, both electroporation and electrical stimulation of peripheral nerves can be regarded as threshold-like phenomenona that depend on the cell TMV: they occur when an external electric field induces a TMV higher than a certain threshold.

In electroporation based treatments, treatment planning is performed under the assumption that all the cells exposed to an electric field higher than a certain value will experience the desired effect (either a reversible permeabilization level or cell death) [97]. The electric field threshold is estimated through experimental measurements and depends on the pulsing protocol (i.e. temporal features of the pulses) and the cells or tissues being treated. In clinical applications, electroporation protocols usually consist in a series of monopolar pulses with a length in the order of 100 $\mu$s. For these pulses, the electric field thresholds to trigger action potentials in excitable cells are significantly lower than those for initiating electroporation. This implies that, in order to successfully perform electroporation based treatments, it is necessary to deliver high voltage pulses that can cause electrical stimulation of excitable tissues such as the efferent and af-

ferent nerve fibers within the region of treatment or surrounding areas, even in distant regions leading to muscle contractions and acute pain.

This electrical stimulation that appears as a side effect in electroporation based treatments may cause multiple clinical complications. Minimizing the risks associated to those complications leads to an increase in the complexity of the whole clinical procedure that may limit the applicability of electroporation based treatments because of the burden to benefit ratio or the risk to benefit ratio. First, to overcome acute pain, it is necessary to administer local anesthesia and, in some cases, it is even necessary to administer general anesthesia. Second, muscle contractions may displace the electrodes and change the outcome of the treatment by changing the distribution of the electric fields that are applied with respect to the prior planning. Furthermore, such electrode displacement may mechanically damage vital structures close to the region being treated. Therefore, sometimes it is necessary to administer muscle relaxants. Additionally, since the myocardium is a structure that contains excitable cells, the high currents that flow in the body during an electroporation based treatment may induce heart arrhythmias, including ventricular fibrillation.

Electrical stimulation has been a concern among researchers and clinicians working in the field of electroporation since the first medical applications began to be developed [5]. When electrochemotherapy emerged, the main concern was the risk of ventricular fibrillation. Fortunately, quite early it was identified a mechanism to prevent it: to synchronize the electroporation pulses with the electrocardiogram signal to deliver them when all myocardium cells are in the absolute refractory period [98, 99].

With the aim of reducing muscle contractions and acute pain, it has been proposed to confine the electric field the by placing a large number of electrodes surrounding the treated region [100]. This sort of approach, however, would be very challenging to implement in clinical settings, for instance, when treating deep seated tumors.

Another approach to reduce electrical stimulation that has been relatively explored is based on modifying temporal features of the pulses. Daskalov et al [101] tried alternating the polarity between successive pulses and compared the outcomes with a conventional treatment. The treatment efficiency was maintained and while the authors did not measure the muscle contractions, they reported that "the patients noted a difference in the stimuli-provoked sensation" and "The biphasic pulses were better tolerated". Later, Miklavčič et al. [102] showed

that, by adjusting the pulse delivery frequency, it was possible to reduce the number of contractions and their strength while maintaining the treatment efficacy.

Recently, a novel method, also based in modifying the temporal features of the pulses, has been proposed. The treatment is based on replacing the conventional 100 $\mu$s monopolar pulses by bursts of bipolar pulses with the same energized time and a short pulse length (1-5 $\mu$s) [7]. It has been demonstrated that this technique, coined "high-frequency irreversible electroporation" (H-FIRE), is able to successfully ablate regions of tissue by means of IRE while practically avoiding muscle contractions [103–107].

### 2.4.2 Effects of electroporation on peripheral nerves

There are very few reports on the effects of electroporation in peripheral nerves in the literature. Abramov et al. [108] performed a study on the effects of electrical shocks in peripheral nerves. The study aimed at investigating the effects of the electrical shocks that can be suffered in an industrial electrical accident. Although the focus of the study was not on electroporation, the authors associated their results to this phenomenon. They found that the shocks produced a transient reduction in the action potential amplitude and the conduction velocity, as well as an increase of the refractory period. All these effects were dependent on the applied electric field, and the animals exposed to the lowest fields did not suffer any significant alteration. In addition, the effects were apparently permanent in the animals exposed to the largest field magnitudes while the rest of the animals recovered the initial values after 3 hours.

Comparable results to those by Abramov et al. were obtained in later studies in isolated muscles [109, 110]. A total loss of contractile force was observed immediately after the treatments when electric field magnitudes above a certain value were delivered. This effect was transient except in the muscles exposed to the highest electric field magnitudes. Additionally, the rate and extent of recovery depended on the magnitude of the applied pulses (higher and faster recovery for the lowest electric fields and almost no recovery for the highest electric field)[110].

In one of the aforementioned studies [110], the extracellular concentrations of $Na^+$ and $K^+$ inside the muscle were monitored. After the pulse, a release of $K^+$ to the extracellular medium as well as an uptake of $Na^+$ ions by the cells were noticed. This ionic transport lasted

for about 20 minutes and, after that, the ionic concentrations slowly returned to their initial values. In addition, it was shown that by pharmacological stimulation of the $K^+$ and $Na^+$ pumps, the recovery time could be decreased. These results indicate that the increase in membrane permeability to ions due to electroporation reduces the ionic concentration gradient between the intracellular and extracellular media. Furthermore, the recovery of the cell functions seems to rely (at least partially) on the ability of the ion pumps to recover the concentration gradient.

Besides the loss of the concentration gradients, electroporation also alters the electrical properties of the cell membrane. In particular, electropoartion creates conductive paths across the membrane which significantly reduces its resistance. According to a numerical study, this effect alone could block the conduction of action potentials along a nerve [111].

In addition to the transient inhibition of the action potential generation and conduction it has been suggested that the massive influx of ions due to electroporation, and in particular $Ca^{2+}$ ions, can trigger other events that would alter the neuronal function [112]. $Ca^{2+}$ is involved in multiple processes that regulate neuronal functions such as synaptic transmission, plasticity and cell viability [113, 114]. Thus, it is reasonable to expect effects associated with the $Ca^{2+}$ influx due to electroporation of peripheral nerves. However, in the present these effects have been relatively unexplored.

The studies described above focused on the acute effects of electroporation. The results of those studies suggested that above a certain electric field, the effects of electroporation were permanent. However, the long term effects on the nerves exposed to high electric fields was unknown. This was addressed by later studies on the long term effects of IRE. These experiments consisted in histopathology studies performed periodically for up to ten weeks [115–117]. The reported time evolution was consistent between them and consisted in a degeneration of the nerve fibers and a posterior regeneration resulting in the emergence of a large number of fibers with small diameter substituting the damaged ones. The whole process followed the patterns of a Wallerian degeneration [118] followed by a regeneration of the fibers. Wallerian degeneration is a well known process that takes place after a nerve injury and results in the complete clearance of the endoneurial channel (connective tissue layer that encloses each nerve fiber inside peripheral nerves) [119]. After this process a new axon can grow oc-

cupying the path of the injured one, however, it may never reach its previous diameter. Regarding the functionality of the nerves after the regeneration, the action potential amplitude showed a significant difference between the treated and the control nerves after two months in one of the studies [117], while another study reports a full recovery after ten weeks [115].

The studies described in this section are particularly relevant for the clinical applications of electroporation and in particular for tissue ablations by means of IRE. As explained in section 2.2.4 IRE kills the cells within a tissue while leaving the extracellular matrix intact. This characteristic of IRE ablation is crucial for the nerve regeneration since the whole regeneration process relies on the preservation of the architecture of the endoneurium. In addition, the studies introduced in the last paragraph suggest that IRE treatments if applied close to a nerve may allow the posterior regeneration of the nerve fibers that were damaged.

Chapter 3

# Dependence of electroporation detection threshold on cell radius

**Abstract** —It is widely accepted that electroporation occurs when the cell TMV induced by an externally applied electric field reaches a certain threshold. Under this assumption, in order to trigger electroporation in a spherical cell, Schwan's equation leads to an inversely proportional relationship between the cell radius and the minimum magnitude of the applied electric field. And, indeed, several publications report experimental evidences to support that. However, this dependence is not always observed or is not as steep as predicted by Schwan's equation. The numerical study presented in this chapter attempts to explain these observations that do not fit Schwan's equation on the basis of the interplay between cell membrane conductivity, permeability and TMV. For that, a single cell in suspension was modeled and it was determined the electric field necessary to achieve electroporation with a single pulse according to two effectiveness criteria: a specific permeabilization level, understood as the relative area occupied by the pores during the pulse, and a final intracellular concentration of a molecule due to uptake by diffusion after the pulse, during membrane resealing. The results indicate that plausible model parameters can lead to divergent dependencies of the electric field threshold on the cell radius. These divergent dependencies were obtained through both criteria and using two different permeabilization models. This suggests that the interplay between cell membrane conductivity, permeability and transmembrane voltage might be the cause of results which are non compatible with the Schwan's equation model.

Part of the contents of this chapter is adapted from:

B. Mercadal, P. T. Vernier and A. Ivorra "Dependence of Electroporation Detection Threshold on Cell Radius: An Explanation to Observations Non Compatible with Schwan's Equation Model" *J. Membr. Biol*, vol. 249, no. 5, pp. 663–676, 2016.

URL: https://link.springer.com/article/10.1007/s00232-016-9907-0

DOI: 10.1007/s00232-016-9907-0

## 3.1 Introduction

Although electroporation is not a bi-stable phenomenon, and cell membrane permeabilization exhibits a monotonically increasing dependence on the local TMV, this dependence is exponential [24] and in practice so abrupt that it is widely accepted that electroporation occurs when the TMV reaches a certain threshold. This simplification is supported by experimental observations in which electroporation was noticed to behave as a threshold-like phenomenon [23–28].

In section 2.1 an analytical expression to calculate the TMV induced in a spherical cell was introduced, the Schwann equation (Eq. 2.1). Assuming a threshold TMV, this equation yields a proportionally inverse relationship (for a spherical cell) between the cell radius and the minimum magnitude of the applied electric field $E_c$ for initiating electroporation.

$$E_c = \frac{2 \cdot TMV}{3 \cdot R \cdot \cos\theta} \tag{3.1}$$

There are, indeed, several published studies which report experimental evidences for an inverse relationship between the cell size and the electric field required to achieve electroporation [19, 120–123]. However, this dependence is not always observed or is not as steep as predicted by Schwan's equation [124–128]. We hypothesize that these other results contradict the Schwan's equation model because that model is only valid for describing what happens just before electroporation of the poles of the cells facing the electrodes ($\theta = 0°$, $\theta = 180°$) and is not adequate for describing the conditions necessary to achieve detectable electroporation.

First, it must be noted that once the TMV reaches the critical value or threshold and electroporation takes place, membrane electroporation occurs in a few nanoseconds [31, 32, 129, 130] and membrane conductivity increases to a value that keeps the local TMV of the electroporated regions of the cell close to its threshold value. The increase in membrane conductivity tends to reduce the TMV but if that happens then the conductivity decreases immediately and hence voltage goes up again. This sort of negative feedback short-circuiting effect reduces the $\cos\theta$ dependence of local TMV in Schwan's equation. The profile of the TMV along the membrane flattens at the poles facing the electrodes. This was observed experimentally [25]. Therefore, while Schwan's equation predicts a directly proportional relationship between the applied field and the TMV over the whole cell, in reality a non-linear relationship should be expected in which

TMV increases at a lower rate once a field threshold is reached. In other words, the Schwan's equation model overstates the TMV of an electroporated cell.

Secondly, it must be noted that assessment of electroporation is based on measurable effects such as dye uptake [122, 125, 131], changes in membrane conductivity [40, 132, 133], or cell lysis [19, 127, 134] which are related to changes over a significant area of the membrane after electroporation whereas the Schwan's equation model can only predict when electroporation starts at an infinitesimal portion of the cell membrane area ($\theta = 0°$, $\theta = 180°$).

From these considerations we first hypothesized that, by modeling membrane conductivity changes during the electroporation pulse, we might predict that in order to achieve a certain level of permeabilization the necessary field (critical field) might not obey Schwan's equation model and might explain the apparently contradictory experimental results regarding the dependence of electric field threshold on cell radius. We then extended the study using a simple diffusion model to quantify the uptake of a probe solute after the electroporation pulse to test the dependence of the critical field to achieve a certain intracellular concentration on the cell radius.

## 3.2 Materials and methods

In this study we defined two criteria to estimate the minimum electric field required to be able to detect electroporation experimentally. The first criterion – related to changes that take place during the pulse – is that we need to reach a minimum level of permeabilization during the pulse, characterized by the average relative pore area (RPA) over the whole membrane. That is, we considered that electroporation can be detected if the relative area of the membrane occupied by pores reaches a threshold value (e.g. 0.01%). The second criterion – related to the processes that take place after the electroporation pulse – is that we need to reach a certain intracellular concentration of a specific ion or molecule after the application of the pulse.

### 3.2.1 Membrane permeabilization during the pulse

To model membrane permeabilization and conductivity changes during the pulse, we used and compared two different models. First, a membrane conductivity model [135] intended to reproduce the conductivity changes that would occur during the first microseconds after

the pulse onset. Second, an electroporation model based on pore creation [136], to assess permeabilization and conductivity at the end of a typical electroporation pulse.

We numerically modeled electroporation of a single cell in a suspension using the FEM based software platform COMSOL Multiphysics 4.4 (Stockholm, Sweeden). The simulations were performed for both models, and according to the first criterion we defined we imposed values of the RPA. Then, for various values of cell radius, different magnitudes of the applied electric field were tested in the models in order to find the magnitude of the field that leads to the desired value of the RPA.

**Model 1: Membrane conductivity model**

A membrane conductivity model from Ivorra et al. [135] – based on experimental measurements from Kinosita and Tsong [137] – was used to describe membrane conductivity dependency on TMV in the first microseconds after the pulse onset due to the electroporation phenomenon:

$$\sigma_m = \sigma_{m0} + K(e^{\beta|TMV|} - 1) \tag{3.2}$$

where $\sigma_{m0}$ is the conductivity of the membrane at the resting $TMV$ and $K$ and $\beta$ are two constants adjusted to fit experimental measurements. If we assume that the membrane conductivity increase is due to the creation of pores, Eq. 3.2 can be written as:

$$\sigma_m = \sigma_{m0} + \sigma_p[\lambda(e^{\beta|TMV|} - 1)] \tag{3.3}$$

where $\lambda$ would be another constant, and $\sigma_p$ is the equivalent conductivity of the medium filling the pores. The term $\lambda(e^{\beta|TMV|} - 1)$ would represent the local relative pore area, and therefore the constant $K$ on Eq. 3.2 depends on $\sigma_p$.

The steady state problem for the geometry depicted in Figure 3.1. was solved in the *Electric currents* mode of the *AC/DC* module of COMSOL (*Stationary Study*) using the linear system solver *Pardiso*. The conductivities of the intracellular and the extracellular media are constant while membrane conductivity depends on TMV as described in Eq. 3.2. Due to the symmetry of the geometry and to minimize computational time a 2-D axisymmetric model was constructed in COMSOL. Dimensions of simulation space were taken large enough so that electric field in the vicinity of the cell could not be distorted due to boundary conditions. Model parameters are shown in Table 3.1.

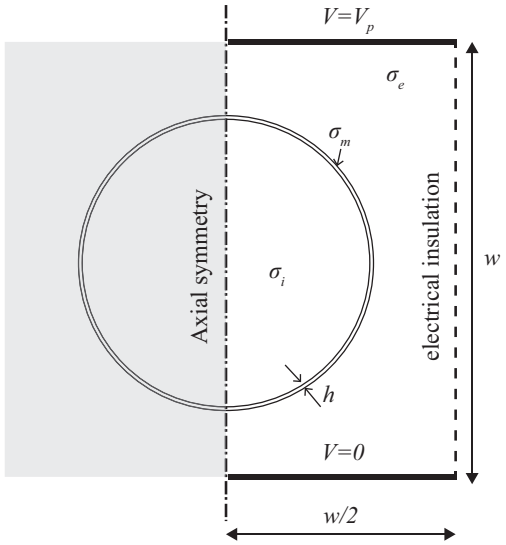


**Figure 3.1:** Representation of the cell in suspension model implemented for simulation by FEM in COMSOL. Conductivities of the intracellular and extracellular media are constant while membrane conductivity is a function of the local TMV.

**Table 3.1:** Model parameters used in the FEM model with the membrane conductivity model of Ivorra et al. [135].

| Symbol | Value | Definition, justification or source |
|---|---|---|
| $\sigma_{m0}$ | $2.5 \cdot 10^{-7}$ S/m | Membrane conductivity when $TMV = 0$ if membrane thickness is 5 nm [138] |
| $\beta$ | 16 | Constant of the conductivity model [135] |
| $K$ | $5 \cdot 10^{-9} \cdot \sigma_p$ | Constant of the conductivity model [135] |
| $\sigma_e$ | 1.5 S/m | Extracellular conductivity, isotonic NaCl [137] |
| $\sigma_i$ | 0.5 S/m | Intracellular conductivity [35] |
| $\sigma_p$ | $\frac{\sigma_e - \sigma_i}{\ln(\sigma_e/\sigma_i)}$ | Conductivty inside the pore [139] |
| $h$ | 5 nm | Membrane thickness [24] |
| $w$ | $10 \cdot R$ | Dimensions of the simulated space (10 times cell radius) |

To model the effect on membrane conductivity of an electroporation pulse in the first microseconds after the onset, the solution of the steady state problem depicted in Figure 3.1 represents a proper approximation even though the dynamics of the electroporation phenomena as well as membrane charging process are neglected. At this stage, a few microseconds after the pulse onset, the membrane is completely charged and the very fast increase in membrane conductivity – presumably due to pores – has concluded to be followed by a slow and mild increase during the rest of the pulse [25, 35]. the parameters

of the model were adjusted to match conductance measurements at 2 $\mu$s after the beginning of the pulse from [137], hence it can be assumed that the obtained results will reproduce qualitatively the effect of a pulse within this timescale.

The simulated space is about 104 times larger than the membrane thickness, which makes the numerical solution complicated and time consuming. To address this, Ivorra et al. [135] used a membrane thickness 10 times larger than a realistic value (50 nm instead of 5 nm) and rescaled the electrical properties of the membrane to not alter the results. Here, to avoid this complication, each subdomain (extracellular and intracellular) was calculated through a separate application mode of the same type as in [140, 141], and the membrane was replaced by a surface to which a boundary condition that accounts for membrane conduction and displacement currents [12, 142] was added:

$$\vec{n} \cdot \vec{j} = \frac{\sigma_m (V - V_{ref})}{h} + \frac{\epsilon_m}{h} \frac{\partial (V - V_{ref})}{\partial t} \tag{3.4}$$

where $V$ and $V_{ref}$ are the potentials on the interior and the exterior side of the boundary respectively, $\epsilon_m$ is the permittivity of the membrane, and $h$ is membrane thickness. The product $\vec{n} \cdot \vec{j}$ represents the normal current that flows across the membrane. Note that displacement currents are not taken into account in steady state solutions, thus the second term in Eq. 3.4 was not included in the computation of steady state solutions.

According to the model presented in Eqs. 3.2 and 3.3, the average membrane conductivity would be related to the area occupied by the pores. Since $\sigma_{m0}$ and $\sigma_p$ are constant along the membrane, and the term $\lambda(e^{\beta|TMV|} - 1)$ represents the local area occupied by pores at each point of the membrane, the average membrane conductivity is related to the RPA as follows:

$$\overline{\sigma_m} = \sigma_{m0} + \sigma_p \cdot RPA \tag{3.5}$$

The average conductivity of the membrane, $\overline{\sigma_m}$, was obtained from the COMSOL results post-processor. Then from Eq. 3.5 the RPA can be calculated. To do so, the effective conductivity of the pores was estimated using the realtion proposed by Li and Lin [139]:

$$\sigma_p = \frac{\sigma_e - \sigma_i}{\ln(\sigma_e / \sigma_i)} \tag{3.6}$$

Where $\sigma_e$ and $\sigma_i$ are the conductivity of the extracellular and the intracellular medium respectively.

**Model 2: Pore creation based model**

We also performed numerical simulations of the geometry depicted in Figure 3.1 using the asymptotic electroporation model from DeBruin and Krassowska [136]. This model states that the pore formation dynamics is governed by the differential equation:

$$\frac{dN}{dt} = \alpha e^{\left(\frac{TMV}{V_{ep}}\right)^2} \left(1 - \frac{N}{N_0} e^{-q\left(\frac{TMV}{V_{ep}}\right)^2}\right) \tag{3.7}$$

where $N$ is the pore density in the membrane, $N_0$ the equilibrium pore density in the membrane when $TMV = 0$ and parameters $\alpha$, $q$ and $V_{ep}$ are constants of the model. The creation of pores in the membrane due to the electroporation phenomena causes an increase in membrane conductivity, $\sigma_{ep}$, that is calculated as in [139, 143]:

$$\sigma_{ep} = N \cdot \frac{2\pi r_p^2 \sigma_p h}{\pi r_p + 2h} \tag{3.8}$$

where $r_p$ and $h$ are the radius of the pores and the membrane thickness respectively, and $\sigma_p$ is the effective conductivity of the solution inside the pores, which was approximated as in the previous section (Eq. 3.6).

To perform numerical simulations, Eq. 3.7 was included into the model using the *Weak Form Boundary* PDE mode of COMSOL and the problem depicted in Figure 3.1 was solved in the Electric currents mode of the AC/DC module of COMSOL (*Time-dependent Study*) using the linear system solver *Pardiso*. As in the previous section, membrane was replaced by a surface with a boundary condition (Eq. 3.4) and the membrane conductivity at each time step was calculated as the sum of the unaltered membrane conductivity $\sigma_{m0}$ and the conductivity due to electroporation phenomenon $\sigma_{ep}$ from Eq. 3.8 ($\sigma_m = \sigma_{m0} + \sigma_{ep}$. Parameters used in the model are shown in Table 3.2.

To estimate the RPA, first the total number of pores was calculated by integrating the pore density $N$ over the whole membrane surface:

$$N_{tot} = \int N \cdot dS \tag{3.9}$$

Then it was straightforward to obtain the RPA as the quotient between the total surface occupied by pores and the cell surface:

$$RPA = \frac{N_{tot} \pi r_p^2}{4\pi R^2} \tag{3.10}$$

where $R$ is the cell radius.

**Table 3.2:** Model parameters used in the FEM simulations with the electroporation model of DeBruin and Krassowska [136] to calculate the electric potentials, membrane conductivity and pore density during an electroporation pulse.

| Symbol | Value | Definition, justification or source |
|---|---|---|
| $\sigma_{m0}$ | $2.5 \cdot 10^{-7}$ S/m | Membrane conductivity when $TMV = 0$ if membrane thickness is 5 nm [138] |
| $\sigma_e$ | 1.5 S/m | Extracellular conductivity, isotonic NaCl [137] |
| $\sigma_i$ | 0.5 S/m | Intracellular conductivity [35] |
| $h$ | 5 nm | Membrane thickness [24] |
| $w$ | $10 \cdot R$ | Dimensions of the simulated space (10 times cell radius) |
| $\epsilon_e$ | 70 | Relative permittivity of the extracellular medium [144] |
| $\epsilon_i$ | 70 | Relative permittivity of the intracellular medium [144] |
| $\epsilon_m$ | 5 | Relative permittivity of the membrane [144] |
| $\sigma_p$ | $\frac{\sigma_e - \sigma_i}{\ln(\sigma_e/\sigma_i)}$ | Conductivty inside the pore [139] |
| $r_p$ | 0.76 nm | Pore radius [136] |
| $q$ | 2.46 | Electroporation constant [136] |
| $\alpha$ | $10^9$ | Electroporation parameter [136] |
| $V_{ep}$ | 0.258 | Characteristic voltage of electroporation [136] |
| $N_0$ | $1.5 \cdot 10^9\ m^{-2}$ | Equilibrium pore densitiy when $TMV = 0$ [136] |

### 3.2.2 Transmembrane transport after the pulse

The second criterion used to assess electroporation effectiveness consisted in reaching a certain intracellular concentration of an arbitrary extracellular solute at a long time after the application of the pulse. Since most of the transport takes place after the pulse [45, 51–54]; the contribution of both electrophoretic and diffusion transport during the pulse can be neglected. Thus, it was only considered the transport by diffusion after the pulse, which can be quantified by Fick's law:

$$\frac{dc(t)}{dt} \cdot \frac{V}{S_p(t)} = -D\frac{dc(t)}{dx} \tag{3.11}$$

where $c(t)$ is the molar concentration of the considered ion or molecule passing through the surface $S_p$, which is the effective surface where transport can take place, $V$ is the volume of the cell and $D$ the diffusion constant. The effective surface of diffusion, $S_p(t)$, in Eq. 3.11 was defined as the area of the membrane occupied by pores or defects through which ions or molecules can penetrate into the cell. This surface was modeled as time dependent to account for membrane resealing.

According to our current knowledge on the electroporation dynamics (see section 2.2.2), the membrane resealing process occurs in at least two different phases. These phases are associated with the different

populations of pores or defects that appear in the membrane during the electroporation pulses. Namely, a population of short-lived pores which play a major role in the membrane conductivity increase and a population of more stable long-lived pores trough which most of the post-pulse transmembrane transport takes place. Since most of the transport takes place after the pulse, and the hypothetical short-lived pores seem to shrink within a few milliseconds [24, 35, 37, 38, 45, 145], the transport through these pores was neglected in the model employed here. Therefore to approximate the effective diffusion surface, $S_p$, the focus was on the fraction of the hypothetical long-lived pores and its dynamics. To model this behavior, here it was employed an exponential time decay function:

$$S_p(t) = S_{per} e^{-t/\tau} \tag{3.12}$$

being $S_{per}$ the surface occupied by the long-lived pores, or defects, at the end of the pulse.

Experimental studies on cell membrane permeabilization – based on the influx or efflux of ions and/or molecules – report a wide range of timescales for the slow resealing process: hundreds of milliseconds [26, 146, 147], several seconds [24, 45, 47, 148] and a few minutes [21, 49, 149].

The RPAs due to the hypothetical short and long-lived pores have been quantified simultaneously after different number of pulses [37, 38]. The percentage of RPA arising from long-lived pores respect to the total RPA ranged from about 5% after a single pulse to about 15% after 8 pulses. Here the value of $S_{per}$ was approximated as a fraction of the surface occupied by pores at the end of the pulse, $S_p$, taking into account these percentages. That is, the value of the surface occupied by the long-lived pores was computed as the product of the RPA (as obtained in previous sections), the total surface of the cell membrane ($S_c$) and the fraction of long-lived pores with respect to the total population of pores ($f$):

$$S_{per} = f \cdot S_p = f \cdot RPA \cdot S_c \tag{3.13}$$

To find a compact expression for intracellular concentration $c_i(t)$ for long times after the pulse, we need to solve Eq. 3.11 defining the transport through the membrane surface as the difference between intracellular and extracellular concentration: $c(t) = c_i(t) - c_e(t)$. The following simplifications were made for such purpose:

- For cell suspensions with a low cell volume fraction or for a low final intracellular concentration (compared with the extracellular concentration), the external concentration can be considered constant: $c_e(t) = c_e(0) = c_e$. For instance, for a cell volume fraction of 0.2 and a final intracellular concentration of a 5% the extracellular concentration, the variation in extracellular concentration is less than 2% (see 3.6).
- Since ions or molecules considered here cannot enter into the cell in normal conditions and the transport during the pulse can be neglected, the initial intracellular concentration can be approximated to zero: $c_i(0) \approx 0$.
- The term $\frac{dc(t)}{dx}$ is the concentration gradient across the membrane and can be approximated as $(c_i(t) - c_e)/h$, being $h$ cell membrane thickness.

After these simplifications, Eq. 3.11 yields to:

$$c_i(t) = c_e \left(1 - exp\left[\frac{DS_{per}\tau}{Vh}\left(e^{t/\tau} - 1\right)\right]\right) \tag{3.14}$$

If it is assumed that the final intracellular concentration is measured a long time after the pulse application, then it is possible to approximate time in Eq. 3.14 as infinity (practically no transmembrane transport takes place for times longer than a few times the value of $\tau$ after the pulse). This leads to a simple expression for the final intracellular concentration after pore resealing:

$$c_i = c_e \left(1 - e^{\frac{-DS_{per}\tau}{Vh}}\right) \tag{3.15}$$

Taking into account how $S_{per}$ was defined, here it was employed the following expression to estimate the RPA during the pulse necessary to reach a certain intracellular concentration from Eq. 3.15:

$$RPA = \ln\left(1 - \frac{c_i}{c_e}\right)\frac{Rh}{3fD\tau} \tag{3.16}$$

where $R$ is cell radius.

Imposing values for intracellular and extracellular concentrations (or their ratio), as well as for the diffusion constant and the resealing time constant, this expression (Eq. 3.16) provides the necessary RPA as function of cell radius. From these values and using the permeabilization models explained in the previous sections it was possible to calculate the necessary applied field as a function of radius in each case by testing different magnitudes of the electric field.

## 3.3 Results

### 3.3.1 Relative pore area during the pulse

The first criterion we defined to assess the necessary applied electric field in order to detect electroporation was to impose a value for the RPA. The values of RPA reported in electroporation experiments range between $10^{-3}$ and $10^{-5}$ [25, 35, 45, 150]. We simulated the applied electric field required to obtain different values of the RPA at the cell membrane as a function of cell radius. The results obtained with the membrane conductivity model [135] are depicted in Figure 3.2. For a small RPA ($10^{-5}$) the relationship between electric field and cell radius is almost indistinguishable from the $1/r$ behavior predicted by Schwan's equation (Eq. 3.1). However, as we increase the imposed RPA, the electric field dependency on cell radius becomes less steep. Moreover for RPA of $10^{-4}$ and above the simulated results differ significantly from an inverse function of cell radius.

Results obtained with the electroporation model based on pore creation [136] for a single pulse of 100 $\mu$s are shown in Figure 3.3. Results are very similar to those obtained using the membrane conductivity model: for a small RPA the results fit with the prediction of a $1/r$ relationship between electric field and cell radius; as we impose higher RPA values this dependency becomes less steep, and for RPA values of $10^{-4}$ and higher we observe a substantial deviation of simulation results from an inverse dependency on cell radius.

### 3.3.2 Final intracellular concentration

The other criterion we defined for assessing effective electroporation was based on imposing the minimum final intracellular concentration after the pulse for a given molecule.

Besides defining a value for the final intracellular concentration, plausible values for the diffusion constant (see Eq. 3.15) and the fraction of long-lived pores respect to the total (see Eq. 3.13) need to be chosen. The diffusion constants for dyes and molecules typically used in electroporation experiments reported in the literature are in the range from $10^{-9}$ to $10^{-10}$ $m^2 \cdot s^{-1}$ [45, 151–153]. Regarding the value of the fraction of long lived-pores, we used the value measured experimentally after a single pulse of 100 $\mu$s [37] that was a 5%. Then to obtain the results displayed in Figure 3.4 and Figure 3.5 we imposed a final intracellular concentration value of 5% of the initial extracellular concentration, a value of $2 \cdot 10^{-10}$ $m^2 \cdot s^{-1}$ for the diffusion constant

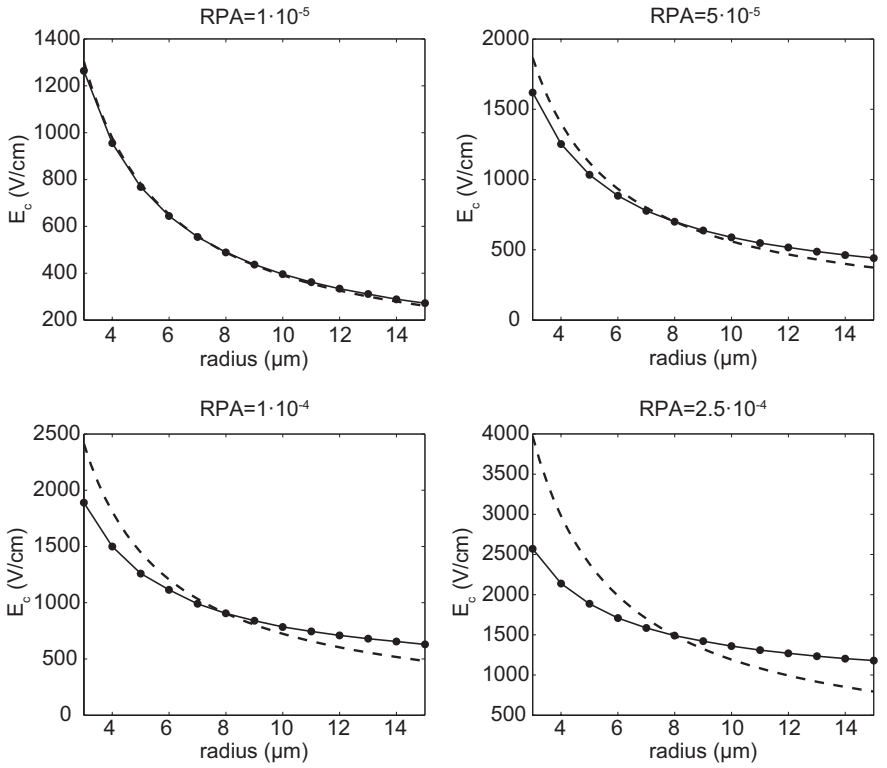


**Figure 3.2:** Simulation results according to permeabilization model 1 of the electric field magnitude required to achieve different values of the RPA (relative membrane area occupied by pores) at the end of a 2 $\mu$s electroporation pulse (•), compared to a function inversely proportional to the radius and adjusted to the value of the field at 8 $\mu$m (dashed line). Simulated results are based on the model geometry depicted in Figure 3.1 and the membrane conductivity model presented in the Materials and Methods section. The RPA was evaluated according to Eq. 3.5.

$D$ – which is the value measured experimentally for the propidium iodide [154] – and different values of the resealing time constant $\tau$.

The results obtained by combining the diffusion model and the membrane conductivity model are displayed in Figure 3.4. When $\tau$ is decreased, the dependency of the electric field on cell radius becomes less steep and simulation results deviate from the expected inverse relationship between radius and electric field. For a $\tau = 2$ seconds a plateau is observed above $R = 8$ $\mu$m where there is no dependence of electric field on cell radius and for $\tau = 1$ second the dependence is very weak for all simulated values of cell radius.

Figure 3.5 shows the results obtained by combining the diffusion model and the electroporation model based on pore creation. Results are

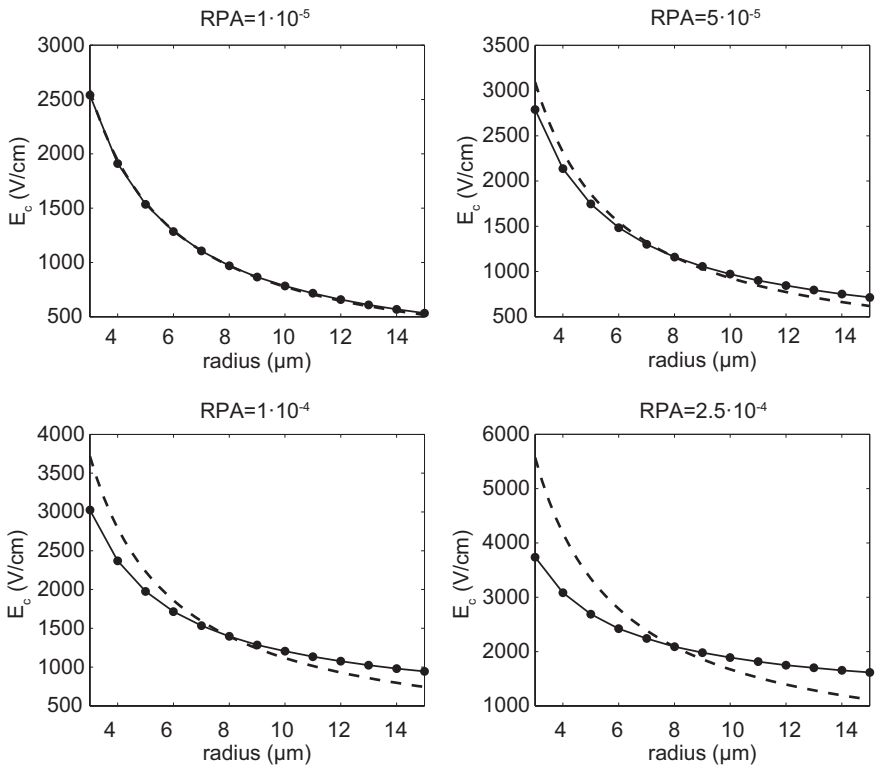


**Figure 3.3:** Simulation results according to permeabilization model 2 of the electric field magnitude required to achieve different values of the RPA (relative membrane area occupied by pores) at the end of a 100 $\mu$s electroporation pulse (•), compared to a function inversely proportional to the radius and adjusted to the value of the field at 8 $\mu$m (dashed line). Simulated results are based on the model geometry depicted in Figure 3.1 and the electroporation model based on pore creation presented in the Materials and Methods section. The RPA was evaluated according to Eqs. 3.9 and 3.10.

very similar to those obtained with the membrane conductivity model although we needed to define lower values of $\tau$ to observe a significant deviation from the expected inverse relationship between radius and electric field. In this case results with $\tau = 1$ second show a plateau for radius above $R = 8$ $\mu$m and results obtained for $\tau = 0.5$ seconds exhibit a very weak dependence on cell radius.

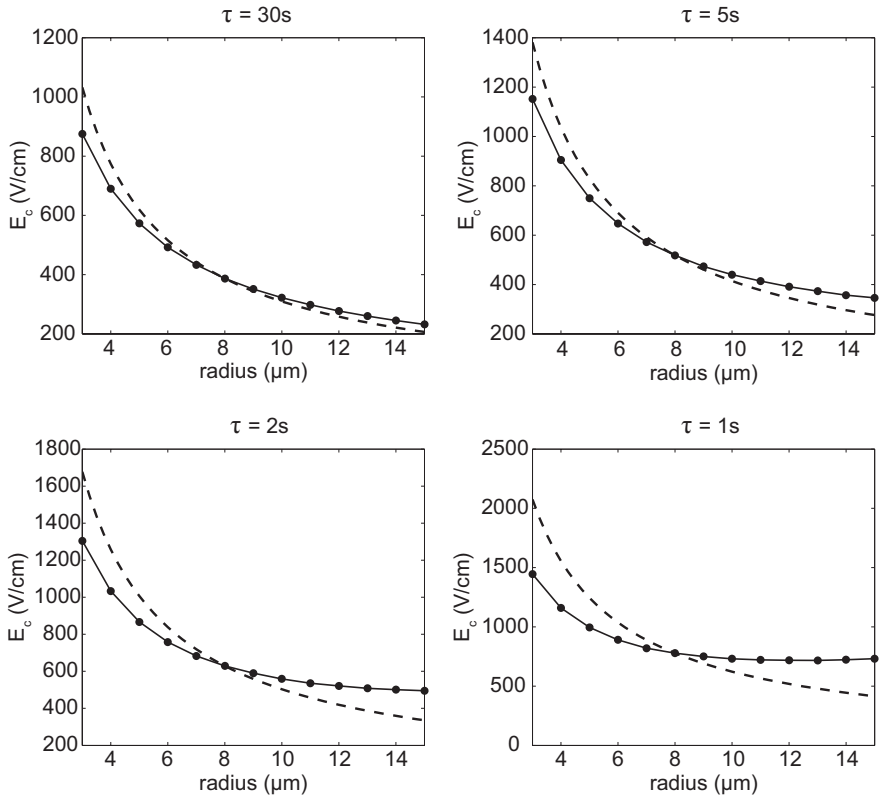


**Figure 3.4:** Simulation results of the electric field magnitude required to achieve a final intracellular concentration value of a 5% the extracellular concentration for different values of the resealing time constant $\tau$ (•),compared to a function inversely proportional to the radius and adjusted to the value of the field at 8 $\mu$m (dashed line). These results were obtained combining the diffusion model presented in the previous section and the permeabilization model 1.

## 3.4 Discussion

### 3.4.1 Relative pore area during the pulse

We calculated the electric field necessary to achieve a RPA as a function of cell radius with two different permeabilization models: a membrane conductivity model based on experimental measurements, and an electroporation model based on the creation of pores. Both models provided similar results indicating that as the imposed RPA is increased the dependency of the electric field on cell radius becomes less steep.

The results obtained with this first criterion can be intuitively explained: since an increase of the RPA means a membrane conduc-

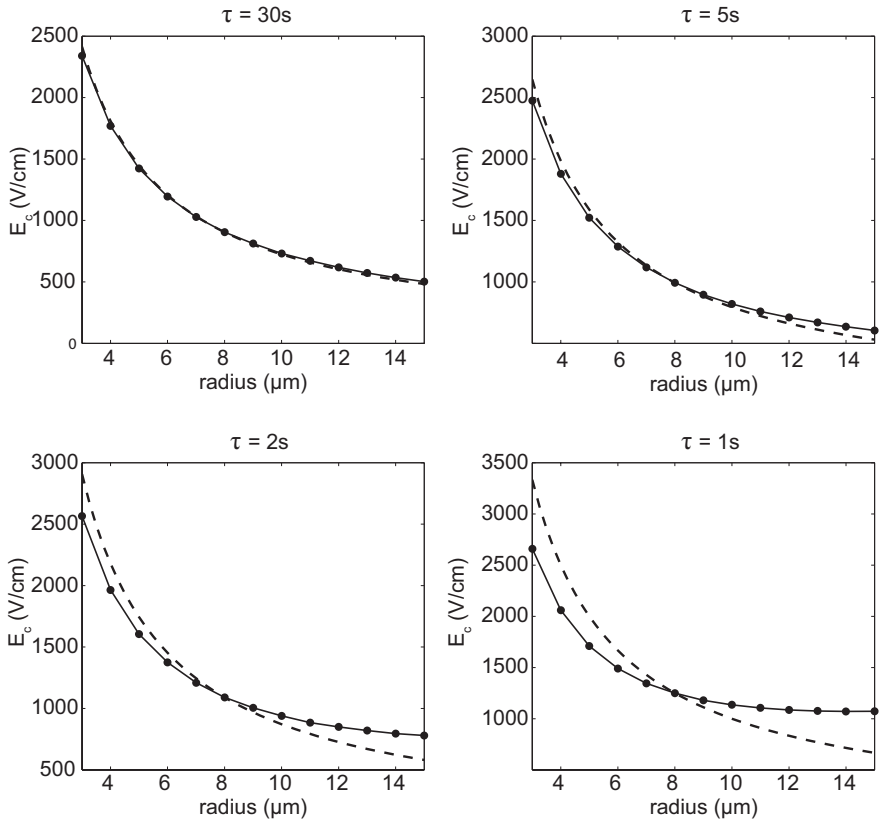


**Figure 3.5:** Simulation results of the electric field magnitude required to achieve a final intracellular concentration value of a 5% the extracellular concentration for different values of the resealing time constant $\tau$ (•),compared to a function inversely proportional to the radius and adjusted to the value of the field at 8 $\mu$m (dashed line). Results were obtained combining the diffusion model presented in the previous section and the permeabilization model 2.

tivity increase, as we get to higher values of the RPA we move away from the condition of a nearly insulating membrane that is assumed in the derivation of Schwan's equation. In particular, due to the short-circuiting effect (explained in section 3.1), the local TMV in those regions of the cell that are already electroporated cannot increase substantially by increasing the external field. This means that above a certain value of the electric field the regions of the membrane that are easier to permeabilize (poles facing the electrodes) will not experience a substantial raise of its local conductivity. Thus in these cases the average conductivity increase for larger fields will be due to an increase in the local conductivity of the regions far from the poles facing the electrodes. This is related to the flattening observed in the TMV

profiles for electric fields above a certain value, and it means that an increase in the RPA can only be accomplished by permeabilizing a larger area of the cell membrane and not so much by further permeabilizing the areas that are already permeabilized. Therefore the deviation between the expected dependence of electric field on cell radius and simulation results gets more pronounced as we increase the value of the RPA.

### 3.4.2 Final intracellular concentration

We calculated the electric field required to reach a certain intracellular concentration as a function of cell radius. The results indicate that depending on the resealing dynamics the dependency of the critical electric field on cell radius can either deviate from the expected $1/r$ relationship according to Schwan's equation model or show a dependency very close to that expected. Results similar to those displayed in Figure 3.4 and Figure 3.5 can be obtained by imposing different values of the final intracellular concentration and adjusting the values of $\tau$ or $D$. Decreasing $\tau$ means that there is less time for the transmembrane transport to take place, and decreasing $D$ means that it is more difficult for the ions or molecules to penetrate into the cell, respectively. Thus lowering one of these two values implies that the initial diffusion surface must be larger in order to reach the same concentration values. Since the diffusion surface is proportional to the RPA, to increase this surface, membrane conductivity during the pulse has to reach values that are far from the assumption of a nearly insulating membrane in Schwan's equation. On the other hand increasing either $\tau$ or $D$ makes transport easier. This means that lower RPA values are required to reach the same concentration, and, as we saw previously for low RPA values, the dependence of the field magnitude on cell radius is similar to the $1/r$ behavior.

From Eq. 3.16 we can see that for a given $D$ and $\tau$, larger cells require larger values of the RPA to reach a given intracellular concentration. This, in comparison to the assessment based on setting a specific RPA during the pulse, leads to a larger deviation between the Schwan's equation model and the simulated dependence of the critical electric field on cell radius.

In the following paragraphs we will discuss some methodological aspects that require further clarification as well as the limitations of this study.

In the derivation of Eq. 3.15 it was assumed that transport during the pulse could be neglected. To validate this assumption, transport during the pulse was quantified as in [47]. The results (not reported here) indicate that the contribution of the transport during the pulse on intracellular concentration is at least five orders of magnitude lower than final concentration even for pulses in the millisecond range. Hence, we conclude that for this analysis transport during the pulse can be ignored, and that this simplification has no impact on the conclusions of the present study.

Regarding the criterion of imposing a final intracellular concentration, it must be noted that, cell electroporation assessment and the detection limit depends substantially on the molecules used and on the detection method [47, 155, 156]. For instance a cytotoxic agent such as bleomycin as few as 500 molecules are needed to kill the cell by a mitotic cell death process [157–159]. On the other hand, when using fluorescence imaging to detect the uptake of a given dye such as propidium iodide, a significant concentration of this dye is needed, at least locally, to be able to distinguish the fluorescence signal from noise. In a real experiment the detection does not depend on the average concentration but in the local concentration, in fact generally fluorescence images present an accumulation in the regions close to the membrane in the areas facing the electrodes. Nevertheless we used a simplified criterion (the average concentration) and an arbitrary value, since the aim was to study how the transmembrane transport can vary depending on the electric field, the cell radius, the diffusion constant and the pore lifetime.

To estimate the effective diffusion surface we used an experimental value that relates the total surface of the whole population of membrane defects (presumably pores) with the surface occupied by long-lived membrane defects. As explained in section 2.2.2, the relation between the long-lived population and the total population of pores is yet not clear, however, experiments suggest that the fraction of long lived pores depends on the electric field magnitude, pulse length, the number of pulses and the pulse repetition rate.

In this study only a single pulse was considered for computing both membrane permeabilization and transmembrane transport. This neglects the fact that, commonly, an electroporation treatment consists in a train of several pulses since it has been observed that multiple pulses are more effective than a single pulse. Nevertheless, it must be noted that the experimental discrepancies regarding the elec-

tric field threshold to detect electroporation and its dependency on cell radius were found also for measurements with single pulse protocols [120, 125, 126, 128]. Therefore, we considered adequate to model a single pulse treatment for the sake of simplicity. Furthermore, it must be noted that mechanisms acting in the electroporation phenomenon that cause the influence of the number of pulses and its repetition rate are yet not elucidated and that the quantification of these effects cannot be accurately modeled. A recent model [160] describes separately the conductivity increase during the pulse and the long term permeabilization of the cell membranes. That model proved to be able to reproduce qualitatively the experimental observations on the uptake of propidium iodide and the dependency of this uptake on the pulse repetition rate. Nevertheless the parameters of the model need to be calibrated to describe quantitatively the phenomenon and the sensitivity of the model to these parameters would have to be investigated before considering its use in our study.

## 3.5 Conclusions

The motivation of the present study was to explore a plausible explanation to the apparently contradictory results that can be found in the electroporation literature regarding the electric field threshold dependency on the cell radius. In particular, it has been attempted to find an explanation to those experimental results that do not follow the Schwan's equation model in which the threshold is predicted to be inversely proportional to the cell radius. While the Schwan's equation model describes when electroporation can be initiated, its relation to detectable outcomes of electroporation (e.g. dye uptake) is more indirect. We therefore hypothesized that by modeling the effects of electroporation, we would be able to predict results not compatible with the Schwan's equation model under some circumstances. And, indeed we have shown that by modeling the interplay between cell membrane conductivity, permeability and transmembrane voltage we obtain electric field thresholds for detection of electroporation that depart from the Schwan's equation model. Departure from the Schwan's equation model is particularly significant when it is imposed that cell membrane permeabilization has to reach a high value during the pulse (RPA $> 10^{-4}$) whereas it is almost unnoticeable when the imposed permeabilization is low (RPA $< 10^{-5}$). When uptake of an extracellular molecule is modeled, departure from the Schwan's equation model is even further exaggerated. These results have been obtained using

two different electroporation models.

## 3.6 Appendix

### Variation in extracellular concentration

Assuming that the initial intracellular concentration is zero and there is no change in cell volume during the experiments, initial and final concentrations can be written as:

$$\begin{cases} c_{i,0} = 0 \\ c_{e,0} = \frac{N_0}{V(1-F)} \\ c_{i,f} = \frac{N}{FV} \\ c_{e,f} = \frac{N_0 - N}{V(1-F)} \end{cases} \tag{3.17}$$

being $N_0$ the total number of molecules, $N$ the number of molecules that enter the cell, $V$ the total volume of the suspension and $F$ the cell volume fraction. If we express the final intracellular concentration as a fraction of the initial extracellular concentration $c_{i,f} = a \cdot c_{e,i}$, then from 3.17:

$$a = \frac{c_{i,f}}{c_{e,f}} = \frac{N(1-F)}{N_0 F} \tag{3.18}$$

On the other hand, from Eq. 3.17, the relationship between final and initial extracellular concentration is:

$$\frac{c_{e,f}}{c_{e,0}} = \frac{N_0 - N}{N_0} \tag{3.19}$$

Combining 3.18 and 3.19 we can obtain an expression of the term $c_{e,f}/c_{e,0}$ as a function of $F$ and $a$:

$$\frac{c_{e,f}}{c_{e,0}} = \frac{1 - F(1+a)}{1-F} \tag{3.20}$$

Then, for a cell volume fraction of 0.2 and a final intracellular concentration of 5% the initial extracellular concentration, the variation of the extracellular concentration is 1.25%.

Chapter 4

# The potential role of electroporation in pulsed radiofrequency treatments

**Abstract** — Pulsed radiofrequency treatments (PRF) for chronic pain consist in the delivery of a train of sinusoidal bursts in the radiofrequency range directly to the targeted nerve. Two decades after its conception and despite numerous clinical evidences of its efficiency in mitigating pain, the mechanism of action of the treatment remains unclear. Several studies have been performed to investigate the biological responses after the treatment. However, very little is known regarding the biophysical mechanisms by which the electric bursts trigger those responses. Since most of the effects that have been reported could be initiated by a calcium influx into the neurons, we hypothesized that PRF may induce a mild electroporation of the cell membrane causing a calcium uptake. This chapter presents the results of an *in vitro* study that was performed to test this hypothesis. Our results show that a single PRF burst can cause a calcium influx at significantly lower electric fields than those required to detect the uptake of larger molecules (Yo-Pro-1). By delivering multiple bursts the electric fields required to induce the same effects significantly decreased. In addition, we provided evidences that the observed effects depend on the TMV induced to the cells and they are not caused by thermal effects.

Part of the contents of this chapter is adapted from:

B. Mercadal, R. Vicente and A. Ivorra "The potential role of electroporation in Pulsed Radiofrequency treatments for chronic pain: exposure to radiofrequency bursts causes an uptake of calcium but not of Yo-Pro-1" [In preparation]

## 4.1 Introduction

Pulsed radiofrequency (PRF) treatments consist in the delivery of a train of sinusoidal electrical bursts (5-20 ms length) in the radiofrequency range (500 kHz) at a repetition rate of a few hertz (2-5 Hz). This treatment modality has proved to be effective in managing pain in patients suffering chronic pain when applied: directly to the affected nerve [161], adjacent to the dorsal root ganglion [162] and intraarticular [163]. Nowadays the most common pathologies for which PRF is indicated are radicular pain, trigeminal neuralgia, occipital neuralgia and shoulder and knee pain [164].

PRF originated from conventional thermal radiofrequency treatments as researchers were seeking for a less destructive radiofrequency based treatment to be applied to the afferent nervous pathways [6]. Two decades after its conception and despite multiple evidences of its effectiveness [164], the exact mechanism of action of PRF has not been revealed yet. There are several evidences that the analgesic effect of PRF is neither related to thermal effects nor to a permanent physical neural damage [165–168]. Currently most studies suggest that PRF induced pain relief is due to an alteration in the synaptic transmission or in the excitability of C-fibers through a neuromodulatory-type process [169–171].

Animal studies have exhibited several biological effects of PRF. Some studies have shown morphological changes in the inner structures of axons [165, 172–174]. Other studies have reported molecular effects such as: alterations of cellular activity [175] and gene expression [176–179], an increase in the expression of inflammatory proteins [173] and the inhibition of extracellular signal-regulated kinasses [180]. In addition, evidences of a long-term depression effect were found in a recent study [181]. These findings have lead to several possible explanations on how PRF inhibits the transmission of pain signals from a biological perspective. However, there has been little progress in elucidating the underlying biophysical mechanisms by which the electric bursts produce these effects.

Interestingly, most of the effects reported after PRF treatments can be triggered by an increase in the cytosolic free $Ca^{2+}$ concentration. This may link PRF effects with a direct effect of the electric fields. In addition, PRF is applied at different regions of the afferent nervous pathways, therefore, a hypothetical cytosolic $Ca^{2+}$ concentration increase should take place through the same mechanism in all those regions. Taking all that into account, we hypothesize that PRF causes

a permeabilization of the neural membrane through a mild electroporation process leading to a $Ca^{2+}$ influx.

In the study presented here, we performed a series of *in vitro* experiments in order to test our hypothesis that the PRF electric fields can cause a $Ca^{2+}$ influx into cells.

## 4.2 Materials and methods

### 4.2.1 Cell culture

HEK-293 cells were grown in Dubelcco's modified Eagle's medium (Gibco, Dublin, Ireland) supplemented with 10% fetal bovine serum (Biosera, Ringmer, East Sussex, UK) and 1% streptomycin/penicillin (Panreac, Barcelona, Spain). Cells were incubated at 37°C in a humidified environment containing 5% $CO_2$. The day before performing the experiments, the cells were seeded into 4 well Nunc$^{TM}$ Lab-Tek$^{TM}$ chambered coverslips (Thermofisher, Waltham, MA, USA) and incubated overnight.

### 4.2.2 Fluorescence labeling and imaging

Fluorescence labeling, as well as most of the experiments, were performed using a physiological buffer consisting of 135 mM $NaCl$, 5 mM $KCl$, 2 mM $MgCl_2$, 10 mM HEPES, 10 mM glucose, 2 mM $CaCl_2$, (pH 7.4, 310 mOsm, conductivity 1.51 S/m). In the experiments with a calcium free extracellular medium, $CaCl_2$ was replaced by 2 mM EGTA (a $Ca^{2+}$ chelator). When indicated in the text, experiments were performed using a buffer with a low electric conductivity (10 mM $NaCl$, 250 mM Sucrose 5 mM $KCl$, 2 mM $MgCl_2$, 10 mM HEPES, 10 mM glucose, 2 mM $CaCl_2$, pH 7.4, 290-310 mOsm, conductivity 0.26 S/m). All these chemicals and reagents were acquired from Panreac.

To label cells for free cytosolic $Ca^{2+}$ imaging, growth medium was replaced by the physiological buffer and Calcium Green-1 AM (Invitrogen, Carlsbad, CA, USA) was added at a final concentration of 5 $\mu$M. Cells were incubated for 40 minutes at 37 °C before being washed thoroughly. Then, the solution was replaced by the desired buffer to perform the experiments. To assess membrane permeability to larger molecules, growth medium was replaced by the buffer and Yo-Pro-1 (Sigma Aldrich, Sant Louis, MO, USA) was added to a final concentration of 2 $\mu$M immediately before the experiments.

Images were acquired with a Leica DMI6000B (Leica, Wetzlar, Germany) inverted microscope using a 20× objective. Time series image stacks were captured through the Leica LAS X software. For the assessment of the transient $Ca^{2+}$ response, images were taken every 2 seconds for 30 seconds before the burst delivery and for at least 1 minute after the end of the treatments. When evaluating the uptake of Yo-Pro-1, images were taken every 30 seconds for at least 15 minutes after the treatments.

### 4.2.3 Electric burst delivery

The typical treatment protocol in clinical PRF treatments consists on a train of sinusoidal bursts (500 kHz) with a burst length of 20 ms and delivered at a repetition rate of 2 Hz for a few minutes (see Figure 4.1). In this study, cells were exposed to sinusoidal bursts of different frequencies keeping the length of the bursts to 20 ms in all cases. All treatments were performed at room temperature. The sinusoidal bursts were generated by an AFG3022B function generator (Tektronix, Beaverton, OR, USA) connected to a WMA-300 high voltage amplifier (Falco Systems, Katwijk aan Zee, The Netherlands). The set-up used to deliver the electric bursts to the cells consisted of an acupuncture needle (300 $\mu$m of diameter) and a stainless steel plate electrode located at the opposite side of the chamber acting as a reference electrode(see Figure 4.2). The needle was placed in contact with the bottom of the chamber and parallel to it. Finally, the voltage applied between the needle and the plate was measured by a digital oscilloscope (DSO1014A, Agilent, Santa Clara, CA, USA).

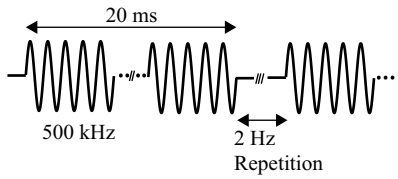


**Figure 4.1:** Typical PRF waveform used in the clinical practice

Typically, in experiments that involve the delivery of pulsed electric fields to cells, researchers use two parallel plates (or wires) in order to generate a relatively uniform and controllable electric field between them. In the present study, however, a different approach was taken in order to reproduce the temperature variations in the tissue during PRF treatments in a clinical setting. It has been shown that dur-

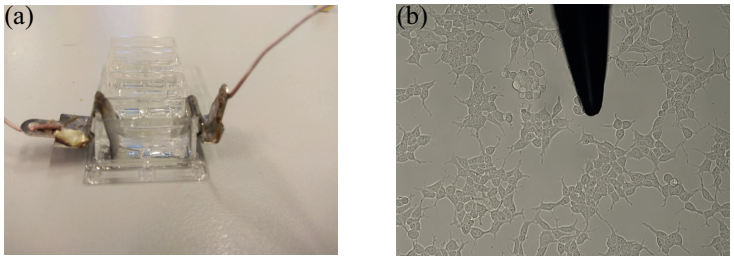


**Figure 4.2:** (a)Picture of the set-up used to deliver the electric bursts. (b) Microscopy image of the set-up showing the needle tip and the cells under study.

ing PRF treatments, the cumulative temperature increase around the electrode, although not irrelevant, is insufficient to create a thermal damage to the tissues [182, 183]. However, each burst generates a brief but large temperature spike that can reach 25°C at the tip of the electrode. Therefore, the electrode arrangement was chosen aiming to minimize the cumulative temperature increase in the buffer while generating large temperature spikes at each burst.

### 4.2.4 Image analysis and statistics

The acquired images were processed using Fiji [184] an open source software based on Image J [185]. Regions of interest (ROI) were created for each cell and the average fluorescence was measured for all time points. The average background fluorescence was subtracted to the fluorescence values obtained and the resulting values were converted to $\Delta F/F_0(\%) = 100 \cdot (F - F_0)/F_0$, where $F_0$ is the average fluorescence of the ROI before the burst delivery and $F$ is the fluorescence of the ROI at the considered time step.

To analyze the transient calcium response to the bursts, the time evolution of $\Delta F/F_0$ was processed in MATLAB (Mathworks Inc, Natick, MA, USA). Cells were classified based on whether or not they exhibited a calcium peak. In order to detect calcium peaks, the time derivative of the fluorescence was calculated and a threshold was applied to its maximum value. If the maximum of the derivative was above the threshold, first the position of the maximum was checked and only those cases whose maximum took place after the burst were considered. Finally the average fluorescence signal of the 10 following seconds was calculated. Only those peaks whose average was more than 3 times higher than the standard deviation of the signal before the burst delivery were counted. This detection process aimed at minimizing the number of spontaneous calcium spikes or image artifacts

counted as responses to the bursts.

In the case of Yo-Pro-1 uptake, a threshold was applied to the final fluorescence average in the cells in order to decide whether or not the dye was internalized by the cells.

The electric field exposure of each cell in the different experiments was estimated through a numerical model. The geometry of our set-up was simulated in COMSOL by defining an arbitrary 1 V voltage difference between the needle and the plate (See Figure 4.3). The steady state solution of the problem was calculated using the electric currents module of COMSOL. Then the results were scaled to the desired voltage to generate electric field maps for each of the applied voltages and extract the electric field exposure of each cell. These electric field values were assigned based on the position of the cells relative to the needle tip. To calculate these relative positions, first, the position of the needle tip was obtained from brightfield images captured before the delivery of the bursts. Second, the position of each cell was calculated by measuring the position of the center of the ROIs. Then, using these two values the relative positions were calculated. Finally, an electric field value was assigned to the ROI by searching for the closest point to the relative position in the electric field maps generated previously.

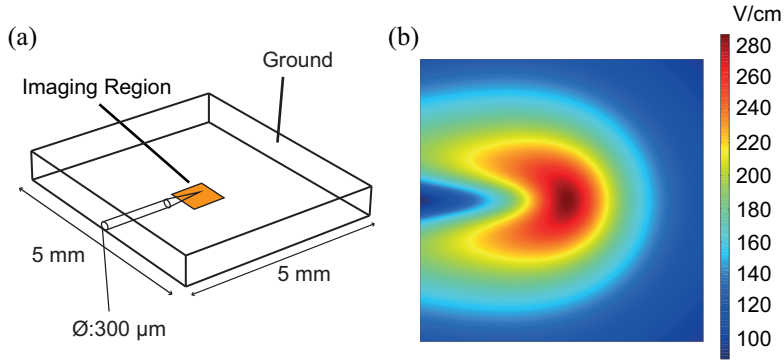


**Figure 4.3:** (a)FEM model geometry. (b) Electric field distribution within the imaging region when a voltage of 30 V is applied between the needle and the plate.

All the processing explained above led to a series of data consisting in an electric field exposure and a binomial response for each cell (either relative to $Ca^{2+}$ or to Yo-pro-1). In order to interpret these data and compare the different treatments, a logistic regression adjustment was

performed to these data:

$$p(E) = \frac{1}{1 + exp\,(-(\beta_0 + \beta_1 \cdot E))} \tag{4.1}$$

Where $p(E)$ is the probability of a cell to show a calcium peak as a function of the electric field exposure, $E$. The values of the parameters $\beta_0$ and $\beta_1$ were adjusted using the R-3.5.3 software package [186]. For each treatment protocol and conditions at least 15 different experiments were conducted and 40-80 cells were analyzed in each experiment.

### 4.2.5 Temperature measurement

Rhodamine B (Sigma Aldrich), a temperature sensitive dye, was used to measure the evolution of the temperature in the medium during the delivery of the electric bursts. The fluorescence of this molecule decreases with temperature [187], and its practically not affected by the external pressure and pH above pH values of 6 [188].

Rhodamine B was dissolved in our buffer to a final concentration of 100 $\mu$M and the solution was added into empty chambered coverslips at the same volume used in the experiments with cells. To measure the temperature evolution during the electric treatments, trains of bursts were delivered using the exact same set-up as the experiments explained above. Simultaneously, fluorescence images were taken every 100 ms with a Leica DMI6000B inverted microscope using a 20× objective. The images obtained were analyzed using Image J. At each time point, the average fluorescence in a region close to the needle tip was measured.

In order to convert the measured fluorescence values to temperature, a calibration procedure was carried out for our set-up. The solution was gradually warmed as follows: two stainless steel plates were placed at opposite sides of the chambered coverslips and were connected to the amplifier. A continuous 500 kHz waveform was generated in order to warm the solution by Joule heating. Images were taken every 15 seconds while simultaneously measuring the temperature using a thermistor. The temperature was increased from room temperature to 50°C within an approximately 15 minutes time span. This process was repeated in 8 independent experiments. Finally, the acquired fluorescence intensity values as a function of the temperature were used to adjust a second-degree polynomial with the least squares method.

### 4.2.6 Simulation of the induced transmembrane voltage

The TMV induced by the electric fields applied in our experiments was calculated by numerical modeling. To do so, realistic 3D geometrical models of the cells were constructed from confocal microscopy images. First, for membrane detection, cells were stained for 20 min in ice with 100 $\mu$g/ml concanavalin A tetramethylrhodamine (Invitrogen) and then fixed with 4% paraformaldehyde in PBS. Digital images were taken using a Leica TCS SP8 confocal microscope (Leica, Wetzlar, Germany). Cross section images of the cells were obtained by shifting the microscope focus at constant steps (0.3-0.6 $\mu$m) from the bottom of the cell to the top. The acquired image stacks were imported to Fiji, and 3D surfaces were constructed using the 3D viewer application of Fiji [189]. Then, these surfaces were smoothed and converted to solid using Meshmixer (Autodesk Inc, San Rafael, CA, USA). Finally, the smoothed surfaces were imported to COMSOL and the induced TMV was calculated by FEM using the *Electric currents* module and a frequency domain study. The simulations were performed following a similar procedure as described in section 3.2. The cell membrane was modeled with Eq. 3.4. The extracellular conductivity was set to 1.51 or 0.26 S/m (values measured for our buffers) and the rest of electrical properties were defined as in section 3.2 (Table 3.2).

## 4.3 Results

First of all we exposed the cells to PRF bursts (500 kHz, 20 ms length) and compared the effects of a single burst with the effects of 120 bursts (delivered at a frequency of 2 Hz) in terms of the free cytosolic $Ca^{2+}$ concentration and the uptake of Yo-pro-1. The results depicted in Figure 4.4 show the probability of the cells to display a peak as a function of the electric field according to the logistic regression (Eq. 4.1) obtained by fitting the data. After a single burst, the electric field having a probability of 0.5 to cause a $Ca^{2+}$ peak ($E_{50}$) is 480 V/cm. Yo-pro-1 uptake, on the other hand, was almost nonexistent after a single burst in the range of electric fields used in our study. When multiple bursts are delivered to the cells, the $E_{50}$ values obtained either for a $Ca^{2+}$ peak or Yo-Pro-1 uptake significantly decrease. In this case, the $E_{50}$ values obtained are around 330 V/cm and 880 V/cm for a $Ca^{2+}$ peak and Yo-Pro-1 uptake respectively. The same treatments were delivered in the absence of extracellular $Ca^{2+}$ and no changes in cytosolic $Ca^{2+}$ concentration were detected.

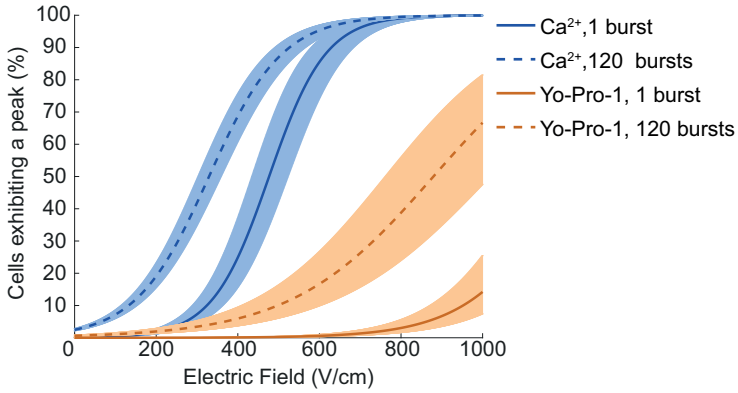


**Figure 4.4:** Probability of a cell to exhibit a $Ca^{2+}$ peak or Yo-Pro-1 uptake as a function of the electric field as obtained by fitting a logistic regression to our experimental data. The results are presented as the probabilty function obtained from the logistic regression (line) ± standard error (shaded region).

The temperature of the medium during the delivery of successive bursts at a repetition rate of 2 Hz was measured. Figure 4.5(a) shows the results obtained within the calibration process as well as the second-degree polynomial that better fitted with the results. Once the set-up was calibrated the same treatments with multiple bursts as in Figure 4.4 were applied. The fluorescence of Rhodamine B was average over an area close to the needle tip (see Figure 4.5(b)). Figure 4.5(c-d) show the temperature evolution over time obtained with the lowest and the largest voltages amplitudes applied in our experiments(40 and 70 V). The cumulative temperature increase did not exceed 4.5 °C in any case.

Wingle bursts with different frequencies were applied. The results, presented in Figure 4.6, show a clear dependence of the effects on the frequency. The $E_{50}$ values to induce a $Ca^{2+}$ peak are approximately 400, 480 and 700 V/cm, for 10 kHz, 500 kHz and 2 MHz respectively.

The effect of the extracellular medium conductivity was also assessed. Figure 4.7 shows the results obtained by delivering single bursts of frequencies of 10 kHz and 500 kHz using two buffers with different conductivity (1.51 S/m and 0.26 S/m). While the responses are almost identical for 10 kHz regardless of the medium conductivity, a significant difference is observed for 500 kHz. When the cells are treated in the low conductivity buffer, the obtained $E_{50}$ increases to 1020 V/cm for a single 500 kHz burst.

Finally, a realistic geometrical model of our cells was built in order to

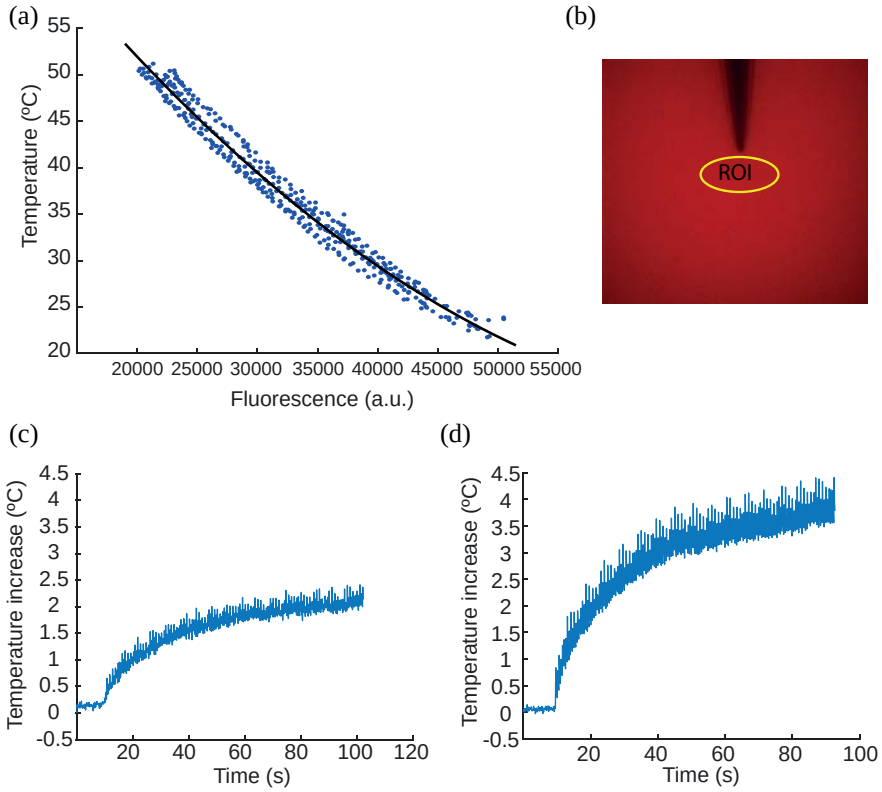


**Figure 4.5:** (a)Fluorescence intensity vs temperature obtained for our set-up and a second-degree polynomial adjusted by the least squares method (black line). The polynomial that better fitted the results was: $y = 1.22 \cdot 10^{-8}x^2 - 1.86 \cdot 10^{-3}x + 84.3$ ($R^2 = 0.98$) (b) Region of interest where the fluorescence values were averaged (c) Temperature increase with time when bursts (500 kHz, 20 ms) with an amplitude of 40 V are delivered at 2 Hz. (d) Temperature increase with time when bursts (500 kHz, 20 ms) with an amplitude of 70 V are delivered at 2 Hz

calculate the induced TMV in our experiments. The induced TMV was simulated with a FEM model for different frequencies and the two extracellular conductivity values used in our experiments. The results, presented in Figure 4.8, show a decrease of the TMV with the frequency as expected. In addition, the induced TMV decreases at lower frequencies when cells are surrounded by the low conductivity extracellular medium.

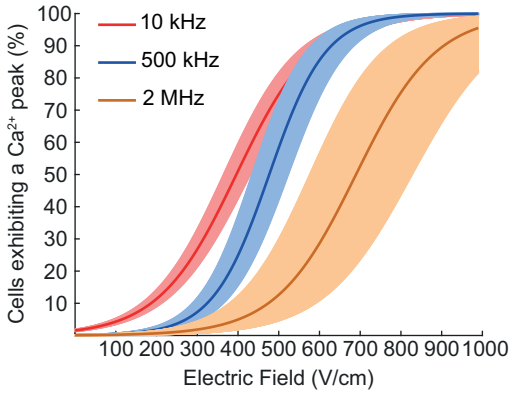


**Figure 4.6:** Effect of the frequency: Probability of a cell to exhibit a $Ca^{2+}$ peak as a function of the electric field for different frequencies (20 ms burst length in all cases). The results are presented as the probability function obtained from the logistic regression (line) ± standard error (shaded region).

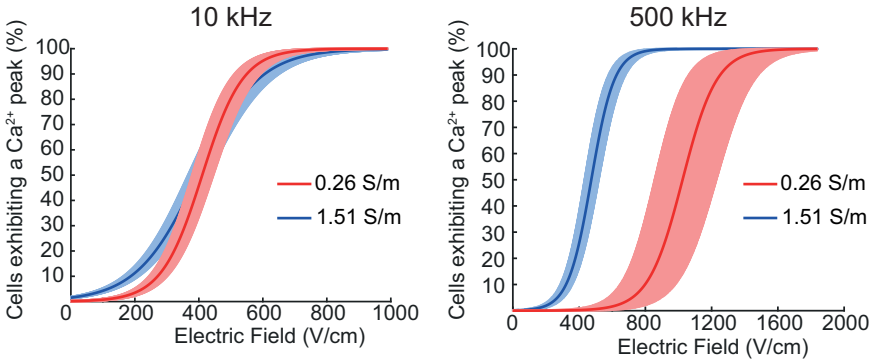


**Figure 4.7:** Effect of the extracellular conductivity: Probability of a cell to exhibit a $Ca^{2+}$ peak as a function of the electric field for two different frequencies and electrical conductivities of the external medium (20 ms burst length in all cases). The results are presented as the probability function obtained from the logistic regression (line) ± standard error (shaded region).

## 4.4 Discussion

### 4.4.1 General discussion

Our results show that the PRF bursts can cause an increase in the intracellular $Ca^{2+}$ at electric fields significantly lower than those required to internalize Yo-Pro-1. The fact that no increase was detected in the absence of extracellular $Ca^{2+}$ suggest that the observed increase in $Ca^{2+}$ concentration is due to an uptake from the extracellular medium. One of the characteristic features of PRF treatments

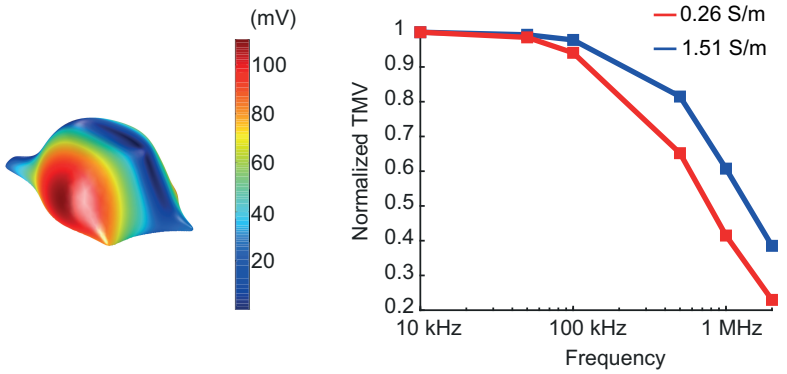


**Figure 4.8:** Induced TMV calculated by a FEM model of the cell geometry. The left image shows the maximum induced TMV amplitude (in mV) when PRF bursts with an electric field amplitude of 100 V/cm are delivered to a HEK cell. The right plot shows the normalized maximum TMV (with respect to the value at 10 kHz) induced to the cells as a function of the frequency of the bursts and the extracellular conductiviy)

in the clinical practice is the large amount of bursts that are delivered and according to our results, the delivery of multiple bursts significantly reduces the electric field amplitude required to observe a $Ca^{2+}$ peak.

The temperature increase during our experiments was low (less than 4.5 °C), and therefore, the $Ca^{2+}$ peaks observed cannot be attributed to a cumulative temperature increase. PRF bursts, although not causing thermal damage to the tissues, generate large temperature spikes at each burst in a clinical set-up[182, 183]. It has been shown that the large temperature spikes generated by infrared laser pulses can cause the excitation of peripheral nerves [190], as well as a $Ca^{2+}$ uptake and even Yo-Pro-1 internalization [191]. Our results show that the cell response largely depends on the frequency, which prevents associating the $Ca^{2+}$ influx observed in our experiments with the temperature spikes. Since the burst length was maintained in all experiments, the generated temperature spikes are expected to be the same in all frequencies. Thus, if our results were due to the temperature spikes the effect of the burst frequency should be very weak.

Finally, the cell response dependence on the frequency and on the extracellular conductivity suggest that the observed $Ca^{2+}$ influx is related to a TMV dependent effect. Indeed, if we compare the results with the induced TMV calculated numerically, the trends observed experimentally are consistent with the results of the simulations. First, we showed experimentally that higher frequencies require higher elec-

tric fields to induce the same effect. Which is consistent with the TMV dependence with frequency. Second, at 10 kHz the effects are very similar regardless of the medium conductivity, however, at 500 kHz the cells treated in a low conductivity medium required significantly larger electric fields to show the same responses. This is also consistent with the induced TMV dependence on the external conductivity.

The cells used in our experiments endogenously express very few voltage gated Ca2+ channels [192]. Thus, our results seem to support an electroporation mediated $Ca^{2+}$ uptake due to the delivery of PRF bursts. However, the possibility that the observed $Ca^{2+}$ influx took place through ion channels cannot be completely ruled out and further research would be needed in order to elucidate the exact pathways of the $Ca^{2+}$ influx.

### 4.4.2 Potential role of electroporation in PRF

The effects of $Ca^{2+}$ in cells have been extensively studied in the last decades and it is known that even a small amount of $Ca^{2+}$ ions can trigger a wide variety of neuronal changes [113]. On the one hand, local increases in $Ca^{2+}$ concentration can lead to alterations in synaptic function locally at the regions of $Ca^{2+}$ influx. On the other hand, besides local effects, a $Ca^{2+}$ influx can activate signaling pathways that affect the expression of several activity-regulated genes in neurons.

After in vivo PRF treatments several alterations in gene expression have been reported. Most of these alterations are consistent with a $Ca^{2+}$ influx as is the case of c-fos [193], BDNF [194] and ATF3 [195]. In addition, an increase in the cytosolic $Ca^{2+}$ concentration is consistent with the ultrastructural changes reported in axons after PRF exposure such as the disruption of neurofilaments [196] and changes in the morphology of mitochondria [197].

Electroporation was already suggested as being involved in the mechanism of action of PRF [183]. However, the suggested participation of electroporation was not related to $Ca^{2+}$. It was suggested a direct effect on neural conduction though a transient disruption of the membrane. Indeed, it is known that electroporation can transiently block neuronal conduction [108]. A recent study showed evidences of a long term depression effect after PRF treatments [181]. This finding is aligned with the results reported by Cahana et al. [198] which to the best of our knowledge is the only in vitro study on PRF effects available in the literature. In that study the authors showed that PRF causes a transient inhibition of evoked synaptic activity in hip-

pocampal slice cultures. In both cases the the reduction in the evoked synaptic activity that the authors attributed to a long term depression is also consistent with a conduction block caused by electroporation. Nevertheless, the hypothesis that PRF effects rely on a conduction block due to electroporation has two major flaws: first, it is inconsistent with the long lasting effects of PRF (several months) [164] and, second, the electric field required to block neuronal conduction through electroporation is very high compared to the electric fields generated in PRF treatments [182, 183]. In contrast what we propose is a "mild" electroporation phenomenon in which membrane permeability is increased during each PRF burst allowing $Ca^{2+}$ ions to enter the cell. The effects of PRF would not be a direct consequence of membrane electroporation but an indirect consequence of the events and cell responses triggered by the massive ion influx.

When square pulses are applied, the extent of membrane permeabilization and the resealing time depends on the duration of the applied pulses [199]. The shorter the pulses are, the smaller the pores that are created and the faster those pores reseal. This effect is clearly seen when pulses in the nanosecond range are applied [200] where the electric field required to allow the entry of large molecules such as propidium iodide is significantly higher than the required to observe a $Ca^{2+}$ influx. In the case of PRF, the sine waves in each burst can be regarded as a succession of short pulses (1 $\mu$s in each semi-cycle) with alternating polarity. In this scenario we expect mostly small sized and short lived pores to be created allowing the transport of ions but not larger molecules. In fact, we showed that significantly larger electric fields are required in order to cause Yo-Pro-1 uptake by PRF bursts.

It has been shown that the effects of PRF can be enhanced by increasing the applied voltage [201] which is consistent with the electroporation hypotheses. However, PRF applied directly to nerves has shown to selectively affect small unmyelinated C fibers and spare larger and myelinated A-$\delta$ and A-$\beta$ fibers [174]. Electroporation is expected to have a non-selective effect or even affect preferentially the larger myelinated fibers due to their size. This apparent contradiction with the electroporation hypotheses might be explained by the myelin sheath allowing $Ca^{2+}$ entry only in a limited area (the nodes of Ranvier) in A-$\delta$ and A-$\beta$ fibers while a larger area of C fibers can be permeabilized. Another possible explanation might be related to a higher capacity to recover normal conditions of larger fibers after PRF application.

## 4.5 Conclusions

We showed that PRF bursts can cause a $Ca^{2+}$ influx. Our results are consistent with our initial hypothesis that PRF causes a $Ca^{2+}$ uptake mediated by a "mild" electroporation of the cell membrane. However, further research is needed in order to elucidate the exact mechanisms of the observed $Ca^{2+}$ influx. The results of this study may link the effects of PRF reported by other authors with a direct action of the electric fields in neurons.

Chapter 5

# Avoiding nerve stimulation in irreversible electroporation

**Abstract** — Electroporation based treatments consist in applying one or multiple high voltage pulses to the tissues to be treated. As an undesired side effect, these pulses cause electrical stimulation of excitable tissues such as nerves and muscles. This increases the complexity of the treatments and may suppose a risk to the patient. To minimize electrical stimulation during electroporation based treatments, it has been proposed to replace the commonly used monopolar pulses by bursts of short bipolar pulses. In this chapter, we numerically analyze the rationale for such approach. Different pulsing protocols are compared in terms of their electroporation efficacy and their capability to trigger action potentials in nerves. For that, we developed a modeling framework that combines numerical models of nerve fibers and experimental data on irreversible electroporation. Our results indicate that, by replacing the conventional relatively long monopolar pulses by bursts of short bipolar pulses, it is possible to ablate a large tissue region without triggering action potentials in a nearby nerve. Our models indicate that this is possible because, as the pulse length of these bipolar pulses is reduced, the stimulation thresholds raise faster than the irreversible electroporation thresholds. We propose that this different dependence on the pulse length is due to the fact that transmembrane charging for nerve fibers is much slower than that of cells treated by electroporation because of their geometrical differences.

Part of the contents of this chapter is adapted from:

B. Mercadal, C. B. Arena, R. V. Davalos. and A. Ivorra "Avoiding nerve stimulation in irreversible electroporation: A numerical modeling study" *Phys. Med. Biol.*, vol. 62, no. 20, pp. 8060–8079, 2017.

URL: https://www.ncbi.nlm.nih.gov/pmc/articles/PMC5744675/

DOI: 10.1088/1361-6560/aa8c53

## 5.1 Introduction

In vivo electroporation is the basis of multiple clinical treatment modalities (see section 2.2.4). One of the main drawbacks of electroporation based treatments is the appearance of electrical stimulation of the excitable tissues during the delivery of the electroporation pulses (see section 2.4.1). Recently, it has been proposed a novel treatment protocol based on replacing the 100 $\mu$s monopolar pulses that are typically used by bursts of bipolar pulses with the same energized time and a short pulse length (1 or 2 $\mu$s) [7]. It has been demonstrated that this technique, coined "high-frequency irreversible electroporation" (H-FIRE), is able to successfully ablate regions of tissue while practically avoiding muscle contractions [7, 105]. The promising results obtained in the first trials with the H-FIRE protocols led to a series of experiments to study the electroporation efficiency of high frequency bursts of bipolar pulses and their potential uses in clinical applications [107, 202–204]. However, a clear explanation on how these waveforms can prevent muscle contractions while maintaining treatment efficacy does not exist.

The two main goals of the study presented in this chapter were: 1) to gain understanding on why bursts of bipolar pulses which are capable of inducing IRE do not cause neuromuscular stimulation and 2) to identify which pulsing protocols may be most suitable in order to minimize stimulation while maximizing IRE.

## 5.2 Materials and Methods

Figure 5.1(a) illustrates the general scenario considered in this study: an electroporation treatment is delivered to a tissue by applying high voltage pulses across two needle electrodes. Inside the tissue to be treated, or nearby, nerves and nerve terminations may be present.

Two nerve stimulation cases were modeled here (see Figure 5.1(b)): 1) a long nerve fiber propagating close to the treated region, and 2) a nerve termination close to the treated region. Under the assumption that the long nerve fiber corresponds to a motor neuron, the first case allowed comparison of different pulse protocols in terms of the maximum volume of tissue that can be ablated before an action potential is triggered in that nerve fiber and neuromuscular stimulation occurs. For performing such comparison, first it was modeled the response of a nerve fiber in the vicinity of the treated area to determine the maximum voltage across the needles that does not trigger an action

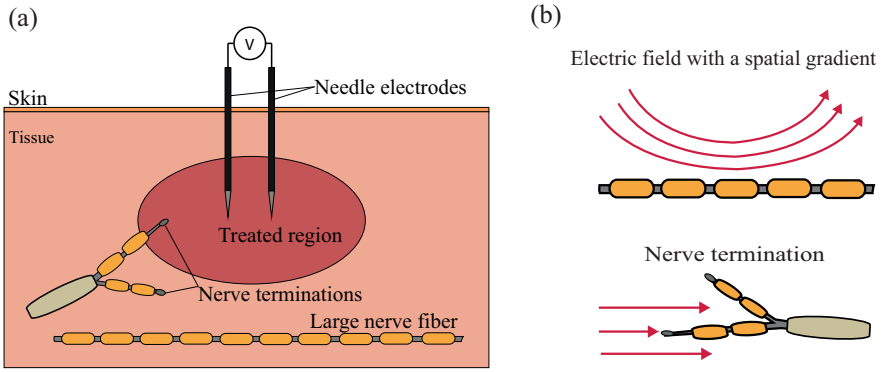


**Figure 5.1:** (a) Schematic representation of the general electroporation scenario considered in the present study. (b) Modeled excitation modes of a nerve.

potential. Then, this voltage was used to estimate the volume of tissue that could be ablated without initiating an action potential.

The second case would represent the activation of pain receptors [205]. This case, unlike the long nerve fiber case, entails stimulation under the presence of a homogeneous electric field. This scenario, despite not being strictly realizable (electric field will always present a spatial gradient in an electroporation clinical setup), is of interest to the present study as will be seen in the next sections.

### 5.2.1 Modeled pulsing protocols

In order to model the response of a nerve fiber or a nerve termination to different pulsing protocols, it was first modeled the electric potential distribution in tissue generated by two needle electrodes with a voltage difference between them. This was done with COMSOL. The needle electrodes were modeled as cylinders with a 1 mm diameter and 1.5 cm of height at a separation of 1 cm between them. The tissue was modeled as a homogeneous conductive medium with an arbitrary conductivity of 1 S/m. The conductivity was arbitrarily set because, for the nerve fiber and nerve termination models, it is only relevant the voltage distribution in tissue and, since the medium is modeled as homogeneous, the conductivity value does not affect the voltage distribution. The dimensions of the simulation space were $10cm \times 10cm \times 10cm$ and the complete model had 2581784 tetrahedral elements.

Voltage between the needles was arbitrarily set to 1 V and the electric potential at each point of the simulation space was computed through

the steady state solution in the *Electric currents* mode of the *AC/DC* module of COMSOL (*Stationary Study*) using the linear system solver *Pardiso*.

The obtained voltage distribution was linearly scaled to assay the response of a nerve fiber to different voltage waveforms (Figure 5.2) using the models described in the next section. For facilitating computation, the modeled pulses were not perfectly sharp; they included up and down linear ramps with a duration of 5% the pulse-length.

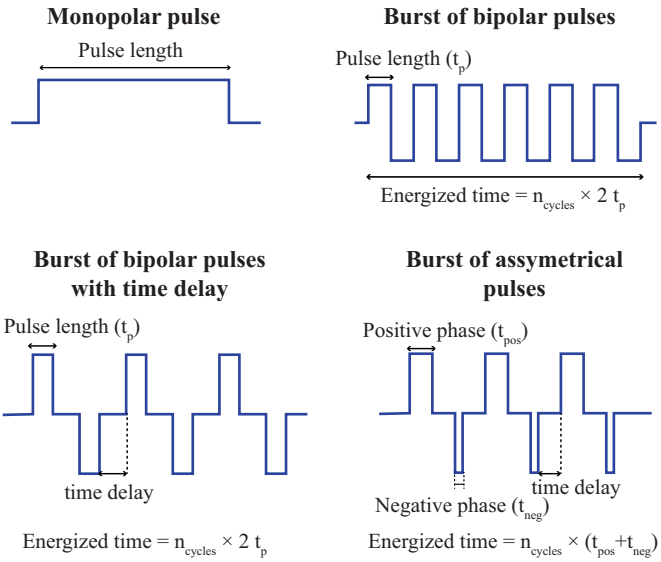


**Figure 5.2:** Waveforms considered in our study.

### 5.2.2 Nerve fiber and Nerve termination models

#### Nerve fiber model

The response of a nerve fiber to the voltage applied across the electrodes was determined using the cable model for a myelinated axon [86] (see section 2.3.5). Following this approach the TMV relative to the resting voltage ($V_n = V_{i,n} - V_{e,n} - V_r$) at the nth node of Ranvier can be calculated by solving the following equation:

$$\begin{aligned}\frac{dV_n}{dt} =& \frac{1}{C_m}[G_a(V_{n-1} - 2V_n + V_{n+1} + \\ &+ V_{e,n-1} - 2V_{e,n} + V_{e,n+1}) - I_{i,n}]\end{aligned} \tag{5.1}$$

where $V_{e,n}$ is the extracellular voltage at each node, $C_m$ is the membrane capacity, $G_a$ is the axoplasmic conductance, and $I_{i,n}$ is the ionic current across the membrane at each node. The ionic current was approximated as the sum of the current through 3 types of voltage gated ion channels plus a leakage current as in [206] (see section 5.6). Assuming that no axial current can exit at the end of the fiber (sealed end assumption) [207][208], the voltage at the extreme nodes is calculated as:

$$\begin{aligned} \frac{dV_1}{dt} &= \frac{1}{C_m}[G_a(-V_1 + V_2 - V_{e,1} + V_{e,2}) - I_{i,1}] \\ \frac{dV_N}{dt} &= \frac{1}{C_m}[G_a(-V_N + V_{N-1} - V_{e,N} + V_{e,N-1}) - I_{i,N}] \end{aligned} \tag{5.2}$$

Equations 5.1 and 5.2 and the equations describing the evolution of the ionic currents were integrated by the implicit backward Euler method in MATLAB. The values of $V_{e,n}$ for each configuration were taken from the solution of the FEM model introduced in the previous section. Since the voltage at each point is proportional to the voltage difference between the needles, any voltage difference can be tested by multiplying the values extracted from the FEM model. The parameters used in the model are listed in Table 5.1.

**Table 5.1:** Parameters used in the nerve fiber model

| Symbol | Value | Definition, justification or source |
|---|---|---|
| $\rho_a$ | $70\,\Omega \cdot cm$ | Axoplasmic resistivity [209] |
| $c_m$ | $2\,\mu F/cm^2$ | Nodal capacitance [85] |
| $L$ | $115 \cdot D$ | Internodal distance [210, 211] |
| $G$ | $1\,\mu m$ | Nodal length[212] |
| $D$ | $10\,\mu m$ | Fiber diameter |
| $d_a$ | $0.7 \cdot D$ | Axon diameter [212] |
| $d_n$ | $0.33 \cdot D$ | Node diameter [212] |
| $C_m$ | $c_m \pi d_n^2 G$ | Membrane capacity |
| $G_a$ | $\frac{\pi d_a^2}{4\rho_a L}$ | Membrane conductance |
| $V_{rest}$ | $-80\,mV$ | Resting voltage |

The position and orientation of the nerve fibers were chosen so as to maximize the second spatial derivative of the extracellular voltage as it has been identified that this value determines when stimulation occurs in the cable model of the nerve fiber [213]. Two different locations were studied (see Figure 5.3): first, a fiber parallel to the axis that joins the centers of the electrodes, placed at a small distance from

them. Second, a fiber inside the plane containing the electrodes and at a small distance beneath the electrodes. These situations correspond to worst case scenarios as it is in these situations when lower excitation thresholds are expected for a given voltage amplitude across the electrodes.

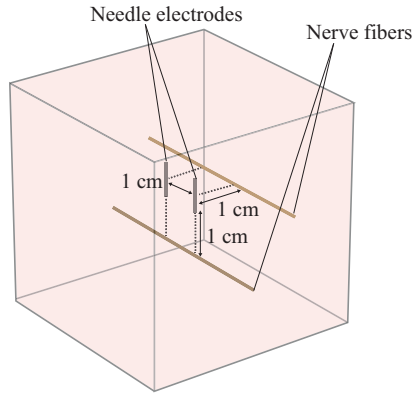


**Figure 5.3:** Model geometry used in the present study to simulate excitation of long nerve fibers (=myelinated axon). Two nerve fiber locations are analyzed: first, an axon parallel to the axis that joins the centers of the electrodes at a distance of 1 cm from them. Second, an axon inside the plane defined by the electrodes at a distance of 1 cm underneath them.

### Nerve termination in a homogeneus electric field

To simulate the response of a nerve termination in a homogeneous field, it was modeled a terminated short fiber with only 6 nodes. By employing the following equation, it was modeled the case in which the nodes are equidistant and aligned in parallel the homogeneous electric field [205]:

$$V_{e,n} = V_{e,1} + ELn \tag{5.3}$$

where $E$ is the electric field magnitude, $L$ the distance between successive nodes and $V_{e,1}$ a reference voltage at the ending node. The value of voltage ($V_{e,1}$) has no impact on the response of the cable model and, for convenience, it was set to zero. After defining the voltages in the nodes with the above equation, the procedure to determine the nerve termination response was the same as in the previous section. First, this voltage distribution was scaled to assay different field magnitudes and waveforms. Then, the same model, including the fiber parameters (see Table 5.1), was used to model the ionic currents and the TMV. However, a smaller fiber diameter of 1 $\mu$m was defined in order to

model sensory fibers, which have smaller diameters than motor fibers. Finally, the problem defined by equations 5.1, 5.2 and 5.3 was solved following the same methodology as in the previous section.

### 5.2.3 Determination of stimulation thresholds

The stimulation threshold for a given configuration was found through binary search until a maximum relative difference of 1% between a voltage that initiates an action potential and a voltage that does not was found. It was determined that an action potential had been triggered when the sodium current across the membrane showed a large and fast increase at in least one node. This increase was detected by monitoring the gating parameters that drive the fast sodium current, m and h (See section 5.6).

The time step used to integrate the equations can have a significant influence in the stimulation threshold results, especially when simulating high-rate variation waveforms as is the case in the present study [214]. To select the time step for each waveform type, simulations using the shortest pulse length were run and the time step was reduced until the relative difference on the excitation thresholds obtained in the subsequent simulations was negligible (taking into account that the search of the threshold is performed with a tolerance of a 1%). The largest time step that was found to provide stable results was 5 nanoseconds.

### 5.2.4 IRE model

Tissue ablation was modeled using experimental data from the *in vitro* experiments by Sano et al. [203](See Table 5.2). In that study, measurements were performed in a 3D tumor mimic using PPT8182 murine primary pancreatic tumor cells. The treatments consisted in 120 bursts of bipolar pulses with an energized time of 100 $\mu$s a time delay of 2 $\mu$s and different pulse lengths.

For each configuration and pulse protocol, the voltage difference between the needles was set to the stimulation threshold and the electric field at each point of the simulation space was calculated through the FEM model introduced previously. To calculate the ablation volume, the volume of tissue exposed to an electric field above the IRE threshold was integrated using the volume integration tool of COMSOL.

**Table 5.2:** IRE electric field threshold for a protocol consisting in 120 bursts with a total energized time of 100 $\mu$s and a time delay of 2 $\mu$s between pulses, as a function of pulse length, $t_p$. The data corresponds to measurements performed using PPT8182 murine primary pancreatic tumor cells in a tumor mimic [203].

| $t_p(\mu s)$ | $E_{IRE}$ (V/cm) |
|---|---|
| 100 | 501 |
| 50 | 531 |
| 10 | 629 |
| 5 | 640 |
| 2 | 755 |
| 1 | 1070 |
| 0.5 | 1687 |
| 0.25 | 2022 |

## 5.3 Results

### 5.3.1 Long nerve fiber

For illustration and for validating our implementation of the cable model for a myelinated axon, we first compared stimulation when applying a single monopolar pulse and when applying a burst of bipolar pulses in a given geometry (Figure 5.4(a)). Figure 5.4(b) shows the time courses of the TMV increase of the fiber at the node where an action potential is initiated when monopolar pulses and bursts of bipolar pulses are applied. It can be observed that, for the same voltage amplitude (100 V) and energized time (100 $\mu$s), a monopolar pulse easily triggers an action potential after about 70 $\mu$s whereas the equivalent burst of bipolar pulses is incapable of triggering an action potential as the membrane is charged and discharged repeatedly. Only after increasing the burst amplitude to 400 V it is possible to observe that an action potential is initiated. Figure 5.4(c) displays the stimulation threshold results for the two types of waveforms. The stimulation thresholds in both cases follow a linear relationship with the pulse length in a log-log plot, which is consistent with neurostimulation literature [215–217].

Note that the results in Figure 5.4(c) are presented as a function of the pulse length, meaning that a single monopolar pulse of a given pulse length is benchmarked against a full burst made up of bipolar pulses with that same pulse length reaching a total energized time of 100 $\mu$s. In other words, a single pulse is evaluated against a succession of equivalent positive and negative pulses that sum up a total energized time of 100 $\mu$s. The results show that the stimulation thresholds are

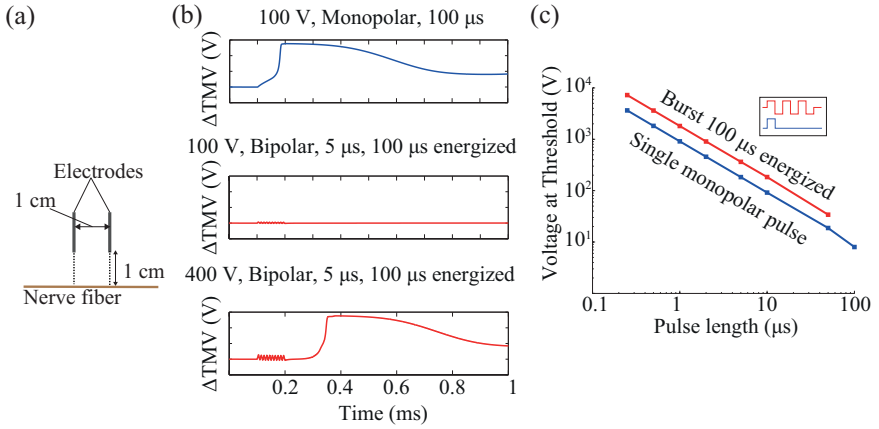


**Figure 5.4:** (a) Modeled geometry (b) Time evolution of the TMV increase with respect to the resting voltage when different pulses are delivered. Top, a 100 V monopolar pulse (starting at time = 0.1 ms) triggers an action potential. Middle, a burst of bipolar pulses with the same amplitude and energized time does not cause any response. Bottom, the same burst with a higher amplitude (400 V) triggers an action potential. (c) Minimum voltage amplitude across the electrodes able to trigger stimulation as a function of pulse length when a single monopolar pulse is applied and when a full burst of bipolar pulses with a 100 $\mu$s of total energized time is applied.

significantly larger when a burst of bipolar pulses is applied compared to a single monopolar pulse. This occurs for all pulse lengths, even though at short pulse lengths the total energized time of the full burst is significantly longer than the duration of the monopolar pulse.

For the two axons locations and the electrode configurations in Figure 5.3, Figure 5.5(a) shows the voltage stimulation thresholds when bursts of bipolar pulses with a 2 $\mu$s inter-pulse delay are delivered. The stimulation thresholds are presented as a function of the length of the pulses that make up the burst. In all cases the total energized time of the burst was set to 100 $\mu$s. The isolated points represent the stimulation thresholds for a conventional electroporation pulse (monopolar, 100 $\mu$s) and, unsurprisingly, deviate from the linear tendency that is seen for the rest of pulse lengths. In relative terms, the behavior of the stimulation thresholds does not depend significantly on whether the nerve fiber is beneath or beside the electrodes. Nevertheless, it is worth noting that the stimulation thresholds are lower when the nerve fiber is beside the electrodes

The stimulation thresholds in Figure 5.5(a) were used to estimate the maximum volume of tissue around the needles that could be ablated without initiating an action potential in the nerve fiber (Figure 5.5(b).

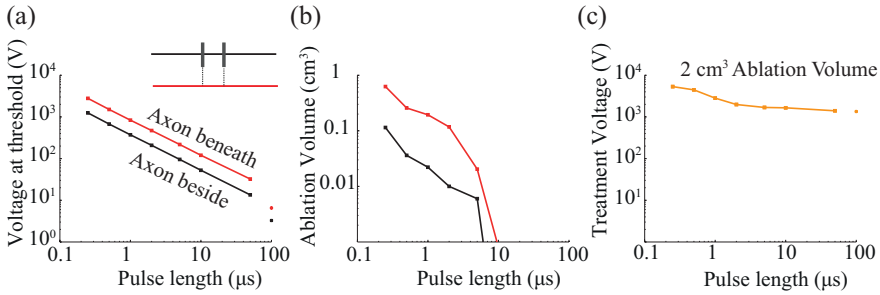


**Figure 5.5:** (a) Voltage stimulation thresholds versus pulse length for two different locations of the nerve fiber (see Figure 5.3) when bursts of bipolar pulses with a total energized time of 100 $\mu$s and with a 2 $\mu$s inter-pulse delay are delivered. (b) For the same axon locations, simulated ablation volume that would be achieved by applying a voltage difference between the electrodes equal to the corresponding stimulation thresholds. (c) Voltage difference between the electrodes in order to produce a 2 $cm^3$ ablation volume by means of IRE.

In both cases, the volume of tissue that theoretically could be ablated without stimulation greatly rises as the length of the pulses is shortened. As further explored in the next section and later discussed, this result can be explained as being the consequence of a steeper increase of the stimulation thresholds as the pulse length is reduced in comparison to the IRE thresholds increase. Indeed, it was computed the voltage necessary to produce a specific IRE ablation volume (2 $cm^3$) using the bursts of bipolar pulses considered before (Figure 5.1(c)), and the voltage shows a significantly lower increase when the pulse length is reduced compared to the stimulation threshold voltages in Figure 5.5(a).

### 5.3.2 Nerve termination

By modeling the response of the nerve termination under the action of a homogeneous electric field it is possible to directly benchmark IRE thresholds against stimulation thresholds for different pulsing protocols; for both phenomena it is possible to define an electric field magnitude threshold. Figure 5.6(a) displays the simulated stimulation thresholds for the nerve termination and the experimental IRE thresholds from [203] as a function of the pulse length. Nerve termination stimulation thresholds follow a linear relationship with pulse length in a log-log plot. IRE thresholds also exhibit a quite linear relationship with pulse length but, in this case, the slope is much more moderate. This result is aligned with the above observation: a steeper increase of the stimulation thresholds as the pulse length is reduced

in comparison to the IRE thresholds increase.

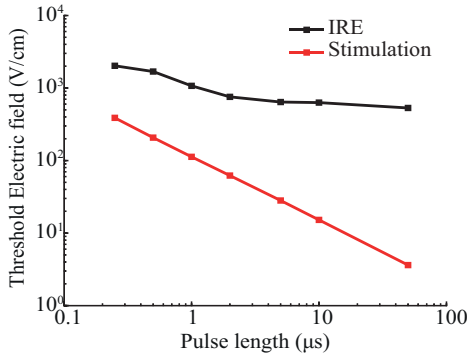


**Figure 5.6:** IRE thresholds for PPT8182 cells (from [203]) and stimulation thresholds for the modeled nerve termination when bursts of bipolar pulses with an energized time 100 $\mu$s and an inter-pulse delay of 2 $\mu$s are applied.

Since an electric field threshold can be defined both for stimulation and for IRE, it is possible to overlap the region that would be subjected to IRE to the region where existing nerve terminations would be stimulated. This was done in Figure 5.7. These plots show, for different pulse lengths and voltage amplitudes, the region where the FEM simulated field magnitude is above the IRE threshold (IRE) and the region where the electric field magnitude is above the stimulation threshold for the nerve termination (STIM). The represented plane corresponds to the cross-section perpendicular to the electrodes which intersects their centers. The amplitude of the voltage applied across the needles was heuristically adjusted in each case to obtain similar ablation areas. The results show that, by reducing the pulse length, the same ablation area can be achieved while reducing the area in which a nerve termination would be stimulated. In the case of a monopolar pulse, the area above the stimulation threshold is much larger than in the bursts of bipolar pulses examples. Using experimental data from [218] for two cell lines, it was decided to test other pulsing protocols for IRE thresholds and nerve termination stimulation. The results are displayed in Figure 5.8. Two additional protocols are compared: 100 bursts with an energized time of 100 $\mu$s and an inter-pulse delay of 1 $\mu$s (Figure 5.8(b)), and 100 bursts with 50 $\mu$s energized time and a delay between pulses of 1 $\mu$s (Figure 5.8(c)). For the reader's convenience, it is represented again the case for 120 bursts with 100 $\mu$s energized time and an inter-pulse delay of 2 $\mu$s (Figure 5.8(a)). Again, it can be observed a steeper increase of the

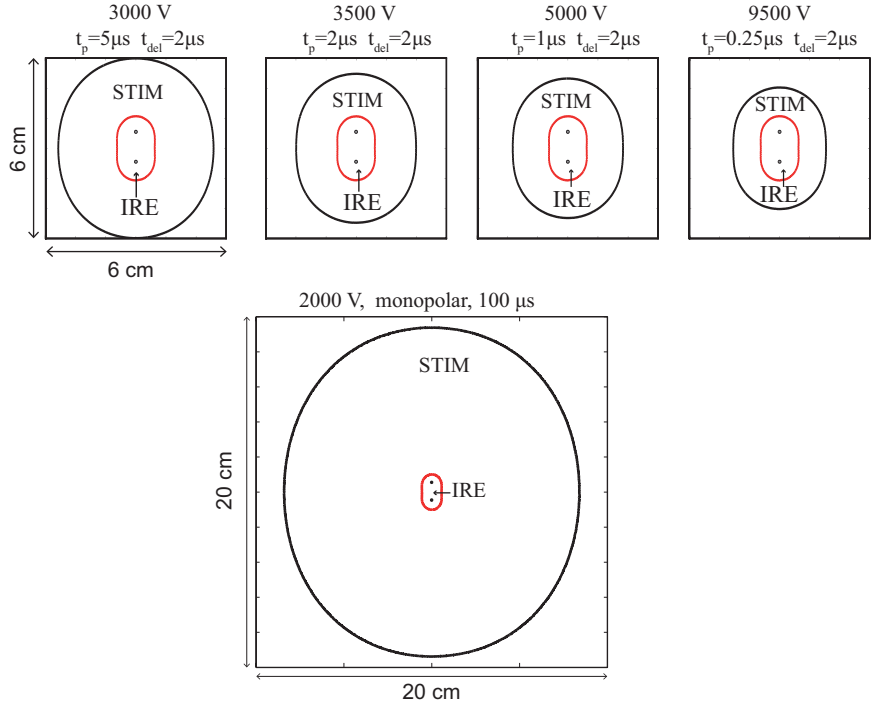


**Figure 5.7:** Simulated areas of ablation (IRE, red boundary) and of nerve termination stimulation (STIM, black boundary) for different pulse lengths and voltages across the needle electrodes. The voltage across the needles was adjusted to obtain a similar ablation area for each pulse length. The represented plane corresponds to the cross-section perpendicular to the electrodes which intersects their centers.

stimulation thresholds as the pulse length is reduced in comparison to the IRE thresholds increase

Bipolar pulses are less effective than monopolar pulses [219] in terms of the electroporation efficacy. For this reason, the delivery of bursts consisting of asymmetric bipolar pulses has been proposed and it has indeed been experimentally shown that they significantly reduce the IRE thresholds compared to bursts of regular bipolar pulses [218]. However, due to the charge imbalance of the asymmetric pulses, the stimulation thresholds are also likely to be significantly reduced. This contingency was also tested here. Table 5.3 shows the modeled stimulation thresholds for a nerve termination in a homogeneous field and the IRE thresholds from [218] for different waveforms. Although the IRE thresholds with asymmetric pulses are reduced about threefold compared to thresholds with symmetric pulses, the excitation thresholds are reduced in more than an order of magnitude. Therefore,

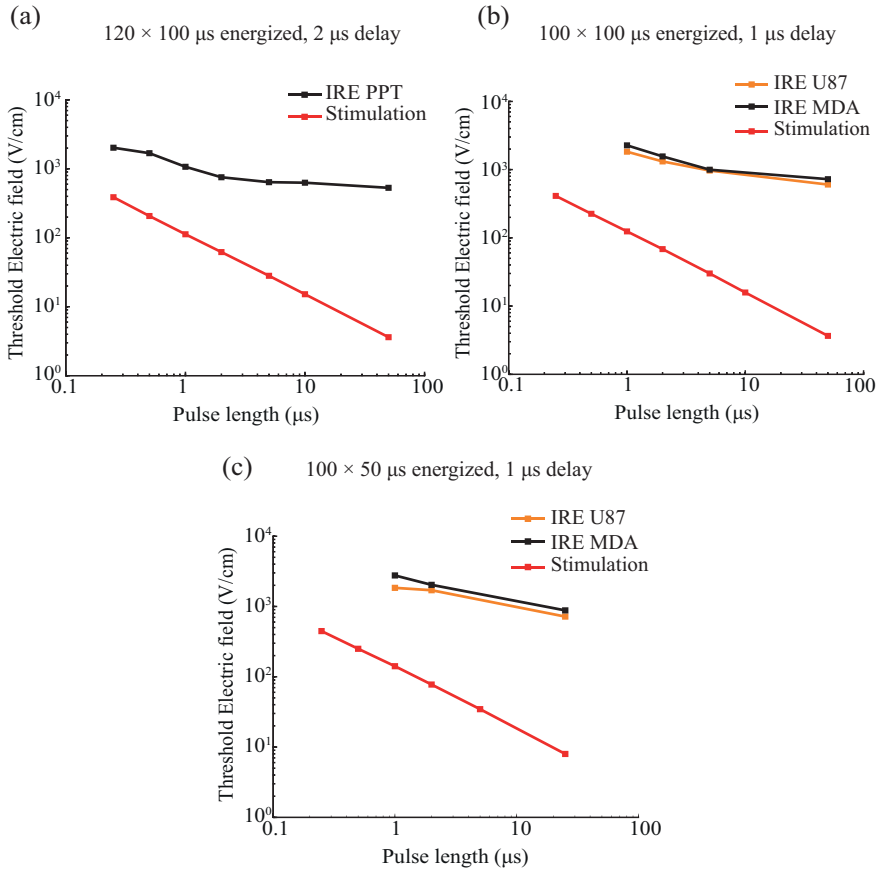


**Figure 5.8:** (a) Replica of Figure 5.6(a), IRE thresholds for PPT8182 cells (from ([203]) and stimulation thresholds for the modeled nerve termination when bursts of bipolar pulses with an energized time 100 $\mu$s and an inter-pulse delay of 2 $\mu$s are applied. (b and c) The same plot for U87 and MDA-MB-231 BR3 cells (IRE data from [218]) when bursts of bipolar pulses with an energized time of 100 $\mu$s and inter-pulse delay of 1 $\mu$s are applied (b) and when bursts of bipolar pulses with an energized time of 50 $\mu$s and an inter-pulse delay of 1 $\mu$s delay are applied (c).

these results suggest that the use of asymmetric bipolar pulses is not a worthwhile approach for minimizing unintended stimulation in electroporation protocols.

## 5.4 Discussion

### 5.4.1 General discussion

Our results indicate that, by replacing the conventional relatively long monopolar pulses by bursts of short bipolar pulses which achieve the

**Table 5.3:** IRE and stimulation thresholds for assymmetric waveforms. Waveforms are defined as positive phase-delay-negative phase. IRE thresholds data extracted from [218].

| Waveform ($\mu s$) | Stimulation (V/cm) | IRE, U87 (V/cm) | IRE, MDA (V/cm) |
|---|---|---|---|
| 5-1-5 | 30.0 | 967 | 998 |
| 5-1-0.5 | 1.0 | 541 | 826 |
| 5-1-0.25 | 1.5 | 484 | 812 |
| 2-1-2 | 68.4 | 1316 | 1563 |
| 2-1-0.5 | 2.2 | 700 | 885 |
| 2-1-0.25 | 1.8 | 594 | 818 |
| 1-1-1 | 124.4 | 1827 | 2271 |
| 1-1-0.5 | 4.1 | 1213 | 2000 |
| 1-1-0.25 | 2 | 780 | 945 |

same IRE efficacy, it is possible to avoid triggering action potentials in nearby nerve fibers or nerve terminations that otherwise would be stimulated. In other words, for the same ablation volume, less nerve fibers or nerve terminations would be recruited. This would have a positive impact on pain and neuromuscular stimulation during treatment, which is consistent with observations in previous in vivo studies [7, 105].

Our models indicate that the above is possible because, as the pulse length of the bipolar pulses is reduced, the stimulation thresholds raise faster than the irreversible electroporation thresholds.

The trends observable in Figures 5.5, 5.6 and 5.7 suggest that the ablation volumes that would be achieved without causing stimulation could be expanded with no limits by reducing the length of the delivered pulses. Nevertheless, in the present study we have not analyzed the thermal effects of the treatments, which are expected to be relevant, especially with short pulse lengths as very high electric fields would be required. Note that to produce a 2 $cm^3$ ablation with the shortest pulse length in Figure 5.5(c), the voltage difference between the electrodes was more than 5 kV. This voltage is higher than the clinically used values which usually do not exceed 3 kV. If an optimization study had to be performed for the pulsing protocol, our modeling framework would have to be upgraded to include thermal effects. This limitation of our study points out other limitations which are discussed below.

First, although electroporation protocols mostly consist in a sequence

of several pulses (or bursts), stimulation in our study is simulated for a single pulse (or burst). This is a reasonable simplification taking into account that, in the vast majority of the clinical electroporation protocols, the delivery of the pulses is done with a 1 second delay between them. Hence, it is a safe assumption to consider that previous pulses have an insignificant effect on neuron's excitability or at least on the threshold values.

Second, in the FEM model used to calculate the external voltage, we considered the medium to be homogeneous while in a real scenario this medium would be highly inhomogeneous, particularly around the nerve fibers. In addition the medium was considered to be purely conductive with a constant conductivity and it is agreed that electroporation alters the conductivity of tissues [220]; although such alteration is not as remarkable in the case of high frequency bipolar bursts as it is in the case of conventional pulses [221]. These circumstances significantly alter the electric field distribution and, normally, would have to be modeled in an electroporation study. Nevertheless, since the aim of the present study was to model the response of excitable cells in a general scenario in order to compare different pulsing protocols, for the sake of simplicity, these circumstances were ignored.

Third, the cable model only considers the TMV induced by the longitudinal component of the current (parallel to the axon) and neglects the transverse components (perpendicular to the axon). In long fibers, when the membrane charges to its steady state, the voltage induced by a longitudinal current is much higher than the voltage induced by a transverse current. Nevertheless, the membrane charging time is significantly longer for longitudinal currents [222]. This means that, when delivering long pulses, longitudinal currents are more effective to excite long fibers. However, below a certain pulse length ($\approx 100$ ns) the transverse currents can become dominant and generate action potentials with a lower current. Therefore, although the cable model is appropriate in our study (pulse lengths $> 100$ ns), other approaches would be necessary to study shorter pulse lengths.

At this point it is worth discussing about the dependence of IRE and stimulation thresholds on pulse length. Electroporation and nerve stimulation are both threshold-like phenomena dependent on the induced TMV, meaning that they occur when the membrane reaches a certain TMV; higher in the case of electroporation. Although the mechanisms of cell death by means of IRE are complex and can vary among different treatment protocols, it is widely accepted that IRE

can also be considered as a threshold-like phenomenon [71]. This explains that, as observed in Figure 5.6 and Figure 5.8, IRE and stimulation thresholds show both a linear relationship with pulse length in a log-log plot. The slopes of these plots are related to the membrane charging process, which, for a given pulse length, determines the electric field magnitude necessary to induce a TMV above the threshold. Therefore, one would expect both phenomena to show the same dependence on pulse length, but with higher electric field magnitudes in the case of IRE. However, the slopes described by our results and by the IRE experimental results are significantly different. What follows is an attempt to justify such difference.

The membrane charging process depends not only on membrane's passive properties (e.g conductance and capacitance), but also on the geometry of the cell and the electric current paths [208, 222–224]. A study on how several parameters affect the time constant when a fiber is exposed to the electric field created by a point electrode can be found in [208]. In a scenario like that presented in Figure 5.3 — a long fiber exposed to the electric field created by two parallel needle electrodes—, the measured time constant will depend on the geometry of the fiber, the membrane's passive properties, the electrode configuration, as well as the geometry of these electrodes. In these situations, in which a nerve fiber is exposed to a non homogeneous electric field, the membrane charging is driven by the second spatial derivative. Therefore, besides the axon's characteristics, the charging time will depend on the electrode configuration and will differ among different situations, such as, two parallel electrodes, two collinear electrodes or a single electrode and a distant grounding pad.

In the case of a nerve termination exposed to a homogeneous electric field (Figure 5.6 and Figure 5.8), the effects of the geometry and the spatial configuration of the electrodes do not exist. In this situation the charging time is determined by the membrane's passive properties and the cell geometry. And, according to our results, in this scenario the IRE thresholds and the stimulation thresholds show a significantly different dependence on the pulse length in this case. Therefore, assuming similar passive properties, it can be inferred that the different behavior may be caused by the geometry of the cells. This will be further discussed in the next section.

**Table 5.4:** Dielectric properties of the model: electrical conductivity, $\sigma$, and relative permittivity, $\epsilon_r$. The modeled thickness of the cell mebrane was 5 nm.

| | | |
|---|---|---|
| Extracellular medium | $\sigma$ | 1.5 (S/m) |
| | $\epsilon_r$ | 80 |
| Cell membrane | $\sigma$ | $2.5 \cdot 10^{-7}$ (S/m) |
| | $\epsilon_r$ | 5 |
| Intracellular medium | $\sigma$ | 0.5 (S/m) |
| | $\epsilon_r$ | 80 |

### 5.4.2 Cell geometry and membrane charging times

In order to study to what extent the geometry of the cells could explain the different threshold evolution with pulse length, we performed a brief study in which we compare the TMV induced by an external electric field in spherical cells and ellipsoidal cells. The spherical cells would represent the cells that were subjected to bursts in [203]. The ellipsoidal cells would account for a simplistic representation of the nerve terminations.

We computed in COMSOL the maximum TMV respect to the resting voltage induced by an external electric field, $\Delta$TMV, for three different cell geometries. The cell membrane was modeled as described in section 3.2 (Eq. ref3.4). The cell volume and the dielectric properties were equal in the three assayed cell geometries (see Table 5.4). We considered a sphere with a radius of 5 $\mu$m and two ellipsoids, having two equal semi-axes and a longer semi-axis with relationships of $R_2 = 20R_1$ and $R_2 = 5R_1$ between the length of these semi-axes and the length of longest one. In order to maintain the same volume in the three geometries, the lengths of the semi-axes were: 2.9 $\mu$m and 14.6 $\mu$m in the ellipsoid with $R_2 = 5R_1$ and 1.8 $\mu$m and 36.8 $\mu$m in the ellipsoid with $R_2 = 20R_1$. The longest semi-axis was aligned with the direction of the electric field. Therefore this situation would resemble the geometry of the nerve termination model in this study.

The time course of the maximum $\Delta$TMV induced by a relatively long pulse of 100 $\mu$s in the three cell geometries is displayed in Figure 5.9. Although the sphere reaches the steady state faster, the ellipsoids reach significantly higher $\Delta$TMV values. The ellipsoid with the largest ratio between semi-axes ($R_2 = 20R_1$) reaches the highest $\Delta$TMV, nevertheless, it also has the longest charging time. Cooper discussed this same effect for cylinders using a cable model and comparing different lengths [224]. When bursts of bipolar pulses are applied (Figure 5.10), due to this difference in the charging and discharging times, if short

pulses such as the ones considered in our study are applied, the difference in the maximum ΔTMV induced at the sphere and at the most elongated ellipsoid is reduced, down to sign inversion. Indeed, below a certain pulse length, the induced ΔTMV is larger in the sphere than in the ellipsoid.

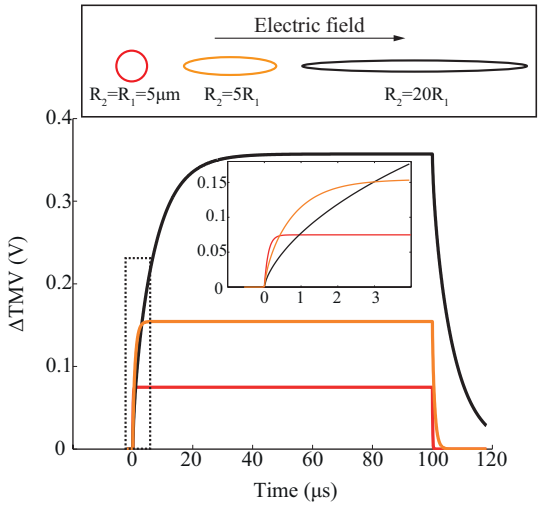


**Figure 5.9:** Simulated time evolution of the maximum ΔTMV induced in a spherical cell and in two ellipsoidal cells when these are subjected to an electric field pulse of 100 V/cm and 100 $\mu$s. The two ellipsoidal cells have two equal semi-axes and the other semi-axis has a length 20 times and 5 times the length of those axes respectively ($R_2 = 20R_1$ and $R_2 = 5R_1$). The volume and the dielectric properties were the same in the three geometries (See Table 5.4).

It has been suggested that the difference in membrane charging times can be explained as being the consequence of the fact that there are two separate mechanisms by which an external electric field induces a TMV. First, the current that crosses the membrane creates an ohmic voltage drop. Second, a difference in the external and internal electric field induces a TMV. According to Rall [88], in short cylinders the difference in electric field strengths between inside and outside the cell is the dominant process. In this case, most of the current flows alongside the surface of the cell and very few current flows across the membrane. Therefore, the steady state is reached through a redistribution of charges at the surface of the cell, which is a faster process than the ohmic potential. On the other hand, as the cylinder length increases, a larger amount of current must flow across the membrane to reach the steady state, making the charging time longer.

Based on the aforementioned, additional COMSOL simulations were

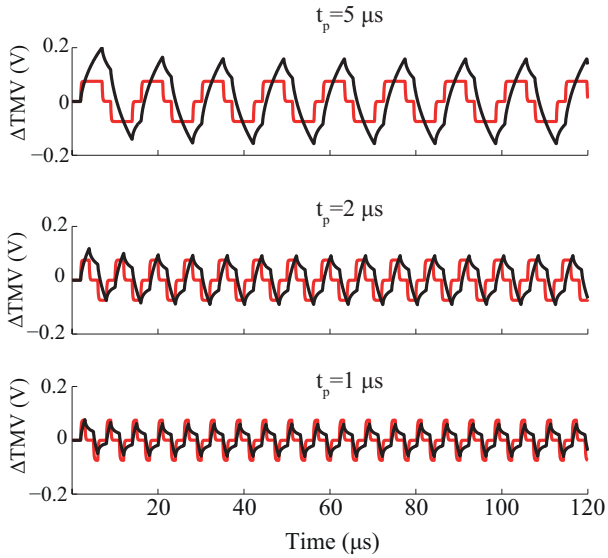


**Figure 5.10:** Simulated maximum ΔTMV in a spherical cell and in an ellipsoidal cell with $R_2 = 20R_1$ when a burst of bipolar pulses with a delay of 2 $\mu$s and an amplitude 100 V/cm is applied, for different pulse lengths.

performed aimed to reproduce the behavior observed in Figure 5.6. We assumed that the spherical cells (radius = 5 $\mu$m) were the cells to be electroporated and assigned to them an IRE ΔTMV threshold of 1 V. We also assumed that the ellipsoidal cells ($R_2 = 20R_1$) were the excitable cells and assigned to them a stimulation threshold of 50 mV. Then, using the same waveforms as in Figure 5.5 and Figure 5.6 (100 $\mu$s energized time and 2 $\mu$s inter-pulse delay), we calculated the electric field magnitude necessary for each pulse length in order to reach a peak ΔTMV equal to the thresholds defined above. To do so, we simulated the induced ΔTMV when the cell is exposed to an arbitrary 100 V/cm electric field for each geometry and pulse length. Finally, these results were used to scale the electric field magnitude in order to reach the desired peak ΔTMV in all cases. Figure 5.11 displays the obtained results, which show a similar trend to the results in Figure 5.6 and Figure 5.8. The sphere shows a flat dependence with the pulse length up to the shortest lengths due to its small charging time (≈0.2 $\mu$s). The ellipsoid on the other hand, has a longer charging time and as a consequence it shows a linear dependence in a log-log plot that starts at about 10 $\mu$s of pulse length.

From this brief study we can conclude that cells with elongated shapes, such the neurons that form the nerve fibers, have significantly longer

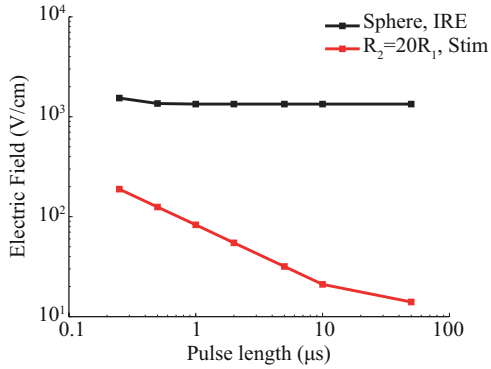


**Figure 5.11:** Hypothetical electric field magnitude that, when delivering bursts of bipolar pulses, would be necessary to induce IRE in a spherical cell (black line) and that would initiate an action potential in an elongated ellipsoid (red line). An arbitrary ΔTMV of 1 V was used as IRE threshold, and 50 mV were used as stimulation threshold. For different pulse lengths, the electric field magnitude necessary to reach a peak ΔTMV equal to the defined thresholds was calculated. The volumes and dielectric properties were the same in both geometries and the same as in Figure 5.9

charging times than those with a lower eccentricity. As a consequence, reducing the pulse length has a stronger impact on the peak membrane voltage induced by an external alternating electric field in elongated cells than in small roundish cells. Therefore we propose that the difference in the dependence that the IRE thresholds and the stimulation thresholds show with the pulse length is closely related to the geometry of the involved cells.

## 5.5 Conclusions

Through a numerical study, we have shown that delivery of bursts of bipolar pulses instead of the conventional monopolar pulses, allows producing ablations by means of IRE while reducing or avoiding nerve fiber or nerve terminal stimulation. Our models indicate that this is possible because, as the pulse length of the bipolar pulses is reduced from 100 $\mu$s to 1 $\mu$s, the stimulation thresholds raise threefold faster than the irreversible electroporation thresholds. This suggests that, for treating the same volume of tissue, it is possible to reduce the amount of recruited nerve fibers by reducing the length of the bipolar pulses.

We propose that the different dependence of the thresholds on the pulse length is due to the fact that transmembrane charging for nerve

fibers is much slower than that of cells treated by electroporation because of their geometrical differences. Cells with elongated shapes, such the neurons that form the nerve fibers, have significantly longer charging times than those with a lower eccentricity. As a consequence, reducing the pulse length has a stronger impact on the peak TMV induced by an external alternating electric field in elongated cells than in small roundish cells.

Although this study was focused on IRE based treatments, the results might be also valid for other electroporation based treatments. This reinforces the idea that working towards the use of bursts of bipolar pulses is a valid effort in order to improve electroporation based treatments in medicine.

The modeling framework employed in the present study, if complemented with thermal modeling and further experimental in vivo data on IRE thresholds for the bursts of bipolar pulses, could be used to optimize the pulsing protocols for safely performing IRE ablation with minimal neuromuscular stimulation.

## 5.6 Appendix

### Equations describing the ionic currents

The equations describing the ionic currents at the axon's membrane were taken from [206]. The currents in this model are adjusted to represent the excitation of a mammalian motor neuron at 36°C and consist of 3 types of ion channels and a leakage current. The total ionic current at each node is calculated as the sum of 4 different currents:

$$I_i = I_{Naf} + I_{Nap} + I_{Ks} + I_L \tag{5.4}$$

Fast sodium current

$$I_{Naf} = g_{Naf} m^3 h (V_m - E_{Na}) \tag{5.5}$$

$$\frac{dm}{dt} = \alpha_m (1 - m) - \beta_m m \tag{5.6}$$

$$\alpha_m = 6.57 \cdot \frac{V_m + 20.4}{1 - exp\,[-(Vm + 20.4)/10.3]} \tag{5.7}$$

$$\alpha_m = 0.304 \cdot \frac{-(V_m + 25.7)}{1 - exp\,[(Vm + 25.7)/9.16]} \tag{5.8}$$

$$\frac{dh}{dt} = \alpha_h(1-h) - \beta_h h \tag{5.9}$$

$$\alpha_h = 0.34 \cdot \frac{-(V_m + 114)}{1 - exp\,[(Vm + 114)/11]} \tag{5.10}$$

$$\alpha_m = 12.6 \cdot \frac{1)}{1 - exp\,[-(Vm + 31.8)/13.4]} \tag{5.11}$$

Persistent sodium current

$$I_{Nap} = g_{Nap} p^3 (V_m - E_{Na}) \tag{5.12}$$

$$\frac{dp}{dt} = \alpha_p(1-p) - \beta_p p \tag{5.13}$$

$$\alpha_p = 0.0353 \cdot \frac{V_m + 27}{1 - exp\,[-(Vm + 27)/10.2]} \tag{5.14}$$

$$\alpha_p = 0.000883 \cdot \frac{-(V_m + 34)}{1 - exp\,[(Vm + 34)/10]} \tag{5.15}$$

Slow potassium current

$$I_{Ks} = g_{Ks} s (V_m - E_K) \tag{5.16}$$

$$\frac{ds}{dt} = \alpha_s(1-s) - \beta_s s \tag{5.17}$$

$$\alpha_s = 0.3 \cdot \frac{1}{1 - exp\,[-(Vm + 53)/5]} \tag{5.18}$$

$$\alpha_p = 0.03 \cdot \frac{1}{1 - exp\,[-(Vm + 90)]} \tag{5.19}$$

Leakage current

$$I_L = g_L (V_m - E_L) \tag{5.20}$$

Values of the parameters used to model the ionic currents: $g_{Naf} = 3\ S/cm^2$, $g_{Nap} = 0.01\ S/cm^2$, $g_{Ks} = 0.08\ S/cm^2$, $g_L = 0.007\ S/cm^2$, $E_{Na} = 50\ mV$, $E_K = -90\ mV$, $E_L = -90\ mV$.

Chapter 6

# Differences in the dynamics and mechanisms of cell death between conventional IRE and H-FIRE treatments

**Abstract** — In the previous chapter we investigated the rationale behind the use of bursts of short bipolar pulses (i.e. H-FIRE) in IRE treatments. The use of a waveform different from the typically used monopolar pulses raises the question of whether the cell death mechanisms and dynamics remain the same. The aim of this chapter is to address this and investigate potential differences between IRE treatments with monopolar pulses and H-FIRE bursts. To do so, human pancreatic adenocarcionoma cells were treated with a conventional IRE protocol and various H-FIRE schemes with the same energized time. Cell viability, membrane integrity and Caspase 3/7 activity were assessed at different times after the treatments. In both treatment protocols we identified two different death dynamics (immediate and delayed) and we quantified the electric field ranges that lead to each of them. While in a conventional IRE protocol with monopolar pulses the electric field range leading to a delayed cell death is very narrow (100 V/cm), in H-FIRE this range is wider (up to 700 V/cm) and can be increased by reducing the pulse length. This delayed cell death takes place mostly between 4 and 8 hours. Unlike cells treated with a conventional IRE protocol, cells treated with H-FIRE displayed Caspase 3/7 expression. Thus, suggesting a difference between the delayed cell death mechanisms of the two treatment protocols.

Part of the contents of this chapter is adapted from:

B. Mercadal, N. B. White, K. N. Aycock, Q. Castellví, R. V. Davalos. and A. Ivorra "Immediate and delayed cell death after conventional IRE and H-FIRE treatments" [Under review]

## 6.1 Introduction

In the previous chapter, we showed that although the electric fields required to kill cells with H-FIRE are significantly larger than in conventional IRE protocols [202, 203], the excitation thresholds of peripheral nerves increase to a much larger extent when comparing conventional IRE monopolar pulses to H-FIRE waveforms. In fact, H-FIRE has been successfully applied to treat solid tumors with minimal muscle contractions [103–107].

The use of a different waveform in H-FIRE raises the question of whether the cell death mechanisms remain the same as in conventional IRE treatments. Currently very little is known regarding the cell death dynamics and mechanisms of H-FIRE. The lengths of the pulses that made up H-FIRE bursts have been relatively unexplored [225] and the cell death dynamics after the delivery of bipolar pulses are largely unknown. To the best of our knowledge cell death dynamics in H-FIRE have only been studied to some extent by Sano et al. [202] and it was found the existence of an immediate and a delayed cell death in cells treated with H-FIRE. The aim of the study presented in this chapter is to further investigate these two dynamics in H-FIRE as well as in conventional IRE protocols by quantifying the ranges of electric fields that lead to each form of death. In addition, we study if the mechanisms of delayed cell death are the same in H-FIRE and in conventional IRE with monopolar pulses.

## 6.2 Materials and methods

3D cell cultures have been previously used to study the outcome of IRE treatments in different cell lines [226–228]. With this model it is possible to accurately define the boundary between treated and untreated cells (live or dead) when used in combination with a live/dead staining method. Then, the profile of the treated region can be correlated with the electric field distribution obtained with a numerical model in order to determine the threshold electric fields. Thus, IRE thresholds can be measured with a relatively low number of experiments using this methodology. In the present study, 3D cell cultures were treated with different protocols and the treatment outcomes were measured at two time points (3 and 24 hours). This allowed us identifying the regions of immediate and delayed cell death after the treatments and quantifying the electric fields that lead to each of them.

Then, in order to have a better insight in the dynamics of the delayed

cell death, cells were treated with a uniform electric field. This series of experiments were done using cell suspensions. First, the electric field thresholds for cell death were measured. Then, these electric fields were delivered to the cells and membrane integrity as well as Caspase 3/7 activity were assessed at different times after the treatments.

### 6.2.1 Cell culture

BxPC-3 cells, a human pancreatic adenocarcinoma cell line, were grown in RPMI-1640 (ATCC modification) medium (Gibco, Dublin, Ireland) supplemented with 10% fetal bovine serum (Sigma-Aldrich, Sant Louis, MO, USA) and 1% penicillin/streptomycin (Invitrogen, Carlsbad, CA, USA). Cells were incubated at 37°C in a humidified environment containing 5% $CO_2$.

### 6.2.2 Collagen scaffold fabrication

Collagen I hydrogel-based scaffolds were fabricated following the same procedure as in [229]. Briefly, concentrated collagen stock solutions were created using rat tail collagen type I. 10% of the total volume of 10× culture medium and 2% of the total volume of 1N NaOH were added to the collagen solution and mixed thoroughly with a spatula until homogeneous. 1N NaOH was added until the pH was adjusted to 7-7.4. Cells in suspension were mixed into the collagen solution for a final concentration of $10^6$ cells/ml. Then, the collagen was injected into custom made Polydimethylsiloxane (PDMS) disk shaped parts (10 mm diameter and 1 mm height) placed at the bottom of wells in a 24-well plate. The injected collagen was flattened with a PDMS mold and placed in the incubator for 20 minutes in order to produce polymerization. Finally, the molds were withdrawn, fresh medium was added to the wells and they were incubated overnight before performing the treatments.

### 6.2.3 Electric field generation

In this study, cells were exposed to a conventional IRE protocol (100 $\mu$s, monopolar pulses) and H-FIRE protocols with different pulse lengths and inter-pulse delays (See Figure 6.1). All H-FIRE protocols had a total energized time within a burst of 100 $\mu$s. Along this chapter the H-FIRE protocols will be referred to as positive pulse length – inter-pulse delay – negative pulse length. All treatment protocols consisted of 80 pulses (or bursts in the case of H-FIRE) delivered at a frequency

of 1 Hz. 100 $\mu$s monopolar pulses were generated by a BTX ECM 830 pulse generator (Harvard Apparatus, Holliston, MA). H-FIRE bursts were generated by a custom-built pulse generation system.

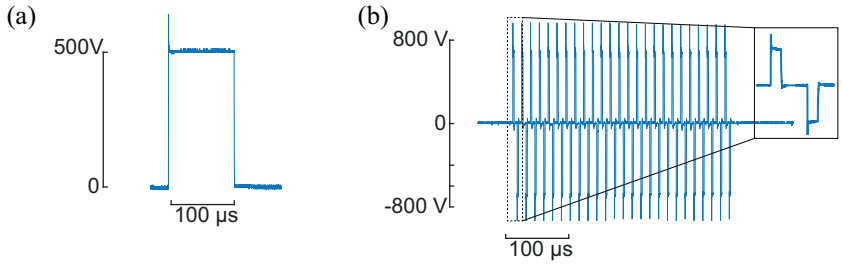


**Figure 6.1:** Oscilloscope traces registered during (a) a conventional IRE treatment and (b) a 2-5-2 H-FIRE treatment.

### 6.2.4 Determination of the lesion areas and electric field thresholds in 3D cell cultures

Prior to the electroporation treatments, the culture medium was aspirated from the wells. The electric fields were delivered using blunt tip stainless steel needles with an outer diameter of 0.9 mm. The two electrodes were placed using a custom-made plastic structure which ensured a 4 mm separation between the electrode centers (See Figure 6.2). After the treatment, fresh medium was added to the wells and they were returned to the incubator. 3 and 24 hours after the treatments, the medium was aspirated and a PBS solution containing 20 $\mu$M Propidium Iodide (PI, Invitrogen) and 2 $\mu$M Calcein AM (Invitrogen) was added to the wells. Cells were then kept at room temperature for 30 minutes protected from light. After washing the cells with PBS (Gibco), images of each well were taken using an inverted DMI 6000B microscope (Leica Microsystems, Wetzlar, Germany) with a 5$\times$ objective. In normal conditions, PI is not permeant to cells, however, it can diffuse through the compromised membranes of dead cells. Once inside the cell, this dye binds to DNA and its fluorescence is enhanced 20-30 fold. Calcein AM in contrast is a cell permeant dye that emits green fluorescence when penetrates into live cells. This allowed visualizing the regions in the collagen scaffold where cells have died as a consequence of the treatment and the region where the cells have survived under a fluorescence microscope.

The images obtained were used to measure the lesion area and calculate the electric field thresholds for cell death. This was done following

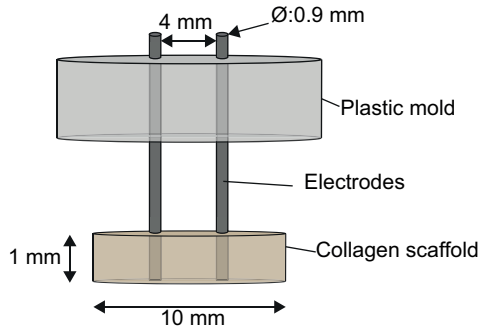


**Figure 6.2:** Schematic of the set-up used to treat 3D cell cultures.

the same procedure as in [228]. Briefly, the green channel (Calcein AM) was used to limit the lesion area using a custom developed MATLAB code. Once the lesion limits were extracted, the area was calculated by a built-in MATLAB function. In those cases in which the algorithm was unable to find the lesion limits due to insufficient fluorescence intensity or image artifacts such as bubbles, the area was manually measured using Image J [185].

The electric field thresholds were calculated by fitting the extracted areas (from the images) to the results of a numerical model. First, the electric field distribution was computed with a FEM model using COMSOL (See Figure 6.3). Then, the areas enclosed by the isolines at different electric field values were extracted from the obtained electric field distribution. These values were used to determine a relationship between the electric field and the area by a polynomial adjustment with the least squares method. Finally, the function obtained by the adjustment was used to convert the lesion areas to electric field threshold values. In order to test the robustness of the whole process, two different voltages were delivered for each treatment protocol and the obtained threshold values were compared statistically.

### 6.2.5 Statistical analysis

A Mann-Whitney-Wilcoxon test was used to analyze the differences between lesion sizes and electric field thresholds. The statistical tests were run in the R-3.5.3 software package [186].

### 6.2.6 Preparation and treatment of cells in suspension

At 70-90% confluence, cells were detached using a solution consisting of PBS and 0.5 mM EDTA (Panreac, Barcelona, Spain). This

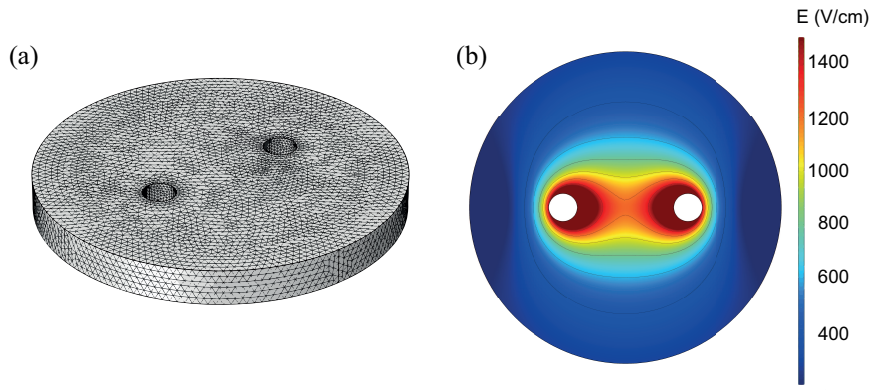


**Figure 6.3:** (a) FEM mesh used to simulate the electric field distribution in the 3D cell culture. The collagen scaffold was modeled as a disk with a diameter of 10 mm and a thickness of 1 mm. The electrodes were modeled as 0.9 mm diameter cylinders. (b) Electric field distribution in the 3D cell culture when 500 V are applied between the electrodes.

detachment method was used to facilitate the quick adhesion of the cells after the treatments. Once detached, the cell suspension was centrifuged twice and re-suspended into growth medium at a concentration of $5 \cdot 10^6$ cells/ml. 100 $\mu$L of the suspension was transferred to a 1 mm gap electroporation cuvette (Thermofisher, Waltham, MA, USA) and the desired pulsing protocol was delivered. Immediately after the treatment, cells were diluted tenfold in growth medium and seeded into 6 well plates. Cells were kept in the incubator until further measurements.

### 6.2.7 Electric field thresholds in suspension cells

24 hours after the treatment cell viability was assessed through a Trypan Blue exclusion assay. Cells were trypsinized and the cell suspension was mixed with a 0.4% Trypan Blue solution (Gibco). Live cells were counted with a Neubauer chamber under a light microscope and the viability was calculated as the number of viable cells divided by the number of viable cells in the Sham groups. The threshold was defined as the lowest electric field that resulted in mean viability levels lower than 10%.

### 6.2.8 Membrane permeability to Yo-Pro-1 and Propidium Iodide

In these experiments, treated cells were diluted tenfold in growth medium and transferred to 1.5 ml Eppendorf tubes and kept in the

incubator. After different time points between 15 minutes to 3 hours, PI and Yo-Pro-1 (Sigma Aldrich) were added to a final concentration of 15 $\mu$M and 0.5 $\mu$M respectively. Cells were kept on ice for 20 minutes before analysis.

Fluorescence of the cells was measured using a LSR II flow cytometer (BD Biosciences, San Jose, CA). Both PI and Yo-pro-1 were excited by a 488 nm laser and their emissions were collected by 695/40 and 530/40 Band pass filters respectively. The results were analyzed using the FACSDiVa v6.1 software (BD Biosciences). Gates were applied on forward and side scatter in order to exclude cell fragments and debris. A total of 10000 counts inside the gating region were acquired and the measured fluorescence values were adjusted with a compensation factor in order to remove the artifacts due to spectral overlap between the dyes. Finally, cells were classified as either unstained, Yo-pro-1 positive, PI positive or double stained. This classification was done by plotting the fluorescence intensity in the two wavelengths of interest and defining four regions in the plot. These regions as well as the compensation factors were adjusted by using positive and negative control samples. Positive controls of stained cells were generated by exposing them to ice cold 70% ethanol for 30 minutes before staining with the desired dye.

### 6.2.9 Expression of Caspase 3/7

At 4, 6 and 8 hours after the treatment, cells were detached using PBS with 0.5 mM EDTA and double stained to study the expression of Caspase 3/7 and cell membrane integrity. Caspase 3/7 expression was assessed using CellEvent$^{TM}$ Caspase-3/7 (Invitrogen) and membrane integrity was assessed using DAPI (Panreac). Following the manufacturer's instructions, 1 drop of CellEvent per ml of medium was added and cells were incubated at 37°C for 30 minutes. Then, DAPI was added to a final concentration of 1 $\mu$g/ml and cells were incubated at room temperature for 10 minutes before their analysis.

Cells were analyzed by flow cytometry following a similar procedure as explained above. CellEvent was excited by a 488 nm laser and the emission was collected by a 530/40 Band pass filter. DAPI was excited by a 407 nm laser and the emission was collected by a 460/50 Band pass filter. No spectral overlap was detected between the two dyes. Positive control samples for Caspase 3/7 were generated by pharmacologically inducing apoptosis to untreated cells. This was done by treating them with 1 $\mu$M of Staurosporine (Panreac) for vari-

ous hours. DAPI positive controls were prepared with ethanol treated cells as well as with electroporated cells. Positive and negative control samples were used to define regions in order to classify cells as: unstained, Caspase expressing or DAPI positive.

## 6.3 Results

### 6.3.1 3 hours and 24 hours lesions in 3D cell cultures

An increase in the lesion size can be observed in the treated 3D cell cultures between 3 and 24 hours (Figure 6.4). Statistically significant differences ($p<0.05$) were found between the areas obtained at 3 and 24 hours in all the treatment protocols used in this study (Figure 6.5). The average fraction of the lesion that occurs after 3 hours is larger in the H-FIRE protocols than in the IRE protocol with monopolar pulses (Figure 6.6(a)). In addition, this fraction increases as the pulse length of the H-FIRE protocols is reduced. Ater treating cells with conventional, IRE 80% of the total lesion occurs in less than 3 hours. In contrast, in the H-FIRE protocols with 1 $\mu$s pulse length this fraction is reduced to 35%. On the other hand, the results suggest that the inter-pulse delay does not have a strong effect on this proportion.

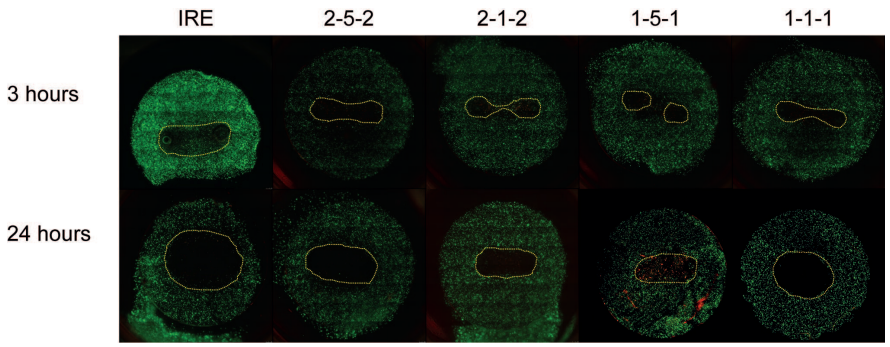


**Figure 6.4:** Examples of lesions obtained at 3 and 24 hours after the treatments. A clear increase in the lesion size between 3 and 24 hours can be observed in all treatment protocols.

In every individual sample, the threshold was extracted from the measured lesion area. No statistical differences were found between the thresholds obtained using different voltages for the same pulsing protocol and time point ($p>0.05$, data not reported here). The average thresholds obtained at 3 and 24 hours are presented in Figure 6.6(b)

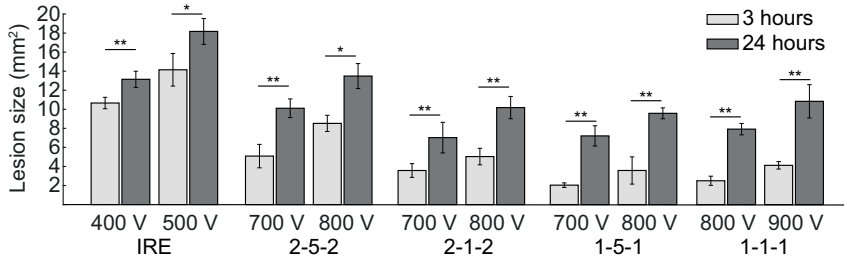


**Figure 6.5:** Lesion areas obtained at 3 and 24 hours after the treatment by using different treatment protocols. The results are presented as mean ± standard deviation (n≥5 in all cases). (* p<0.05 , ** p<0.01).

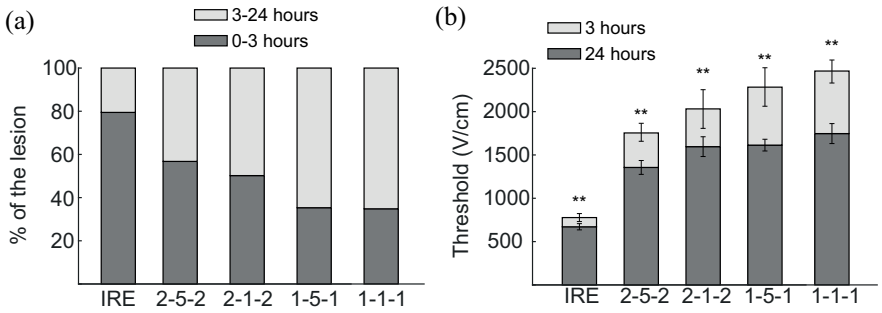


**Figure 6.6:** (a) Average proportion of the lesion produced before and after 3 hours (b) Thresholds obtained at 3 and 24 hours for each treatment protocol. The results are presented as mean ± standard deviation (n≥10 in all cases). (* p<0.05, ** p<0.01).

and the values can be found in Table 6.1. Statistical differences were found between 3 and 24 hours in all protocols. Therefore, there is a range of electric fields in which cells die shortly after the treatment (less than 3 hours) and a range of lower electric fields in which the cells die in a slower fashion (between 3 and 24 hours). This range of electric fields that leads to a delayed cell death is larger in the H-FIRE protocols than in the IRE protocol and it increases by reducing the length of the pulses. In contrast, the inter-pulse delay seems to have a minor effect on this range.

### 6.3.2 Cell death dynamics in cell suspensions

Cells in suspension were treated with the conventional IRE protocol and the 2-5-2 H-FIRE scheme. In first place, the 24 hours thresholds for these protocols were measured. This was done by measuring the cell viability percentage 24 hours after the treatment for different

**Table 6.1:** Thresholds obtained in 3D cell cultures presented as mean ± standard deviation and expressed in V/cm.

| Protocol | 3 hours | 24 hours |
|---|---|---|
| IRE | 777±46 | 671±36 |
| 2-5-2 | 1754±104 | 1356±80 |
| 2-1-2 | 2032±223 | 1596±114 |
| 1-5-1 | 2283 ±222 | 1614±68 |
| 1-1-1 | 2468±133 | 1746±115 |

electric field magnitudes (Figure 6.7). The thresholds were extracted as the minimum electric field that yields a mean viability lower than 10%. A threshold of 1100 V/cm was obtained for the IRE protocol and a threshold of 3800 V/cm was obtained for the 2-5-2 scheme. All the following experiments were performed by applying the measured electric field thresholds.

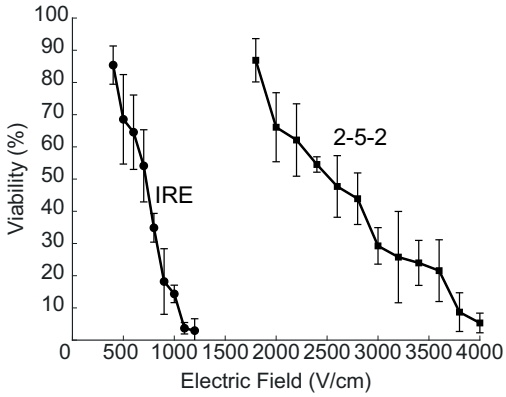


**Figure 6.7:** Cell viability as a function of the electric field magnitude measured 24 hours after cells in suspensions are treated with conventional IRE (circles) and the 2-5-2 H-FIRE scheme (squares). Results are presented as mean ± standard deviation (n≥3).

We assessed membrane permeability to PI and Yo-Pro-1 at different time points after the treatments. The results displayed in Figure 6.8 show that, in both treatments, after 15 minutes there is a large percentage of cells exhibiting permeability to Yo-Pro-1 but not to PI, especially in the H-FIRE treated samples. The percentage of PI permeable cells is larger in the IRE samples than in the H-FIRE ones. After both treatments, the percentage of PI permeable cells remains quite stable during all the measured time points, especially after 1 hour. In contrast, the percentage of Yo-Pro-1 permeable cells signifi-

cantly decreases during the first hour and then remains stable in both cases. In cells treated with conventional IRE pulses this percentages is very low (<4%) while in the H-FIRE treated samples it is around 15%.

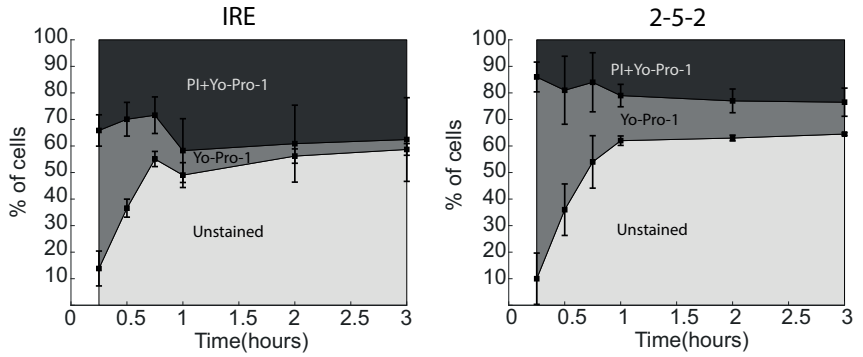


**Figure 6.8:** Evolution of membrane permeability to PI and Yo-Pro-1 after treating the cells with IRE pulses of 1100 V/cm and 2-5-2 bursts with 3800 V/cm amplitude. Squares show the mean percentage of cells permeable to PI and Yo-Pro-1 at different times after the treatment (n≥4 for each time point). The error bars show the standard deviation.

## 6.4 Dicussion

Our results show that IRE with monopolar pulses and H-FIRE treatments can both lead to either an immediate (i.e. necrosis) or a delayed cell death depending on the electric field magnitude applied. However, the range of electric fields that lead to a delayed cell death is very narrow in the conventional IRE protocol, while in H-FIRE protocols this range is wider and can be increased by reducing the pulse length. A direct consequence of this, as showed by our results, is that with a typical electroporation set-up (two needle electrodes) a large portion of the ablated volume can be accomplished through a non-necrotic pathway with H-FIRE. In addition, the fact that necrotic cell death can be largely avoided within a wide range of electric fields implies that H-FIRE may offer a greater control on the cell death mechanisms taking place after a treatment. In other words, controlling the electric field exposure may allow selecting between a purely necrotic ablation and an almost purely non-necrotic ablation.

In both treatments, the evolution of PI permeability in Figure 6.8 shows that, even with electric fields around the threshold, there is a fraction of cells whose membrane integrity is not recovered. Thus, a

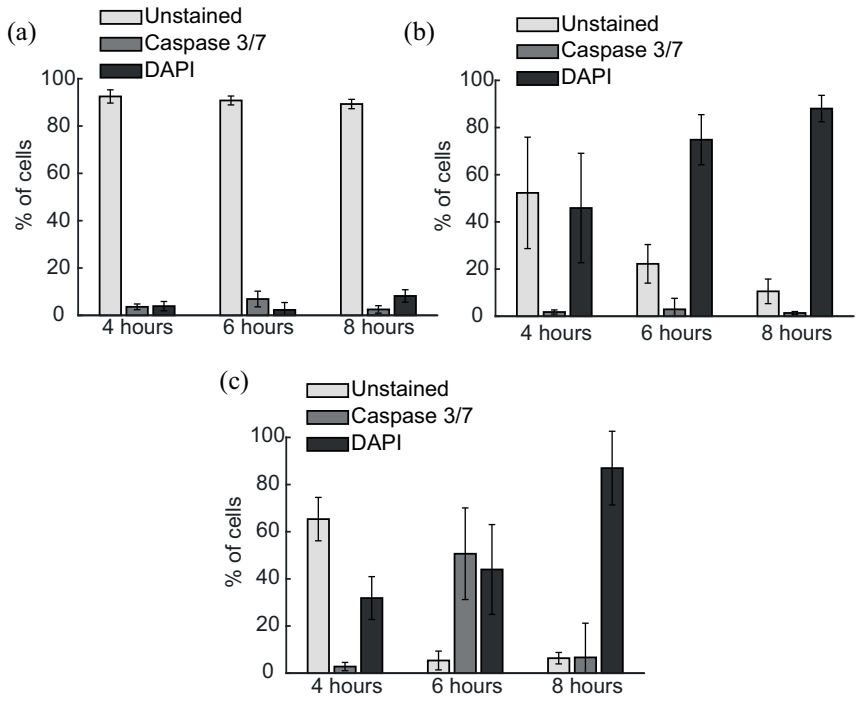


**Figure 6.9:** Assessment of Caspase 3/7 activity and membrane integrity at different times after treating the cells with IRE pulses of 1100 V/cm and 2-5-2 bursts with 3800 V/cm of amplitude. The values in the bar plots are presented as mean ± standard deviation (n≥7 in all treatment groups and time points). (a) Sham. (b) IRE treated cells.(c)Cells treated with a 2-5-2 H-FIRE scheme.

fraction of cells die through necrosis regardless of the electric field. The fraction of DAPI positive cells at 4 hours (Figure 6.9) is very similar to the PI positive cells between 1-3 hours. Therefore, essentially no cells died between 1-4 hours and all the remaining viable cells died between 4 and 8 hours. This time evolution is consistent with other experiments in IRE using 100 $\mu$s pulses [230] or nanosecond pulses [231] and shows the existence of two clearly identifiable cell death dynamics.

Yo-Pro-1 uptake can be either an early indicator of apoptosis [232] or an indicator of membrane permeability [233]. Yo-Pro-1 is smaller than PI which makes it a more sensitive marker of membrane permeability [130]. In our experiments we observed a large fraction of Yo-Pro-1 positive cells briefly after the treatments that significantly reduced within 1 hour. This may be attributed to a recovery of the membrane integrity within this time lapse. After 1 hour there is a small fraction of cells that remain permeable to Yo-pro-1 which may

be either an indicator of apoptosis or an indicator that these cells are not able to fully recover their membrane integrity. Our results show that the mechanisms of delayed cell death are different between a typical IRE treatment and an H-FIRE scheme. While in H-FIRE this death is preceded by the expression of Caspase 3/7, in conventional IRE, cells die through a pathway independent of Caspase 3/7. The activity of these proteins is widely used to classify cell death as it is one of the main hallmarks of apoptosis. Therefore, our results are consistent with an apoptotic cell death in the case of H-FIRE but not in the case of IRE. However, further research needs to be done in order to properly classify the death mechanisms in both cases.

The exact death mechanisms of IRE are still under study. In the recent past it was believed that in conventional IRE treatments cell death was mostly necrotic in combination with some extent of apoptosis [234, 235]. In fact, several studies supported the idea that cell death after these treatments was in part apoptotic [236–240]. However, our understanding of the death mechanisms has quickly evolved in the recent years. Nowadays, several forms of programmed cell death have been identified besides apoptosis [241, 242]. Therefore the interpretation of the results in some of those studies would have been likely different in the present. In fact, more recent studies using conventional IRE treatment protocols point towards other forms of programmed cell death such as pyroptosis or necroptosis instead of apoptosis [243, 244]. These cell death modes are independent of the expression of Caspase 3/7, thus, our results are consistent with those studies.

In the case of H-FIRE, the cell death mechanisms after the treatment have been barely studied. Histological examination of tissues treated with H-FIRE found activation of Caspase 3 [103, 105] which is consistent with our results. However, another study showed evidences of Caspase 3/7 independent death modes such as pyroptosis and necroptosis [104] which would contradict our results. Nonetheless, it is important to note that we have only quantified Caspase expression for a specific electric field magnitude. Thus, we cannot rule out the possibility that these other death modes coexist within the range of electric fields that lead to a delayed cell death.

Unlike other waveforms, cell death mechanisms have been more deeply studied after the delivery of nanosecond pulses [245–249]. From the numerous studies using those pulses it can be extracted that the cell death pathways depend on multiple variables such as the cell line,

the pulse length, the electric field strength and the composition of the extracellular medium [250]. Thus, the results presented here regarding the death mechanisms need to be taken with caution as it is unclear how they can be extrapolated to other cell lines or pulse protocols.

## 6.5 Conclusions

We showed the existence of two clearly identifiable cell death dynamics in cells treated with conventional IRE and H-FIRE protocols. Cells treated with a conventional IRE protocol mostly die briefly after the treatment and only a narrow range of electric fields lead to a delayed cell death. In contrast, H-FIRE protocols lead to a delayed cell death within a wide range of electric fields. Thus, H-FIRE protocols can largely reduce the fraction of cells that die through necrosis compared to IRE treatments with 100 $\mu$s monopolar pulses. In addition, H-FIRE protocols may offer the possibility to select between a purely necrotic and an almost completely non-necrotic cell death with sufficient control on the electric field delivered.

Finally, in the present study we quantified for the first time the dynamics of the delayed cell death after treating cells with H-FIRE. In addition, our results suggest that the mechanisms of the delayed cell death may be different between conventional IRE and H-FIRE.

Chapter 7

# Innervation model for the study of the recruitment patterns in intramuscular electrical stimulation

**Abstract** — Compared to surface stimulation, intramuscular electrical stimulation has shown to be an advantageous strategy for finer control of muscle recruitment and minimizing fatigue. Understanding the recruitment processes and optimizing electrode placement are crucial in order to obtain the desired outcomes. For this purpose, numerical models can be of great help. Nevertheless, a suitable modeling scheme for intramuscular stimulation has not been developed yet. This chapter presents a muscle model created by using already existing models of motor unit pools and motor neurons and integrating them into a synthetic 3D muscle innervation model. The model allows the simulation of twitch forces in response to intramuscular electrical stimulation by monopolar electrodes. The main novelty of the model presented in this chapter lies in the integration of a motor unit pool in a realistic intramuscular nerve distribution, thus, providing an appropriate tool to study the recruitment patterns in intramuscular electrical stimulation. It qualitatively reproduces different experimental observations regarding muscle recruitment and supports some explanatory hypotheses for those observations. In addition, the results obtained with the model offer insights on the muscle response to stimulation at different locations and may serve as a guide to optimize electrode placement in order to maximize the benefits of intramuscular electrical stimulation.

Part of the contents of this chapter is adapted from:

B. Mercadal, J. M. Phillips, A. Eladly. and A. Ivorra "Innervation model for the study of the recruitment patterns in intramuscular electrical stimulation" [Under review]

## 7.1 Introduction

The main challenges in functional electrical stimulation derive from the different recruitment patterns between a voluntary and an electrically elicited contraction (see sections 2.3.6 and 2.3.7). The most promising approach to overcome these issues is interleaved stimulation [96]. Which consists on using multiple electrodes in order to activate subunits of the muscle and distribute spatially and temporally the force production within the muscle.

The effectiveness of interleaved stimulation in overcoming fatigue is greatly compromised by the amount of overlap in the muscular regions activated by the different electrodes. In comparison to surface and nerve electrodes, intramuscular electrodes offer the possibility of achieving regionalized muscle activation. By placing the intramuscular electrode near fine nerve branches supplying localized regions of the muscle, selectivity in muscle activation is increased and overlap between recruited regions is minimized. Thus, it is of great importance to estimate the spatial distribution of the recruited regions in intramuscular electrical stimulation in order to test and optimize stimulation strategies for effective interleaved stimulation. For this purpose, numerical models can be of great help. In fact, models of muscle force production and fatigue [251–255] as well as models of motor neuron responses to external electrical stimulation [86, 205, 206, 214] have been extensively studied. Several neuromuscular models have been developed aiming at a wide range of applications [256–259]. However, none of these models provides a suitable modeling scheme to study intramuscular stimulation. In order to model intramuscular stimulation it is crucial to account for the wide range of MU sizes, the spatial location of their motor neurons inside the muscle and their different responses to electrical stimulus. To the best of our knowledge none of the existing models in literature combines those three features.

This chapter presents a modeling framework to generate a synthetic muscle and study the motor unit recruitment patterns and twitch force generation in intramuscular electrical stimulation. This model was generated by using well established existing models of motor unit pools and motor neuron responses to electrical stimulus combined with the available knowledge regarding the spatial distribution of the motor neurons within the muscle.

## 7.2 Model

Here it is presented the modeling framework together with a synthetic muscle model we have generated to study the recruitment patterns in intramuscular electrical stimulation in a hypothetical, but plausible, case. The muscle model is intended to represent a spindle shaped unipennate muscle (see Figure 7.1) with its muscle fibers innervated by a single motor end-plate region located at approximately the center of the muscle. The model was entirely implemented in MATLAB, the routines used to generate the results presented here can be found online (https://github.com/bmercadal/Neuromuscular-Model). A scheme of the modeling process can be found in Figure 7.2. The

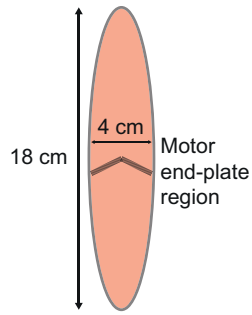


**Figure 7.1:** Geometry of the modeled muscle

first steps in the generation of the model consist in the creation of the intramuscular nerve distribution and a MU pool. Nerve distribution is created through the generation of a nerve tree that reproduces the intramuscular nerve branching that provides a neuronal supply to each muscle fiber. This nerve tree defines the paths through which the motor neurons will travel and the MU pool consists of a set of MUs having different properties such as size or force. This MU pool is then integrated in the nerve tree by creating a set of motor neurons that innervate the muscle fibers. Once the model is created, virtual monopolar electrodes can be placed anywhere in the model geometry and the muscle response to an electrical stimulus can be obtained. This is done by simulating the motor neuron response to the stimulus and adding the force contribution of all MUs that are activated by the stimulus. All these steps are described in detail in the following sections.

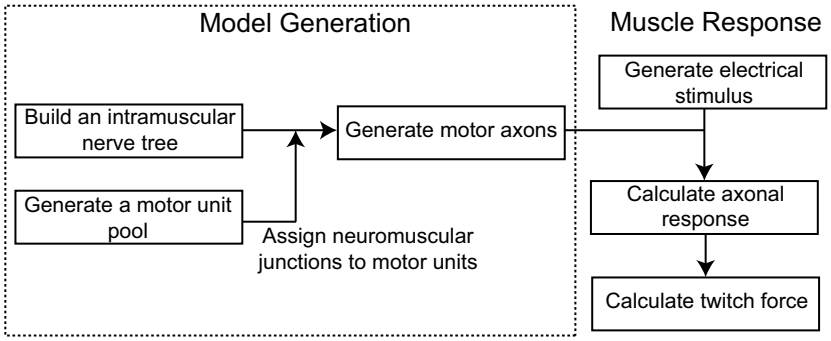


**Figure 7.2:** Modeling process used in this study

### 7.2.1 Intramuscular nerve tree

In general, muscles are innervated by one or more main nerves that split in several branches when they reach the muscle [260]. These branches are referred to as major branches and they are usually generated before entering the muscle. Once the major branches enter into the muscle, smaller branches arise from them giving raise to what is known as the minor branches. As these branches propagate inside the muscle, higher level branches arise from them and the nervous tree expands until it reaches the neuromuscular junctions (NMJ). The NMJs are the points at which the motor neurons connect with the muscle fibers through chemical synapses. These NMJs are usually localized into one or more small regions of the muscle known as the motor end-plate regions [261–264].

While major and minor branches have been traced for several muscles and various patterns have been identified regarding the numbers of branches [260, 265–267], the knowledge of the arborization patterns of higher level branches is very limited. This is mainly due to the difficulty in tracing those branches. In recent years axon terminals have been traced and complete reconstructions of muscle innervations have been achieved for small muscles [268, 269]. However, it is unknown if the patterns observed in such small muscles would apply to larger ones.

The locations of the motor end-plates have been extensively studied in several muscles [261, 262, 270]. In general, motor end-plate regions appear as narrow bands whose spatial distribution depends on the muscle shape and the muscle fibers orientations [262, 271]. In the simplest muscle morphologies the motor end-plate region consists on a single band with a v shape and approximately at the middle of the

muscle [263, 270, 272]. On the other hand, the motor end-plate regions in more complex muscle architectures are distributed in several bands across a large volume within the muscle [262, 264].

In the present study we aimed at creating a nerve tree with a simplistic structure in order to obtain results that can be interpreted in terms of the innervation patterns explained above. Thus, the results may be generalized to any muscle by making reference to easily identifiable anatomical landmarks such as the nerve entry, the major branches of the nerves and the motor end-plate regions.

The nerve tree was created aiming to replicate the nerve distribution of a simple unipennate muscle with its NMJS organized in a single v shaped band located at approximately the center of the muscle. The tree architecture was organized in four branch levels: the major branches, the minor branches, third order branches and a fourth level consisting in small twigs that join the third level branches with the NMJs.

The different levels of the tree were generated following procedures that had a certain level of randomness but at the same time a series of restrictions in order to generate a realistic tree. These restrictions aimed to accomplish two main features: first, that after each branching level the new branches are evenly distributed across the muscle cross section, thus maximizing the space occupied by them. Secondly, that the branches sprouting from the same major branch distribute inside a limited region of the muscle's cross section, allowing a slight overlap between the regions of the different major branches. The major branches were created arising from the same point of the nerve trunk and were expanded by randomly creating small segments within a specific range of directions. The directions of the branches were restricted in order to create a central branch and three lateral branches approximately evenly distributed. In addition the lateral branches were restricted so their radial distance to the center of the muscle was less than half the muscle radius. These branches were expanded until they reached half the distance between the nerve trunk and the motor end-plate region.

In order to create the minor branches, evenly spaced points occupying 80% of the muscle radius were created using a sunflower seed arrangement [273]. These points were placed at the plane corresponding to 2/3 of the distance between the nerve trunk and the motor end-plate region. Then the muscle cross section was divided in 4 compartments, one for each major branch, and the generated points were associated to

the major branches based on the compartment where they belonged. Then, random locations in the major branches were designated as the minor branches origin and associated to one of the generated points. To join the points with their designated branch locations, an attractive force depending on the square of the distance was modeled. The minor branch path was created by calculating the trajectory from the generated points to the major branches due to this attractive force. Finally, after all the points were joined to the major branches, the resulting minor branches were expanded until they reached 85% of the distance between the nerve trunk and the motor end-plate region.

The process to generate the third level branches was very similar to that used to generate the minor branches. Evenly spaced points were generated with a sunflower seed arrangement occupying a 95% of the muscle radius. These points were placed at the plane corresponding to a 95% of the distance between the nerve trunk and the motor end-plate region. Locations in the minor branches were assigned to each point to create the third level branch origins. These locations were randomly selected with the restriction that the radial distance between them and the associated point was less than 1/5 the muscle radius. Finally, the points were joined with the branch origins with a straight line. A similar process was used to create the fourth level branches. In this case the evenly spaced points were in fact the NMJ and therefore they were located at the motor end-plate region. Then the process to join these points with the third level branches was exactly the same as in the previous step.

### 7.2.2 Motor unit pool

A MU pool of 120 MUs was generated based on the model developed by Fuglevand et al. [253, 255]. This model assigns a twitch amplitude $P(i)$ to each MU, $i$, by the following exponential function:

$$P(i) = e^{[\ln(RP)(i-1)/(n-1)]} \tag{7.1}$$

where $RP$ is the range of twitch forces within the MUs in the pool (the strongest MU has a force $RP$ times the force of the weakest MU) and $n$ is the number of MUs in the pool. In our model a range of twitch forces, $RP$, of 100 was used which is approximately the range that has been reported by experimental studies [274]. These values of $P$ were normalized with respect to the total muscle force in order to obtain the contribution of each MU to the total muscle force. Then, the obtained values were multiplied by the total number of muscle

fibers to calculate the number of fibers that are innervated by each MU. This approach assumes that all muscle fibers contribute equally to the total muscle force (all muscle fibers are equal) which is not true since different types of muscle fibers exist. It has been shown that MU force depends not only on the number of fibers but also has a strong dependence on the total area of the fibers [90, 275]. However, although this simplification affects the calculation of the twitch forces, it does not have a strong effect on the recruitment patterns of the MUs. The limitations of this assumption will be further discussed in section 7.3.4.

### 7.2.3 Integration of the motor unit pool into the nerve tree

Once the MU pool was generated, those MUs were integrated into the nervous tree. The number of fibers innervated by each MU is equivalent to the number of NMJ in the tree and each NMJ has associated a path inside the tree. Thus, the whole paths described by the axons from the nerve trunk to the motor end-plate region could be traced by allocating the NMJs into the MUs.

In real muscles, the regions of innervated by the different MUs overlap and the muscle fibers of the MUs intermingle [276, 277]. However, although the muscle fibers associated to a single MU can occupy a large portion of the muscle cross section, they are usually localized in a specific region [278–281]. There are evidences that this so called compartmentalization of the MUs is related to the nerve tree architecture and the paths of the motor neurons inside the tree. In particular, several studies show that the regions innervated by MUs correspond to the same regions innervated by the major nerve branches [278, 282–285]. This compartmentalization pattern seems to hold true within different muscles and species and is consistent with the size of the regions innervated by single MUs. In fact, if compartmentalization existed about higher level branches the regions innervated by MUs would be smaller compared to what is observed experimentally. However, higher level branches are difficult to study, and although it seems unlikely that compartmentalization occurs at higher level branches it may be the case in some muscles (see for example the study by Hammond et al.[286]).

In our model, MU compartmentalization was imposed when the NMJs were assigned to MUs. NMJs were randomly assigned to MUs with the only restriction that all NMJs associated to a MU must belong to

the same major branch. This was done through an iterative process as follows: first, a matrix of weights, $w_{ij}$, is created being $i$ the MU index and $j$ the major branch index:

$$w_{ij} = \frac{n_{ij}}{\sum_j n_{ij}} \tag{7.2}$$

Where $n_{ij}$ is the number of muscle fibers of the MU $i$. Then, a MU is randomly assigned to each NMJ based on the weight. Every time that a NMJ is allocated into a MU $i$, the algorithm looks at the index of the major branch $j$, to which the NMJ belongs and turns to zero all the values $n_{ij}$ for $j$ different to the major branch index. Therefore at each step the weight matrix is updated. At the end of this process the twitch amplitude of each motor unit is calculated and compared with the twitch amplitude calculated from Eq. 7.1. If the average difference between them is above a 5% the process is repeated until a configuration that differs less than a 5% is found. Then, once the NMJ are allocated into the MUs, it is straightforward to trace the paths of each MU neuron by extracting them from the nerve tree.

Finally, the motor neuron radius along its path needs to be defined. The diameter of a motor neuron is related to the MU size and therefore on how extensively it branches [287–289]. In addition, the diameter decreases as the motor neuron moves distally into the muscle which seems to be related with the neuronal branching [268]. It has been observed that whenever the neuron branches, the diameters of the daughter branches are smaller than the diameter of the parent. In general the sum of the cross sections of the daughter branches equals or is slightly larger than the cross section of the parent branch([287].

In our model it was assumed that the total cross section is constant along the muscle and that the diameter at the neuron ends when it reaches the NMJs is the same in all cases and across all MUs. These two assumptions yield a direct relation between the diameter at the neuron ends and the diameter at any point:

$$D = \sqrt{N_d} \cdot D_{min} \tag{7.3}$$

where $N_d$ is the number of daughter NMJs that are connected to that point, and $D_{min}$ is the minimum neuronal diameter (diameter at the axon ends). The minimum diameter, $D_{min}$, was arbitrarily set to the plausible value of 1 $\mu$m [269].

### 7.2.4 Electrical stimulation and twitch force

The response of the motor neurons to external electrical stimulation was modeled as in section 5.2.2. Note that in order to calculate the external voltage the exact location of the nodes of Ranvier is required. The distance between successive nodes was approximated with the empirical relation between the internodal distance and the neuron diameter ($L = 115 \cdot D$) [210]. Then the axons paths were divided in segments of length $L$ (taking into account the diameter at each point) to calculate the exact locations of the nodes within the model geometry.

The electrodes that deliver the electrical stimulus were modeled as point current sources. This approximation yields an analytical expression to calculate the external voltage at each node of Ranvier:

$$V_e = \frac{\rho_e I_{el}}{4\pi r} \tag{7.4}$$

Where $\rho_e$ is the resistivity of the tissue that was set to $5\ \Omega \cdot m$ [290], $I_{el}$ is the current delivered by the electrode and $r$ is the distance between the electrode and the node of Ranvier.

The initiation of action potentials was detected through the evolution of the sodium currents across the membrane. Whenever the sodium current across the membrane showed a large and fast increase in at least one node it was determined that an action potential was triggered. This increase was detected by monitoring the gating parameters that drive the fast sodium current, $m$ and $h$ (see section 5.6).

To calculate the twitch fore, it was assumed that whenever an action potential is initiated it propagates in all directions along the axon. Therefore, regardless of the position where the action potential is generated, all the muscle fibers innervated by the MU are activated. Then relative twitch force was calculated by adding the forces of all MUs recruited by the electrical stimulus. Note that it was assumed that the forces of individual MUs sum in an additive manner, which is not exactly true. However, it has been shown that the summation of forces by individual MUs is almost linear across a wide range of forces [291].

## 7.3 Results and discussion

### 7.3.1 Generated model

Figure 7.3 shows the steps taken to generate the synthetic nervous tree. The tree consisted of: a) 4 major branches, b) an average of 10 minor branches per major branch, c) an average of 5 third level branches per minor branch, and d) a total of 12000 NMJ.

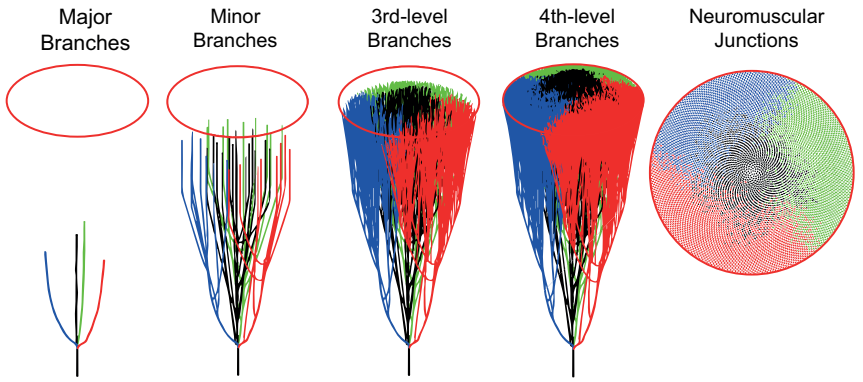


**Figure 7.3:** Steps of the synthetic nerve tree generation and the distribution of the neuromuscular junctions belonging to the different major branches at the motor end-plate region.

The nerve branching pattern created four clearly identifiable muscle compartments associated to the major branches with a slight overlap between them close to the motor end-plate region. The number of NMJs introduced into the model, which is equal to the number of muscle fibers, results in a fiber density of approximately 10 fibers/mm$^2$.

After building the nerve tree, the MU pool was generated and integrated into it. The resulting properties of the pool after integration are shown in Figure 7.4. The number of muscle fibers associated to each MU closely matched the values calculated theoretically from the Fuglevand model (Eq. 7.1). The average number of muscle fibers per MU is 100 and these fibers are distributed within a large range of values depending on the MU size. In particular, the large range of twitch forces used to generate the MU pool led to fiber numbers ranging from 5 to 463. The final MU pool generated had a large proportion of small MUs and a small population of large MUs as can be seen in the histograms of the force and axonal diameter distributions. Regarding the axonal diameter, the values obtained ranged between 2-22 $\mu$m which is consistent with the values measured in adult humans at the sciatic

nerve [292].

According to the results of Lu et al. [268], both axon diameter and arbor length are proportional to the square root of the motor unit size. In the case of the diameter, the relationship is unequivocally accomplished due to the assumptions made when calculating the force and diameter of the MUs. Namely that the twitch force of the MUs is proportional to the number of innervated fibers and that the diameter is proportional to the square root of the number of daughter branches. Regarding the arbor length, no restrictions were applied when allocating the MUs and therefore it was only limited by the tree geometry and the compartmentalization pattern. The arbor lengths of the MU pool fitted quite well a power function relating the length with the MU size with a power of 0.74 (arbor length $\propto$ Mu size$^{0.74}$). This discrepancy with the measurements by Lu et al. is likely related to the innervation architecture. Nonetheless, the meaning of this correlation is unknown and different proportionalities have been found (see for example [293]).

Examples of the axons generated by the integration of the MU pool in the nerve tree are depicted in Figure 7.5. The figure shows the locations of the Nodes of Ranvier as well as the positions of the muscle fibers innervated by the axon. In large MUs the internodal distance is larger as well as the portion of the muscle cross section activated by the axon.

### 7.3.2 Stimulation close to the nerve trunk

In first place we used our model to simulate stimulating the muscle with an electrode close to the nerve trunk. At this point axons are bundled up together inside the nerve and have not branched yet. Therefore selectivity in fiber recruitment is driven only by axonal diameter. We studied the response of the muscle when an electrical stimulus is delivered by an electrode located at a distance of 5 mm to the nerve trunk. We computed the force output as a function of the electrode current amplitude for a fixed pulse length (Figure 7.6(a)) and the force output and the percentage of MUs recruited as a function of the pulse length for a fixed electrode current amplitude (Figure 7.6 (b)).

The twitch force as a function of the current behaves roughly as a step response. The force output increases from 0 to close to 0.8 within a small range of currents (0.45-0.9 mA) due to the recruitment of all the strongest MUs. For larger currents, the addition of smaller MUs

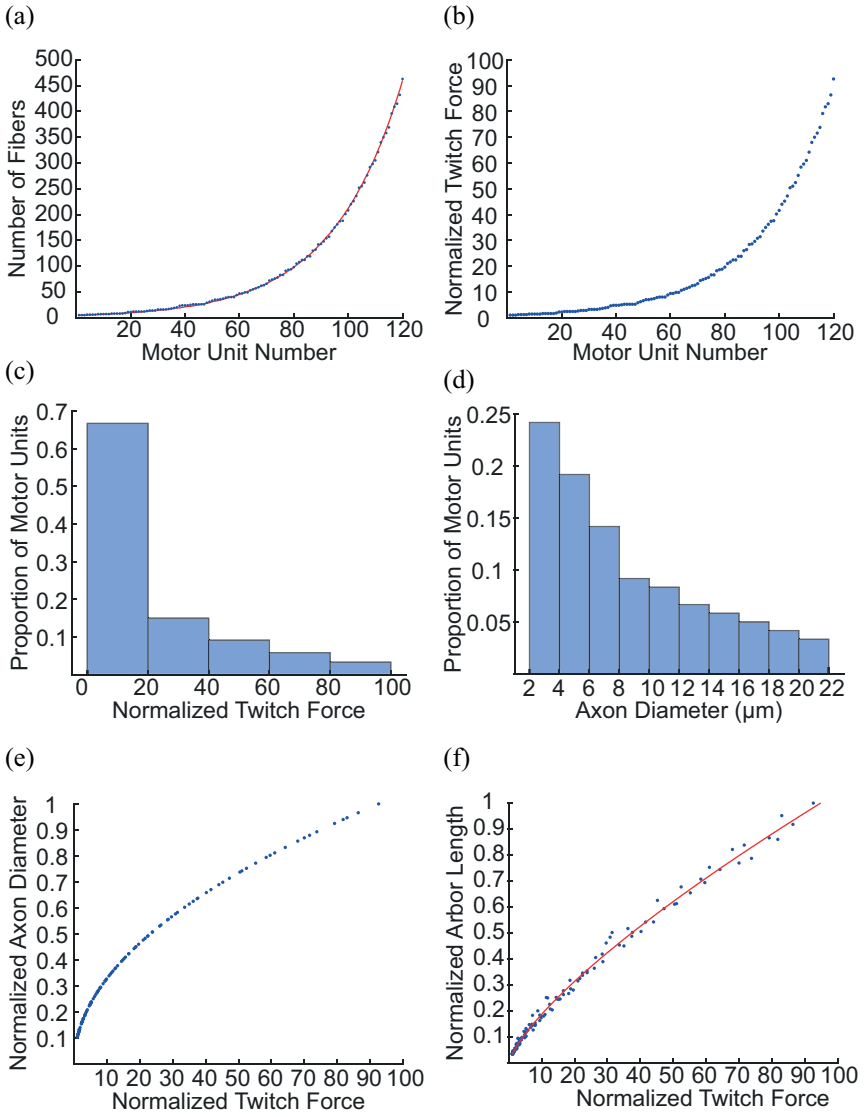


**Figure 7.4:** Properties of the MU pool after its integration into the nerve tree. (a) Number of muscle fibers innervated by each motor unit. Blue dots show the number of fibers of the model after the creation of the axons. The red line shows the number of fibers calculated from (7.1) before integrating the MUs into the nervous tree. (b) Twitch force of each MU normalized to the weakest MU. (c) MUs twitch force distribution. (d) Distribution of the axonal diameters at the nerve trunk. (e) Relation between the twitch force and the axon diameter (f) Relation between the arbor length and the twitch force. The red line shows the result of fitting a power function of the type $y = a \cdot x^b$. The exponent, $b$, that better fitted the results from our model was 0.74 ($R^2$=0.99).

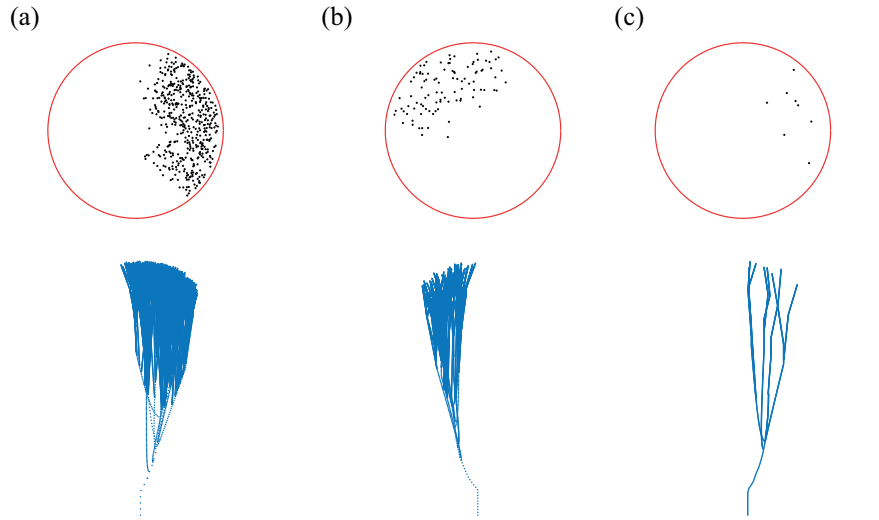


**Figure 7.5:** Examples of MUs of different sizes when are integrated into the nerve tree. On the top, cross section of the muscle with black dots showing the spatial distribution of the muscle fibers belonging to the MU. At the bottom, the nodes of Ranvier of the axon are represented. (a) and (c) represent one of the largest and one of the smallest MUs in the pool respectively and (b) belongs to a medium sized MU.

increases the force more gradually until all the fibers are recruited. A similar trend is observed when we study the force generation as a function of the pulse length. Note that in both cases the force reaches values above 90% of the maximum force by only recruiting around a 50% of the MUs. This is due to the force distribution within the MUs in the pool which causes that, despite of the small number of large MUs in the pool, the force response depends mostly on their activation. Therefore, although the MU pool consists of a large number of small MUs, their force contribution is very small in relative terms.

Our model assumes that all the axons virtually travel through the exact same path inside the nerve and neglects how they would spatially distribute within the nerve's cross section. Therefore, when stimulating close to the nerve trunk, the axons relative distances to the electrode are equal and MU recruitment depends purely on the axonal diameter. However, in a real nerve these axons would be spatially distributed within its cross section leading to different relative distances between the axons and the electrode. In order to quantify the effect of this approximation, we carried out a substudy in which

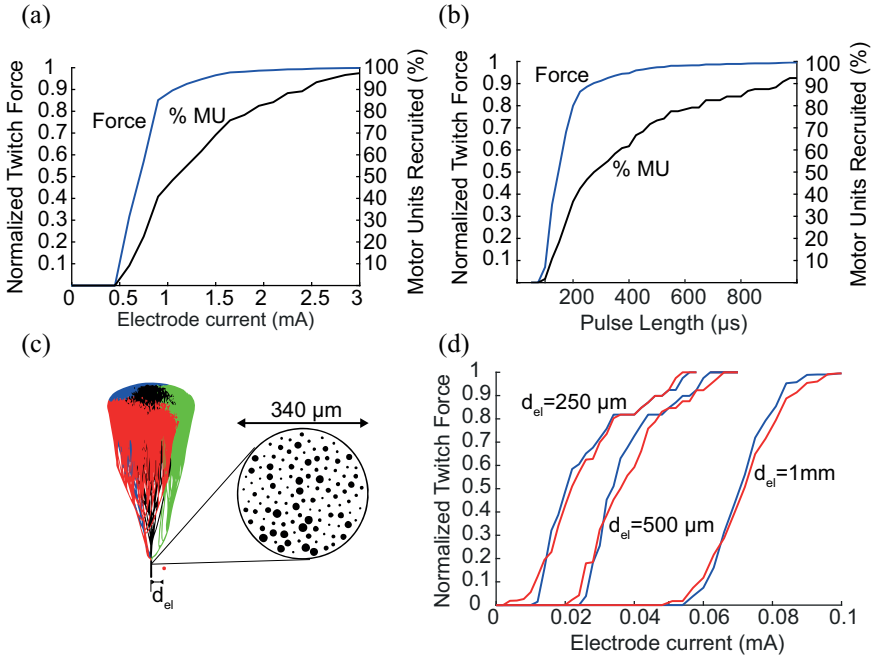


**Figure 7.6:** (a) Twitch force and percentage of motor units recruited as a function of the electrode current when a 250 $\mu$s pulse is delivered by an electrode located at a distance of 5 mm to the main nerve trunk. (b) Twitch force and percentage of motor units recruited as a function of the pulse length when a current of 1 mA is delivered by an electrode located at a distance of 5 mm to the main nerve trunk. (c) Schematic diagram showing the position of the electrode and the distribution of the axons inside the nerve trunk. (d) Effect of the axon location inside the nerve: Blue lines show the response of the muscle if all axons are virtually located at the center of the nerve. Red lines show the response of the muscle if axons are distributed within the nerve cross section (as in c). The graph shows twitch forces as a function of the electrode current when a 250 $\mu$s pulse is delivered by electrodes located at different distances ($d_{el}$) to the center of the nerve trunk.

we generated a random spatial distribution of axons within the nerve trunk cross section. The total nerve cross section was calculated by assuming that the axons occupy a 10% of the total cross section to account for the area occupied by connective tissue and blood vessels. This led to a nerve diameter of 340 $\mu$m. Using this diameter the axons were placed at random evenly spaced locations inside the nerve cross section (See Figure 7.6(c)) and we computed the force response of the muscle when stimulated with electrodes close to the trunk. These results were compared to the force responses obtained with all axons located at the center of the nerve (Figure 7.6(d)). The force response was roughly the same even for electrodes very close to the nerve trunk, therefore suggesting that the MU size plays a bigger role

in the recruitment than the axon location inside the nerve trunk.

### 7.3.3 Intramuscular stimulation

The goal of interleaved intramuscular stimulation with multiple electrodes is to activate non-overlapping portions of the muscle in a selective manner based on the spatial distribution of the MUs. In order to study the spatial selectivity we simulated electrodes placed inside the same muscle compartment by following the paths of one major branch and its daughter branches beginning at a location proximal to the nerve entry and moving the electrode distally. The positions were selected based on the branching order of the axons (see Figure 7.7), and the muscle response as a function of the current delivered by the electrode was computed.

The results in Figure 7.7 show that with a small current we can recruit MUs belonging to the targeted muscle compartment while sparing the rest of the compartments. In all electrode positions we can notice the appearance of plateaus in the current force curve. These plateaus are associated to the recruitment of MUs in the different compartments: once all MUs in one compartment are recruited if we keep increasing the current this may not lead to an increase in force if the current is not large enough to recruit MUs of the neighbor compartments. This feature has been observed experimentally in intramuscular stimulation and it was suggested to be a consequence of the muscle compartmentalization [294–298]. Therefore our results would reinforce this hypothesis.

It is interesting to note that the number and length of the plateaus increases as the electrode moves distally along the muscle. This is a consequence of the axonal propagation and branching: as the axons propagate inside the muscle, they extensively branch and their caliber is reduced, as a consequence, the diameters of all MUs tend to reach similar values and the impact of the MU size in the recruitment is reduced. This is further discussed below in view of the current-force curves in Figure 7.7.

In electrode 1 we can only identify a plateau after the MUs of the muscle compartment are recruited. Then, after this short plateau, MUs of the other compartments are recruited within a small range of currents and the force increases rapidly. This electrode is close to the nerve trunk, therefore the major branches are close to each other and the axon diameters are roughly the same as in the nerve trunk. Thus, although the geometry of the tree allows the gradual recruitment of

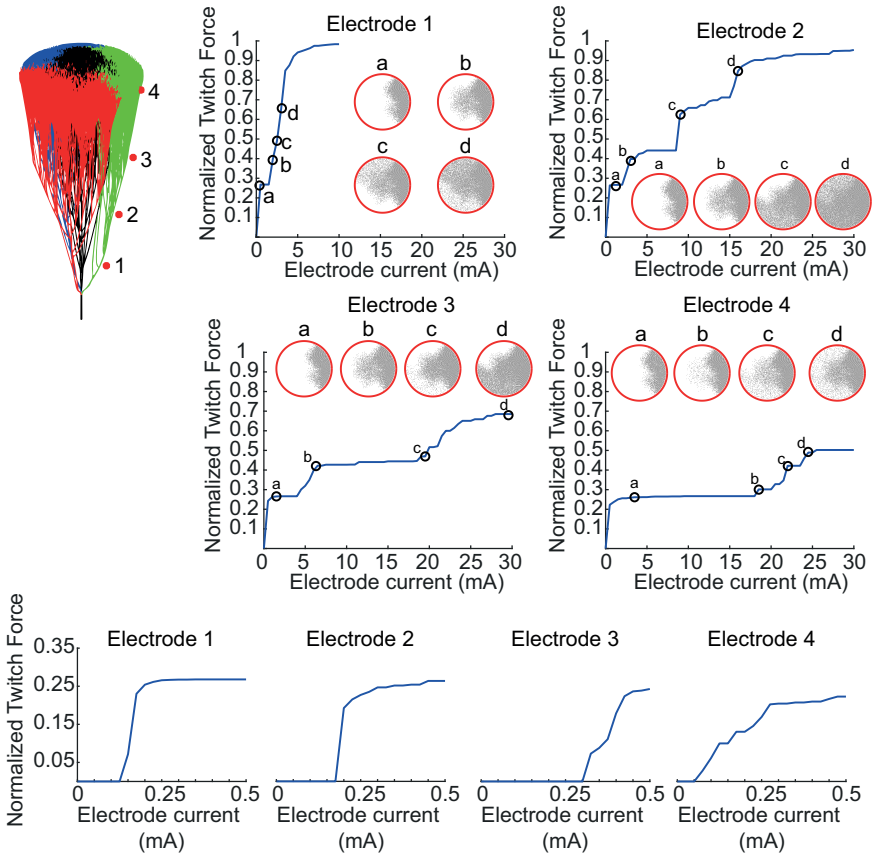


**Figure 7.7:** Current-Force relationships for electrodes located in the same muscle compartment at positions with different branching degrees. The graphs show the responses of the muscle to a 250 $\mu$s pulse as a function of the current amplitude delivered by the electrode. The circles show the portions of the muscle cross section that are activated in representative points of the curve. The current-force relationships displayed below are a magnification of the upper traces for a better visualization of the muscle response at small current amplitudes.

the different compartments, all large MUs of the muscle are recruited within a small range of currents.

In electrode 2 there is a similar scenario in terms of the axonal size distribution, however, the distance between muscle compartments is larger due to the expansion of the nerve tree. For this reason the currents at which each muscle compartment is activated can be clearly identified in the current force curve. The steep force increase every time a muscle compartment is activated indicates that all large MUs in the compartment are recruited within a narrow range of currents. Additionally we can also identify small leaps in the force associated

to the addition of medium sized MUs to the contraction. Therefore, we observed plateaus or steps of two different origins: on the one hand, the most easily identifiable, that are associated to the muscle compartmentalization (major branches). On the other hand, small steps that are not related to the axonal branching but to the different MU sizes.

In electrode 3 and especially in electrode 4, the axonal size distribution is very narrow and therefore the recruitment depends purely on the spatial location of the axons with respect to the electrode. The main trend arising from that is that the recruitment of the neighbor muscle compartments does not result in large and steep force increases as those seen in electrode 2. This is due to the fact that large MUs of the same compartment are recruited at significantly different currents based on their spatial locations. This causes the appearance of several small steps in the current force curve and allows the recruitment of small subsets of the fibers in the neighbor compartments. In fact, with electrode 4 we can recruit MUs from all four compartments without exceeding a 50% of the total force. Another noticeable feature in these traces is the significant enlargement of the plateaus. This is due to the larger distance between the electrode and the neighbor compartments as well as the smaller axonal size that reduces the excitability of the MUs to a distant electrode.

Up to this point we have discussed the recruitment of the different compartments without considering the possibility of recruiting only a portion of the compartment where the electrode is located. A closer look to the current force curves (bottom traces in Figure 7.7) shows a step like response of the muscle compartment when stimulating with electrodes 1 and 2. Therefore at these electrode locations the compartment is recruited in an all or none fashion. When stimulating with electrode 3, the response is also steep, however, the force increases in a more gradual fashion. Finally in electrode 4 we observe a more gradual recruitment and even intermediate plateaus. This indicates that, with fine control of the delivered current, it should be possible to independently activate fractions of the muscle compartment by placing electrodes close to the motor end-plate region. Nevertheless even at this ideal electrode placement region for interleaved stimulation, most of the fibers in the muscle compartment are recruited over a narrow range of currents (50-350 $\mu$A). The extensive branching of the large MUs causes that, regardless of the electrode position, there is at least an axonal branch close to the electrode. Therefore, selective recruitment of small portions of the muscle will be highly limited

by the inherent compartmentalization pattern of the muscle. Accurate electrode positioning with respect to the motor end-plate region and current delivery are critical in order to activate a subset of fibers within a muscle compartment and generate small forces.

Finally, in order to test recruitment at different locations, we placed a grid of equally spaced electrodes at four different planes. The same current and pulse length was applied in all them and the twitch forces generated by the stimulus were calculated. The results and the geometry of the simulations are depicted in Figure 7.8. In the planes located more proximally to the nerve entry we can clearly identify those electrode positions that activated only one muscle compartment (normalized force around 0.2) and those that activated more than one compartment (normalized force over 0.4). The electrode locations that resulted in a larger twitch force correspond to those that were near more than one muscle compartment.

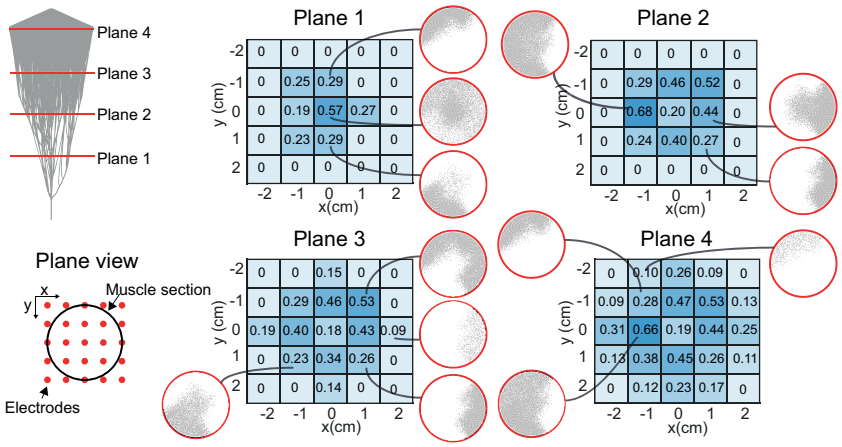


**Figure 7.8:** Force output as a function of the electrode position when a 2 mA stimulus with a pulse length of 250 $\mu$s is delivered. The circles show the portions of the muscle cross section that are activated in representative positions.

In the more distal planes we obtained twitch forces below 0.2 meaning that only a portion of the muscle compartment was activated. The electrode locations that yielded lower twitch forces correspond to those that are at a larger distance to any nervous branch. As explained above the extensive branching of the large motor axons difficults the selective activation of a small portion of a muscle compartment. Therefore those electrodes that are surrounded by the nervous tree recruit all the large MUs within a muscle compartment at a very low current.

### 7.3.4 General discussion

We presented a realistic neuromuscular model for intramuscular electrical stimulation that may help to interpret experimental results. In fact, it qualitatively reproduced experimental observations such as the large slope in the current-force curve when stimulating at the nerve trunk compared to intramuscular electrodes or the appearance of plateaus when stimulating in the muscle belly. These plateaus have always been interpreted as an evidence of the MU compartmentalization within the different nerve branches and the distance between those branches [294–298]. While our results reinforce this hypothesis, the model also predicts the appearance of small steps associated with the gradual recruitment of MUs innervated by the same major branch due to their different sizes. To the best of our knowledge, distinction between these two different steps has never been reported in the literature. This may be for two reasons: on the one hand, lack of resolution in the experimental measurements may have prevented their detection. On the other hand, these steps may appear as an artifact in our model due to the small number of MUs included.

Another interesting result we have obtained with the model is that, when stimulating with an electrode close to the motor end-plate region, the MUs of the closest compartment are recruited approximately in an order based on their size. This suggests that due to the extensive branching of the large motor axons the reversed recruitment order is maintained despite the disappearance of the differences in the axon diameters. Therefore, recruitment of MUs in a natural manner (size principle) may not be possible. However, stimulation strategies can be designed in order to minimize the drawbacks associated to electrical stimulation.

The main limitations of the model are associated with the assumption that all muscle fibers are equal and their contribution to the total force in a contraction is the same. It is well known that different types of muscle fibers exist in terms of their force generating ability and fatigability [91, 299]. However, although the force generated by a single MU depends not only on the number of fibers that it innervates but also on their size, there is a strong correlation between MU force and number of fibers [90]. Therefore, including different muscle fiber types in our model would only affect quantitatively the output forces but the trends and recruitment patterns observed would be the same. Note, however, that in order to simulate the time courses of muscle contractions, different types of muscle fibers would need to be

considered. Thus, including additional properties in the generation of the MU pool would be necessary in order to account for the different fatigue rates and contraction times within fiber types.

In the present study for the sake of simplicity we generated a synthetic intramuscular nerve distribution with the simplest structure that can be found in real muscles (unnipenate, single motor end-plate). However, more complex innervation patterns or 3-D maps of the nerve supply of real muscles could be integrated into the same modeling scheme.

All the simulations presented in this study were performed using a single monopolar electric pulse delivered by a point source electrode. However, the modeling scheme developed here would allow testing a wide variety waveform type and multiple electrode geometries. On the one hand, the axonal models based on the cable approximation have been extensively tested for different waveforms showing a good agreement with experimental results [2]. On the other hand, introducing realistic electrode geometries to the model could be done by calculating the potential distribution generated by the electrode through a finite elements method model [300].

## 7.4 Conclusions

We presented a model to simulate the force generated by a muscle as a result of intramuscular electrical stimulation. The proposed modeling scheme may serve as an *in silico* test bench for the design of new electrodes and devices as well as the optimization of interleaved stimulation protocols intended to reduce muscle fatigue. In addition, this model may also help interpreting experimental results. In fact, it reproduced trends observed experimentally such as the appearance of intermediate plateaus in the current-force curves obtained with intramuscular electrodes. Our results support the hypothesis that these plateaus appear as a consequence of the nerve distribution patterns inside the muscle.

Our results show that, due to the extensive branching of the axons associated to large MUs, the reversed recruitment order in electrical stimulation largely prevails regardless of the electrode position. Therefore physiological recruitment patterns may be impossible to mimic with intramuscular electrodes. In addition, the selective recruitment of small portions of the muscle seems to be highly limited by the intrinsic muscle compartmentalization of the MUs. However,

we showed that by placing the electrodes close to the motor end-plate region it is possible to recruit subsets of the muscle fibers within a compartment and obtain more graded forces. In addition, at these electrode positions the overlap between electrodes is minimized.

These results can be used a guide for ideal intramuscular electrode placement with multiple electrodes by making reference to anatomical landmarks. We showed that the optimal electrode positions in order to maximize the benefits of intramuscular stimulation are close to the motor end-plate regions. This is particularly relevant in order to successfully perform interleaved stimulation using intramuscular electrodes.

Chapter 8

# Conclusions

## 8.1 General conclusions

This thesis aimed at addressing questions in the fields of electroporation and peripheral nerve stimulation and, in particular, those questions that arise from the interaction between these two phenomenona.

Electroporation is a complex phenomenon that can trigger various effects in cells due to the membrane permeability increase to ions and molecules. Since electroporation occurs when the TMV induced by an external electric field reaches a certain threshold, Schwann equation provides a good estimation of the electric field at which electroporation is initiated in spherical cells. However, electroporation experiments rely on indirect measurements of the effects of electroporation. In order to detect electroporation a series of events need to take place which entails a process that is more complex than simply inducing a certain TMV. Thus, the assumption that the effects of electroporation for a specific electric field depend on cell size as predicted by Schwann equation needs to be taken with care. Depending on the detection method and its sensitivity it is possible find scenarios in which the electric field required to detect electroporation has a very weak dependence on cell size.

Two decades after the first report on PRF as a treatment for chronic pain, the exact mechanism of action of the treatment remains unknown. Several biological responses that could explain the pain relief after the treatment have been identified. Nevertheless, the underlying biophysical mechanisms by which the electric bursts trigger those responses have not been identified. Our hypothesis of an electroporation mediated $Ca^{2+}$ influx, could explain the effects that have been reported in the literature and would link those effects with a direct action of the electric fields. Indeed, we showed that PRF bursts can cause a $Ca^{2+}$ influx through a mechanism that depends on the induced TMV and is not related to thermal effects of any nature.

By using bursts of short bipolar pulses instead of monopolar pulses it is possible to take advantage of the long charging times exhibited by the membranes of the nerve fibers in order to minimize the muscle contractions that occur during IRE treatments. These long charging times are determined by the geometry of the nerve fibers, which are long and thin cable-like structures. Unlike nerve fibers, most cells in tissues tend to have geometries that resemble a spheroid, or at least that are significantly less elongated than nerve fibers. Thus, most cells display significantly shorter charging times compared to nerve fibers. As a consequence, when applying short bipolar pulses, the

TMV induced by an external electric field is significantly smaller in nerve fibers compared to other cells. In fact, bipolar pulses are less effective at inducing IRE compared to monopolar pulses and larger electric fields need to be delivered to compensate that. However, even requiring larger electric fields, muscle contractions can be largely avoided as a consequence of the long membrane charging times of nerve fibers.

In addition to prevent muscle contractions, bipolar pulses have the potential to reduce the extent of necrosis in a tissue ablation by means of IRE. Both monopolar and bipolar pulses can lead to a delayed cell death within a range of electric fields. However, this range is wider when using bipolar pulses. Additionally, the mechanisms of delayed cell death may be different between the two waveforms.

Finally, intramuscular electrical stimulation can help maximizing the benefits of interleaved stimulation in FES applications. The physiological recruitment patterns may be impossible to replicate with this approach and the selectivity in the recruitment of small portions of a muscle seems to be highly limited by its inherent compartmentalization. However, with the adequate electrode placing it may be possible to activate fractions of the muscle fibers within a compartment which would allow obtaining graded forces by means of electrical stimulation.

## 8.2 Future perspectives

Since the first clinical report on PRF treatments for chronic pain, the number of studies on the biological responses to this treatment has been continuously growing. The acquired knowledge contributed to create a picture of the responses caused by PRF that translate into a pain relief and more findings can be expected in the next years. However, the physical mechanisms by which PRF bursts trigger these responses have been relatively unexplored. The results presented in this thesis regarding the potential role of electroporation in these treatments are promising and could link the biological responses with a direct effect of the electric fields. However, further research is needed in order to elucidate the exact pathways of the $Ca^{2+}$ influx detected in our experiments. The response of a cell to an increase in the intracellular $Ca^{2+}$ levels are highly dependent its origins. Thus, a systematic study accounting all possible pathways would be required in order to link the biological responses in PRF with a $Ca^{2+}$ signaling process.

The use of IRE in medicine is relatively new and the treatment has

not been established yet in the clinical practice. The multiple ongoing clinical trials in the present indicate that important advances are likely going to be made in the near future that may help determining the treatment efficacy and its indications.

The use of H-FIRE waveforms seems to largely avoid all the issues related to neurostimulation that appear in conventional IRE treatments. This has triggered the interest of researchers in alternating polarity waveforms and their potential in electroporation based treatments. However, there is a challenge that will need to be faced which is related to the higher thresholds for cell death of this waveforms compared to conventional IRE protocols. The high electric field thresholds of H-FIRE waveforms highly limit the volume of tissue that can be treated at the same time without causing a thermal damage to the tissues. In some cases this may be a great disadvantage compared to the conventional IRE protocols and may prevent the widespread use of the H-FIRE waveforms. In contrast, the results presented in this thesis suggest that H-FIRE may reduce the extent of necrotic cell death in an ablation. This could have several benefits, however, further research will be needed to determine how this affects the body responses and the healing process after the treatment.

Finally, regarding the use of FES, there have been numerous advances in the last decades that boosted our understanding on how the neurmouscular system works and how we can electrically act on it. However, there is still a long way to go in order to be able to replicate a voluntary muscle contraction by means of electrical stimulation. Interleaved stimulation in combination with the use of intramuscular electrodes is probably the most promising approach to reach that goal. The success of this approach will depend on our ability to activate small portions of the muscles. In the present, there are two main research areas that could greatly enhance the selectivity of the stimulation systems. First, a better knowledge of the intramuscular nerve distribution is required in order to optimize the electrode placement and the stimulation strategies. Second, the development of new devices, electrodes or in general any technical solution that allows acting on a small portion of the nerve fibers inside a muscle is crucial to enhance the selectivity.

# References


[1] A. Rolong, R. V. Davalos, and B. Rubinsky, "History of electroporation," in *Irreversible Electroporation in Clinical Practice*. Cham: Springer International Publishing, 2017, pp. 13–37.

[2] J. P. Reilly, *Applied Bioelectricity*. New York, NY: Springer New York, 1998.

[3] L. R. Sheffler and J. Chae, "Neuromuscular electrical stimulation in neurorehabilitation," *Muscle and Nerve*, vol. 35, no. 5, pp. 562–590, 2007.

[4] M. L. Yarmush, A. Golberg, G. Serša, T. Kotnik, and D. Miklavčič, "Electroporation-Based Technologies for Medicine: Principles, Applications, and Challenges," *Annual Review of Biomedical Engineering*, vol. 16, no. 1, pp. 295–320, jul 2014.

[5] C. B. Arena and R. V. Davalos, "Advances in Therapeutic Electroporation to Mitigate Muscle Contractions," *Journal of Membrane Science & Technology*, vol. 02, no. 01, pp. 2–4, 2012.

[6] M. E. Sluijter, E. R. Cosman, W. B. Rittman, and M. Van Kleef, "The effects of pulsed radiofrequency fields applied to the dorsal root ganglion - a preliminary report," *The Pain Clinic*, vol. 11, no. 2, pp. 109–117, 1998.

[7] C. B. Arena, M. B. Sano, J. H. Rossmeisl, J. L. Caldwell, P. a. Garcia, M. Rylander, and R. V. Davalos, "High-frequency irreversible electroporation (H-FIRE) for non-thermal ablation without muscle contraction," *BioMedical Engineering OnLine*, vol. 10, no. 1, p. 102, 2011.

[8] S. Grimnes and Ø. G. Martinsen, *Bioimpedance and bioelectric-*

*ity basics*. San Diego: Academic, 2000.

[9] H. Fricke, "A Mathematical Treatment of the Electric Conductivity and Capacity of Disperse Systems ii. The Capacity of a Suspension of Conducting Spheroids Surrounded by a Non-Conducting Membrane for a Current of Low Frequency," *Physical Review*, vol. 26, no. 5, pp. 678–681, nov 1925.

[10] H. P. Schwan, "Electrical Properties of Tissue and Cell Suspensions," *Advances in Biological and Medical Physics*, vol. 5, pp. 147–209, 1957.

[11] T. Kotnik and D. Miklavčič, "Analytical description of transmembrane voltage induced by electric fields on spheroidal cells." *Biophysical Journal*, vol. 79, no. 2, pp. 670–679, aug 2000.

[12] G. Pucihar, T. Kotnik, B. Valič, and D. Miklavčič, "Numerical determination of transmembrane voltage induced on irregularly shaped cells," *Annals of Biomedical Engineering*, vol. 34, no. 4, pp. 642–652, 2006.

[13] E. W. Lee, J. Gehl, and S. T. Kee, "Introduction to Electroporation," in *Clinical Aspects of Electroporation*. New York, NY: Springer New York, 2011, pp. 3–7.

[14] A. Ivorra and B. Rubinsky, "Historical Review of Irreversible Electroporation in Medicine," in *Irreversible Electroporation*, B. Rubinsky, Ed. Berlin, Heidelberg: Series in Biomedical Engineering. Springer, 2010, pp. 1–21.

[15] R. Stämpfli and M. Willi, "Membrane potential of a ranvier node measured after electrical destruction of its membrane," *Experientia*, vol. 13, no. 7, pp. 297–298, 1957.

[16] R. Stämpfli, "Reversible electrical breakdown of the excitable membrane of a Ranvier node," *An Acad Brasil Cienc*, vol. 30, no. 1, pp. 57–61, 1958.

[17] A. Sale and W. Hamilton, "Effects of high electric fields on microorganismsI. Killing of bacteria and yeasts," *Biochimica et Biophysica Acta (BBA) - General Subjects*, vol. 148, no. 3, pp. 781–788, dec 1967.

[18] W. Hamilton and A. Sale, "Effects of high electric fields on microorganismsII. Mechanism of action of the lethal effect," *Biochimica et Biophysica Acta (BBA) - General Subjects*, vol. 148, no. 3, pp. 789–800, dec 1967.

[19] A. Sale and W. Hamilton, "Effects of high electric fields on micro-organisms," *Biochimica et Biophysica Acta (BBA) - Biomembranes*, vol. 163, no. 1, pp. 37–43, aug 1968.

[20] E. Neumann and K. Rosenheck, "Permeability changes induced by electric impulses in vesicular membranes," *The Journal of Membrane Biology*, vol. 10, no. 1, pp. 279–290, dec 1972.

[21] K. J. Kinosita and T. Y. Tsong, "Formation and resealing of pores of controlled sizes in human erythrocyte membrane." *Nature*, vol. 268, pp. 438–441, 1977.

[22] E. Neumann, M. Schaefer-Ridder, Y. Wang, and P. H. Hofschneider, "Gene transfer into mouse lyoma cells by electroporation in high electric fields." *The EMBO journal*, vol. 1, no. 7, pp. 841–5, 1982.

[23] I. Abiror, V. Arakelyan, L. Chernomordik, Y. Chizmadzhev, V. Pastushenko, and M. Tarasevich, "246 - Electric breakdown of bilayer lipid membranes I. The main experimental facts and their qualitative discussion," *Bioelectrochemistry and Bioenergetics*, vol. 6, no. 1, pp. 37–52, mar 1979.

[24] R. W. Glaser, S. L. Leikin, L. V. Chernomordik, V. F. Pastushenko, and A. I. Sokirko, "Reversible electrical breakdown of lipid bilayers: Formation and Evolution of Pores," *Biochimica et biophysica acta*, vol. 940, pp. 275–287, 1988.

[25] K. Kinosita, I. Ashikawa, N. Saita, H. Yoshimura, H. Itoh, K. Nagayama, and A. Ikegami, "Electroporation of cell membrane visualized under a pulsed-laser fluorescence microscope." *Biophysical journal*, vol. 53, no. 6, pp. 1015–9, 1988.

[26] K. C. Melikov, V. A. Frolov, A. Shcherbakov, A. V. Samsonov, Y. A. Chizmadzhev, and L. V. Chernomordik, "Voltage-induced nonconductive pre-pores and metastable single pores in unmodified planar lipid bilayer." *Biophysical journal*, vol. 80, no. 4, pp. 1829–36, 2001.

[27] J. Teissié and M. P. Rols, "An experimental evaluation of the critical potential difference inducing cell membrane electropermeabilization." *Biophysical Journal*, vol. 65, no. 1, pp. 409–413, jul 1993.

[28] U. Zimmermann, G. Pilwat, and F. Riemann, "Dielectric Breakdown of Cell Membranes," *Biophysical Journal*, vol. 14, no. 11, pp. 881–899, nov 1974.

[29] A. Ivorra, "Tissue Electroporation as a Bioelectric Phenomenon: Basic Concepts," in *Irreversible Electroporation*, B. Rubinsky, Ed. Berlin, Heidelberg: Springer Berlin Heidelberg, 2010, pp. 23–61.

[30] R. Benz and U. Zimmermann, "Pulse-length dependence of the

electrical breakdown in lipid bilayer membranes," *Biochimica et Biophysica Acta (BBA) - Biomembranes*, vol. 597, no. 3, pp. 637–642, apr 1980.

[31] W. Frey, J. White, R. Price, P. Blackmore, R. Joshi, R. Nuccitelli, S. Beebe, K. Schoenbach, and J. Kolb, "Plasma Membrane Voltage Changes during Nanosecond Pulsed Electric Field Exposure," *Biophysical Journal*, vol. 90, no. 10, pp. 3608–3615, may 2006.

[32] J. A. White, U. Pliquett, P. F. Blackmore, R. P. Joshi, K. H. Schoenbach, and J. F. Kolb, "Plasma membrane charging of Jurkat cells by nanosecond pulsed electric fields," *European Biophysics Journal*, vol. 40, no. 8, pp. 947–957, aug 2011.

[33] L. Delemotte and M. Tarek, "Molecular Dynamics Simulations of Lipid Membrane Electroporation," *The Journal of Membrane Biology*, vol. 245, no. 9, pp. 531–543, 2012.

[34] M. Tarek, "Membrane Electroporation: A Molecular Dynamics Simulation," *Biophysical Journal*, vol. 88, no. 6, pp. 4045–4053, 2005.

[35] M. Hibino, H. Itoh, and K. Kinosita, "Time courses of cell electroporation as revealed by submicrosecond imaging of transmembrane potential," *Biophysical Journal*, vol. 64, no. 6, pp. 1789–1800, jun 1993.

[36] Y. Demiryurek, M. Nickaeen, M. Zheng, M. Yu, J. D. Zahn, D. I. Shreiber, H. Lin, and J. W. Shan, "Transport, resealing, and re-poration dynamics of two-pulse electroporation-mediated molecular delivery," *Biochimica et Biophysica Acta (BBA) - Biomembranes*, vol. 1848, no. 8, pp. 1706–1714, 2015.

[37] M. Pavlin and D. Miklavčič, "Theoretical and experimental analysis of conductivity, ion diffusion and molecular transport during cell electroporation — Relation between short-lived and long-lived pores," *Bioelectrochemistry*, vol. 74, no. 1, pp. 38–46, nov 2008.

[38] M. Pavlin, V. Leben, and D. Miklavčič, "Electroporation in dense cell suspension—Theoretical and experimental analysis of ion diffusion and cell permeabilization," *Biochimica et Biophysica Acta (BBA) - General Subjects*, vol. 1770, no. 1, pp. 12–23, jan 2007.

[39] A. Silve, A. Guimerà Brunet, B. Al-Sakere, A. Ivorra, and L. Mir, "Comparison of the effects of the repetition rate between microsecond and nanosecond pulses: Electropermeabilization-

induced electro-desensitization?" *Biochimica et Biophysica Acta (BBA) - General Subjects*, vol. 1840, no. 7, pp. 2139–2151, jul 2014.

[40] L. H. Wegner, "The conductance of cellular membranes at supra-physiological voltages," *Bioelectrochemistry*, vol. 103, pp. 34–38, 2015.

[41] L. H. Wegner, B. Flickinger, C. Eing, T. Berghöfer, P. Hohenberger, W. Frey, and P. Nick, "A patch clamp study on the electro-permeabilization of higher plant cells: Supra-physiological voltages induce a high-conductance, K+ selective state of the plasma membrane," *Biochimica et Biophysica Acta (BBA) - Biomembranes*, vol. 1808, no. 6, pp. 1728–1736, jun 2011.

[42] L. H. Wegner, W. Frey, and A. Silve, "Electroporation of DC-3F cells is a dual process," *Biophysical Journal*, vol. 108, no. 7, pp. 1660–1671, 2015.

[43] T. Kotnik, P. Kramar, G. Pucihar, D. Miklavčič, and M. Tarek, "Cell membrane electroporation- Part 1: The phenomenon," *IEEE Electrical Insulation Magazine*, vol. 28, no. 5, pp. 14–23, sep 2012.

[44] T. Kotnik, L. Rems, M. Tarek, and D. Miklavčič, "Membrane Electroporation and Electropermeabilization: Mechanisms and Models," *Annual Review of Biophysics*, vol. 48, no. 1, pp. 63–91, 2019.

[45] E. Neumann, K. Toensing, S. Kakorin, P. Budde, and J. Frey, "Mechanism of electroporative dye uptake by mouse B cells." *Biophysical journal*, vol. 74, no. 1, pp. 98–108, 1998.

[46] D. P. Tieleman, "The molecular basis of electroporation," *BMC Biochemistry*, vol. 5, no. 1, pp. 1–12, 2004.

[47] G. Pucihar, T. Kotnik, D. Miklavčič, and J. Teissié, "Kinetics of Transmembrane Transport of Small Molecules into Electropermeabilized Cells," *Biophysical Journal*, vol. 95, no. 6, pp. 2837–2848, sep 2008.

[48] M. P. Rols and J. Teissié, "Electropermeabilization of mammalian cells. Quantitative analysis of the phenomenon." *Biophysical journal*, vol. 58, no. 5, pp. 1089–98, 1990.

[49] M.-P. Rols and J. Teissié, "Experimental evidence for the involvement of the cytoskeleton in mammalian cell electropermeabilization," *Biochimica et biophysica acta*, vol. 1111, pp. 45–50, 1992.

[50] J. Teissie and M. Rols, "Fusion of mammalian cells in culture is obtained by creating the contact between cells after their electropermeabilization," *Biochemical and Biophysical Research Communications*, vol. 140, no. 1, pp. 258–266, oct 1986.

[51] M. Puc, T. Kotnik, L. M. Mir, and D. Miklavčič, "Quantitative model of small molecules uptake after in vitro cell electropermeabilization," *Bioelectrochemistry*, vol. 60, no. 1-2, pp. 1–10, aug 2003.

[52] E. Tekle, R. D. Astumian, and P. B. Chock, "Electropermeabilization of cell membranes: Effect of the resting membrane potential," *Biochemical and Biophysical Research Communications*, vol. 172, no. 1, pp. 282–287, oct 1990.

[53] E. Tekle, R. D. Astumian, and P. B. Chock, "Electroporation by using bipolar oscillating electric field: an improved method for DNA transfection of NIH 3T3 cells." *Proceedings of the National Academy of Sciences of the United States of America*, vol. 88, no. 10, pp. 4230–4234, 1991.

[54] E. Tekle, R. D. Astumian, and P. B. Chock, "Selective and asymmetric molecular transport across electroporated cell membranes." *Proceedings of the National Academy of Sciences*, vol. 91, no. 24, pp. 11 512–11 516, nov 1994.

[55] T. Batista Napotnik and D. Miklavčič, "In vitro electroporation detection methods – An overview," *Bioelectrochemistry*, vol. 120, pp. 166–182, 2018.

[56] Q. Castellví, B. Mercadal, and A. Ivorra, "Assessment of Electroporation by Electrical Impedance Methods," in *Handbook of Electroporation*, D. Miklavčič, Ed. Cham: Springer International Publishing, 2016, pp. 1–20.

[57] L. H. Wegner, "Patch Clamp in Use of Electroporation Mechanisms Studies," in *Handbook of Electroporation*, D. Miklavčič, Ed. Cham: Springer International Publishing, 2016, pp. 1–23.

[58] L. M. Mir, S. Orlowski, J. Belehradek, and C. Paoletti, "Electrochemotherapy potentiation of antitumour effect of bleomycin by local electric pulses," *European Journal of Cancer and Clinical Oncology*, vol. 27, no. 1, pp. 68–72, 1991.

[59] M. Belehradek, C. Domenge, B. Luboinski, S. Orlowski, J. Belehradek, and L. M. Mir, "Electrochemotherapy, a new antitumor treatment. First clinical phase I-II trial," *Cancer*, vol. 72, no. 12, pp. 3694–3700, 1993.

[60] M. Marty, G. Sersa, J. R. Garbay, J. Gehl, C. G. Collins,

M. Snoj, V. Billard, P. F. Geertsen, J. O. Larkin, D. Miklavčič, I. Pavlovic, S. M. Paulin-Kosir, M. Cemazar, N. Morsli, D. M. Soden, Z. Rudolf, C. Robert, G. C. O'Sullivan, and L. M. Mir, "Electrochemotherapy - An easy, highly effective and safe treatment of cutaneous and subcutaneous metastases: Results of ESOPE (European Standard Operating Procedures of Electrochemotherapy) study," *European Journal of Cancer, Supplement*, vol. 4, no. 11, pp. 3–13, 2006.

[61] B. Mali, T. Jarm, M. Snoj, G. Sersa, and D. Miklavčič, "Antitumor effectiveness of electrochemotherapy: A systematic review and meta-analysis," *European Journal of Surgical Oncology*, vol. 39, no. 1, pp. 4–16, 2013.

[62] L. M. Mir, J. Gehl, G. Sersa, C. G. Collins, J. R. Garbay, V. Billard, P. F. Geertsen, Z. Rudolf, G. C. O'Sullivan, and M. Marty, "Standard operating procedures of the electrochemotherapy: Instructions for the use of bleomycin or cisplatin administered either systemically or locally and electric pulses delivered by the Cliniporator$ˆTM$ by means of invasive or non-invasive electrodes," *European Journal of Cancer, Supplement*, vol. 4, no. 11, pp. 14–25, 2006.

[63] D. Miklavčič, G. Serša, E. Brecelj, J. Gehl, D. Soden, G. Bianchi, P. Ruggieri, C. R. Rossi, L. G. Campana, and T. Jarm, "Electrochemotherapy: Technological advancements for efficient electroporation-based treatment of internal tumors," *Medical and Biological Engineering and Computing*, vol. 50, no. 12, pp. 1213–1225, 2012.

[64] R. V. Davalos, L. M. Mir, and B. Rubinsky, "Tissue ablation with irreversible electroporation," *Annals of Biomedical Engineering*, vol. 33, no. 2, pp. 223–231, 2005.

[65] J. Edd, L. Horowitz, R. Davalos, L. Mir, and B. Rubinsky, "In Vivo Results of a New Focal Tissue Ablation Technique: Irreversible Electroporation," *IEEE Transactions on Biomedical Engineering*, vol. 53, no. 7, pp. 1409–1415, jul 2006.

[66] B. Rubinsky, G. Onik, and P. Mikus, "Irreversible Electroporation: A New Ablation Modality — Clinical Implications," *Technology in Cancer Research & Treatment*, vol. 6, no. 1, pp. 37–48, feb 2007.

[67] B. Rubinsky, *Experimental Studies on Non-thermal Irreversible Electroporation in Tissue*. Berlin, Heidelberg: Springer Berlin Heidelberg, 2010, pp. 155–181.

[68] E. W. Lee, S. Thai, and S. T. Kee, "Irreversible electroporation: A novel image-guided cancer therapy," *Gut and Liver*, vol. 4, no. SUPPL. 1, pp. 99–104, 2010.

[69] G. Onik and B. Rubinsky, *Irreversible Electroporation: First Patient Experience Focal Therapy of Prostate Cancer*. Berlin, Heidelberg: Springer Berlin Heidelberg, 2010, pp. 235–247.

[70] G. Onik, P. Mikus, and B. Rubinsky, "Irreversible electroporation: implications for prostate ablation." *Technology in cancer research & treatment*, vol. 6, no. 4, pp. 295–300, 2007.

[71] C. Jiang, R. V. Davalos, and J. C. Bischof, "A Review of Basic to Clinical Studies of Irreversible Electroporation Therapy," *IEEE Transactions on Biomedical Engineering*, vol. 62, no. 1, pp. 4–20, jan 2015.

[72] L. C. Heller and R. Heller, "Electroporation Gene Therapy Preclinical and Clinical Trials for Melanoma," *Current Gene Therapy*, vol. 10, no. 4, pp. 312–317, aug 2010.

[73] L. Low, A. Mander, K. McCann, D. Dearnaley, T. Tjelle, I. Mathiesen, F. Stevenson, and C. H. Ottensmeier, "DNA Vaccination with Electroporation Induces Increased Antibody Responses in Patients with Prostate Cancer," *Human Gene Therapy*, vol. 20, no. 11, pp. 1269–1278, nov 2009.

[74] M. Nomura, Y. Nakata, T. Inoue, A. Uzawa, S. Itamura, K. Nerome, M. Akashi, and G. Suzuki, "In vivo induction of cytotoxic T lymphocytes specific for a single epitope introduced into an unrelated molecule," *Journal of Immunological Methods*, vol. 193, no. 1, pp. 41–49, jun 1996.

[75] A. C. Guyton and J. E. Hall, *Textbook of Medical Physiology*, 10th ed. Philadelphia: W.B. Saunders Company, 2000.

[76] C. H. Ho, R. J. Triolo, A. L. Elias, K. L. Kilgore, A. F. DiMarco, K. Bogie, A. H. Vette, M. L. Audu, R. Kobetic, S. R. Chang, K. M. Chan, S. Dukelow, D. J. Bourbeau, S. W. Brose, K. J. Gustafson, Z. H. T. Kiss, and V. K. Mushahwar, "Functional electrical stimulation and Spinal Cord Injury," *Physical Medicine and Rehabilitation Clinics of North America*, vol. 25, no. 3, pp. 631–654, aug 2014.

[77] J. Zheng and M. C. Trudeau, Eds., *Handbook of Ion Channels*. CRC Press, 2016.

[78] J. Erlanger and H. S. Gasser, "The compound nature of the aciton current of nerve as disclosed by the cathode ray oscillograph," *American Journal of Physiology-Legacy Content*,

vol. 70, no. 3, pp. 624–666, nov 1924.

[79] J. Erlanger and H. S. Gasser, "The action potential in fibers of slow conduction in spinal roots and somatic nerves," *American Journal of Physiology-Legacy Content*, vol. 92, no. 1, pp. 43–82, feb 1930.

[80] H. S. Gasser, "The classification of nerve fibers." *Ohio Journal of Science*, vol. 41, pp. 145–159, 1941.

[81] G. M. Manzano, L. M. Giuliano, and J. A. Nóbrega, "A brief historical note on the classification of nerve fibers," *Arquivos de Neuro-Psiquiatria*, vol. 66, no. 1, pp. 117–119, mar 2008.

[82] I. Varga and B. Mravec, "Nerve Fiber Types," in *Nerves and Nerve Injuries*. Elsevier, 2015, vol. 1, pp. 107–113.

[83] A. L. Hodgkin and A. F. Huxley, "Action Potentials Recorded from Inside a Nerve Fibre," *Nature*, vol. 144, no. 3651, pp. 710–711, oct 1939.

[84] A. L. Hodgkin and A. F. Huxley, "A quantitative description of membrane current and its application to conduction and excitation in nerve," *The Journal of Physiology*, vol. 117, no. 4, pp. 500–544, aug 1952.

[85] B. Frankenhaeuser and A. F. Huxley, "The action potential in the myelinated nerve fibre of Xenopus laevis as computed on the basis of voltage clamp data," *The Journal of Physiology*, vol. 171, no. 2, pp. 302–315, jun 1964.

[86] D. R. McNeal, "Analysis of a Model for Excitation of Myelinated Nerve," *IEEE Transactions on Biomedical Engineering*, vol. BME-23, no. 4, pp. 329–337, jul 1976.

[87] a. G. Richardson, C. C. McIntyre, and W. M. Grill, "Modelling the effects of electric fields on nerve fibres: Influence of the myelin sheath," *Medical & Biological Engineering & Computing*, vol. 38, no. 4, pp. 438–446, jul 2000.

[88] W. Rall, "Core Conductor Theory and Cable Properties of Neurons," in *The handbook of physiology, nervous system, vol 1: Cellular biology of neurons*, E. Kandel, J. Brookhart, and V. Montcastle, Eds. Bethesda, MD, USA: American Physiological Society, jan 1977, pp. 39–97.

[89] F. Buchthal and H. Schmalbruch, "Motor unit of mammalian muscle." *Physiological Reviews*, vol. 60, no. 1, pp. 90–142, jan 1980.

[90] J. E. Totosy de Zepetnek, H. V. Zung, S. Erdebil, and T. Gordon, "Innervation ratio is an important determinant of force in

normal and reinnervated rat tibialis anterior muscles," *Journal of Neurophysiology*, vol. 67, no. 5, pp. 1385–1403, may 1992.

[91] C. Heckman and R. M. Enoka, "Motor Unit," in *Comprehensive Physiology*. Hoboken, NJ, USA: John Wiley & Sons, Inc., oct 2012, vol. 2, no. 4, pp. 2629–2682.

[92] E. Henneman, "Relation between size of neurons and their susceptibility to discharge." *Science*, vol. 126, no. 3287, pp. 1345–7, dec 1957.

[93] P. Feiereisen, J. Duchateau, and K. Hainaut, "Motor unit recruitment order during voluntary and electrically induced contractions in the tibialis anterior," *Experimental Brain Research*, vol. 114, no. 1, pp. 117–123, 1997.

[94] B. M. Doucet, A. Lam, and L. Griffin, "Neuromuscular electrical stimulation for skeletal muscle function." *The Yale journal of biology and medicine*, vol. 85, no. 2, pp. 201–15, jun 2012.

[95] M. O. Ibitoye, N. A. Hamzaid, N. Hasnan, A. K. A. Wahab, and G. M. Davis, "Strategies for rapid muscle fatigue reduction during FES exercise in individuals with spinal cord injury: A systematic review," *PLoS ONE*, vol. 11, no. 2, pp. 1–28, 2016.

[96] E. D. H. Zonnevijlle, N. N. Somia, R. W. Stremel, C. J. Maldonado, P. M. N. Werker, M. Kon, and J. H. Barker, "Sequential segmental neuromuscular stimulation: An effective approach to enhance fatigue resistance," *Plastic and Reconstructive Surgery*, vol. 105, no. 2, pp. 667–673, 2000.

[97] A. Zupanic, B. Kos, and D. Miklavčič, "Treatment planning of electroporation-based medical interventions: electrochemotherapy, gene electrotransfer and irreversible electroporation," *Physics in Medicine and Biology*, vol. 57, no. 17, pp. 5425–5440, sep 2012.

[98] M. Okino, H. Tomie, H. Kanesada, M. Marumoto, K. Esato, and H. Suzuki, "Optimal Electric Conditions in Electrical Impulse Chemotherapy," *Japanese Journal of Cancer Research*, vol. 83, no. 10, pp. 1095–1101, oct 1992.

[99] B. Mali, T. Jarm, F. Jager, and D. Miklavčič, "An algorithm for synchronization of in vivo electroporation with ECG," *Journal of Medical Engineering & Technology*, vol. 29, no. 6, pp. 288–296, jan 2005.

[100] A. Golberg and B. Rubinsky, "Towards Electroporation Based Treatment Planning considering Electric Field Induced Muscle Contractions," *Technology in Cancer Research & Treatment*,

vol. 11, no. 2, pp. 189–201, apr 2012.

[101] I. Daskalov, N. Mudrov, and E. Peycheva, "Exploring new instrumentation parameters for electrochemotherapy. Attacking tumors with bursts of biphasic pulses instead of single pulses," *IEEE Engineering in Medicine and Biology Magazine*, vol. 18, no. 1, pp. 62–66, 1999.

[102] D. Miklavčič, G. Pucihar, M. Pavlovec, S. Ribarič, M. Mali, A. Maček-Lebar, M. Petkovšek, J. Nastran, S. Kranjc, M. Čemažar, and G. Serša, "The effect of high frequency electric pulses on muscle contractions and antitumor efficiency in vivo for a potential use in clinical electrochemotherapy," *Bioelectrochemistry*, vol. 65, no. 2, pp. 121–128, feb 2005.

[103] T. J. O'Brien, M. Passeri, M. F. Lorenzo, J. K. Sulzer, W. B. Lyman, J. H. Swet, D. Vrochides, E. H. Baker, D. A. Iannitti, R. V. Davalos, and I. H. McKillop, "Experimental High-Frequency Irreversible Electroporation Using a Single-Needle Delivery Approach for Nonthermal Pancreatic Ablation In Vivo," *Journal of Vascular and Interventional Radiology*, vol. 30, no. 6, pp. 854–862.e7, jun 2019.

[104] V. M. Ringel-Scaia, N. Beitel-White, M. F. Lorenzo, R. M. Brock, K. E. Huie, S. Coutermarsh-Ott, K. Eden, D. K. McDaniel, S. S. Verbridge, J. H. Rossmeisl, K. J. Oestreich, R. V. Davalos, and I. C. Allen, "High-frequency irreversible electroporation is an effective tumor ablation strategy that induces immunologic cell death and promotes systemic anti-tumor immunity," *EBioMedicine*, may 2019.

[105] I. A. Siddiqui, E. L. Latouche, M. R. DeWitt, J. H. Swet, R. C. Kirks, E. H. Baker, D. A. Iannitti, D. Vrochides, R. V. Davalos, and I. H. McKillop, "Induction of rapid, reproducible hepatic ablations using next-generation, high frequency irreversible electroporation (H-FIRE) in vivo," *HPB*, vol. 18, no. 9, pp. 726–734, sep 2016.

[106] I. A. Siddiqui, R. C. Kirks, E. L. Latouche, M. R. DeWitt, J. H. Swet, E. H. Baker, D. Vrochides, D. A. Iannitti, R. V. Davalos, and I. H. McKillop, "High-Frequency Irreversible Electroporation: Safety and Efficacy of Next-Generation Irreversible Electroporation Adjacent to Critical Hepatic Structures," *Surgical Innovation*, vol. 24, no. 3, pp. 276–283, jun 2017.

[107] C. Yao, S. Dong, Y. Zhao, Y. Lv, H. Liu, L. Gong, J. Ma, H. Wang, and Y. Sun, "Bipolar Microsecond Pulses and In-

sulated Needle Electrodes for Reducing Muscle Contractions during Irreversible Electroporation," *IEEE Transactions on Biomedical Engineering*, vol. 9294, no. c, pp. 1–1, 2017.

[108] G. Abramov, M. Bier, M. Capelli-Schellpfeffer, and R. Lee, "Alteration in sensory nerve function following electrical shock," *Burns*, vol. 22, no. 8, pp. 602–606, dec 1996.

[109] H. Gissel and T. Clausen, "Ca 2+ uptake and cellular integrity in rat EDL muscle exposed to electrostimulation, electroporation, or A23187," *American Journal of Physiology - Regulatory, Integrative and Comparative Physiology*, vol. 285, no. 1, pp. R132–R142, jul 2003.

[110] T. Clausen and H. Gissel, "Role of Na+,K+ pumps in restoring contractility following loss of cell membrane integrity in rat skeletal muscle," *Acta Physiologica Scandinavica*, vol. 183, no. 3, pp. 263–271, mar 2005.

[111] R. P. Joshi, A. Mishra, Q. Hu, K. H. Schoenbach, and A. Pakhomov, "Self-consistent analyses for potential conduction block in nerves by an ultrashort high-intensity electric pulse," *Physical Review E*, vol. 75, no. 6, p. 061906, jun 2007.

[112] C. C. Roth, G. P. Tolstykh, J. a. Payne, M. a. Kuipers, G. L. Thompson, M. N. DeSilva, and B. L. Ibey, "Nanosecond pulsed electric field thresholds for nanopore formation in neural cells." *Journal of biomedical optics*, vol. 18, no. 3, p. 035005, 2013.

[113] S. W. Flavell and M. E. Greenberg, "Signaling Mechanisms Linking Neuronal Activity to Gene Expression and Plasticity of the Nervous System," *Annual Review of Neuroscience*, vol. 31, no. 1, pp. 563–590, 2008.

[114] U. Wojda, E. Salinska, and J. Kuznicki, "Calcium ions in neuronal degeneration," *IUBMB Life*, vol. 60, no. 9, pp. 575–590, sep 2008.

[115] W. Li, Q. Fan, Z. Ji, X. Qiu, and Z. Li, "The Effects of Irreversible Electroporation (IRE) on Nerves," *PLoS ONE*, vol. 6, no. 4, p. e18831, apr 2011.

[116] H. Schoellnast, S. Monette, P. C. Ezell, A. Deodhar, M. Maybody, J. P. Erinjeri, M. D. Stubblefield, G. W. Single, W. C. Hamilton, and S. B. Solomon, "Acute and Subacute Effects of Irreversible Electroporation on Nerves: Experimental Study in a Pig Model," *Radiology*, vol. 260, no. 2, pp. 421–427, aug 2011.

[117] H. Schoellnast, S. Monette, P. C. Ezell, M. Maybody, J. P. Erinjeri, M. D. Stubblefield, G. Single, and S. B. Solomon, "The de-

layed effects of irreversible electroporation ablation on nerves," *European Radiology*, vol. 23, no. 2, pp. 375–380, feb 2013.

[118] A. Waller, "XX. Experiments on the section of the glossopharyngeal and hypoglossal nerves of the frog, and observations of the alterations produced thereby in the structure of their primitive fibres," *Philosophical Transactions of the Royal Society of London*, vol. 140, no. 1850, pp. 423–429, jan 1850.

[119] M. G. Burnett, E. L. Zager, M. A. R. K. G. B. Urnett, and E. R. I. C. L. Z. Ager, "Pathophysiology of peripheral nerve injury : a brief review," *Neurosurgical focus*, vol. 16, no. 5, pp. 1–7, 2004.

[120] A. Agarwal, I. Zudans, E. A. Weber, J. Olofsson, O. Orwar, and S. G. Weber, "Effect of Cell Size and Shape on Single-Cell Electroporation," *Analytical Chemistry*, vol. 79, no. 10, pp. 3589–3596, may 2007.

[121] C. Mauroy, T. Portet, M. Winterhalder, E. Bellard, M. C. Blache, J. Teissié, A. Zumbusch, and M. P. Rols, "Giant lipid vesicles under electric field pulses assessed by non invasive imaging," *Bioelectrochemistry*, vol. 87, pp. 253–259, 2012.

[122] S. Sixou and J. Teissié, "Specific electropermeabilization of leucocytes in a blood sample and application to large volumes of cells," *Biochimica et Biophysica Acta (BBA) - Biomembranes*, vol. 1028, no. 2, pp. 154–160, 1990.

[123] E. Tekle, R. Astumian, W. Friauf, and P. Chock, "Asymmetric Pore Distribution and Loss of Membrane Lipid in Electroporated DOPC Vesicles," *Biophysical Journal*, vol. 81, no. 2, pp. 960–968, aug 2001.

[124] M. Ĉemazâr, T. Jarm, D. Miklavĉiĉ, A. M. Lebar, A. Ihan, N. A. Kopitar, and G. Serŝa, "Effect of Electric-Field Intensity on Electropermeabilization and Electrosensitmty of Various Tumor-Cell Lines In Vitro," *Electro- and Magnetobiology*, vol. 17, no. 2, pp. 263–272, jan 1998.

[125] B. E. Henslee, A. Morss, X. Hu, G. P. Lafyatis, and L. J. Lee, "Electroporation dependence on cell size: Optical tweezers study," *Analytical Chemistry*, vol. 83, no. 11, pp. 3998–4003, 2011.

[126] S. Hojo, K. Shimizu, H. Yositake, M. Muraji, H. Tsujimoto, and W. Tatebe, "The relationship between electropermeabilization and cell cycle and cell size of Saccharomyces cerevisiae," *IEEE Transactions on Nanobioscience*, vol. 2, no. 1, pp. 35–39, 2003.

[127] B. L. Ibey, C. C. Roth, A. G. Pakhomov, J. a. Bernhard, G. J.

Wilmink, and O. N. Pakhomova, "Dose-Dependent Thresholds of 10-ns Electric Pulse Induced Plasma Membrane Disruption and Cytotoxicity in Multiple Cell Lines," *PLoS ONE*, vol. 6, no. 1, p. e15642, jan 2011.

[128] L. Towhidi, T. Kotnik, G. Pucihar, S. M. P. Firoozabadi, H. Mozdarani, and D. Miklavčič, "Variability of the Minimal Transmembrane Voltage Resulting in Detectable Membrane Electroporation," *Electromagnetic Biology and Medicine*, vol. 27, no. 4, pp. 372–385, 2008.

[129] R. Benz and U. Zimmermann, "376 - Relaxation studies on cell membranes and lipid bilayers in the high electric field range," *Bioelectrochemistry and Bioenergetics*, vol. 7, no. 4, pp. 723–739, dec 1980.

[130] P. T. Vernier, M. J. Ziegler, Y. Sun, M. A. Gundersen, and D. P. Tieleman, "Nanopore-facilitated, voltage-driven phosphatidylserine translocation in lipid bilayers—in cells and in silico," *Physical Biology*, vol. 3, no. 4, pp. 233–247, nov 2006.

[131] M. Golzio, J. Teissié, and M.-P. Rols, "Cell synchronization effect on mammalian cell permeabilization and gene delivery by electric field," *Biochimica et Biophysica Acta (BBA) - Biomembranes*, vol. 1563, no. 1-2, pp. 23–28, 2002.

[132] A. Ivorra and B. Rubinsky, "In vivo electrical impedance measurements during and after electroporation of rat liver," *Bioelectrochemistry*, vol. 70, no. 2, pp. 287–295, 2007.

[133] M. Pavlin, M. Kandušer, M. Reberšek, G. Pucihar, F. X. Hart, R. Magjarevićcacute;, and D. Miklavčič, "Effect of Cell Electroporation on the Conductivity of a Cell Suspension," *Biophysical Journal*, vol. 88, no. 6, pp. 4378–4390, jun 2005.

[134] C. S. Djuzenova, V. L. Sukhorukov, G. Klöck, W. M. Arnold, and U. Zimmermann, "Effect of electric field pulses on the viability and on the membrane-bound immunoglobulins of LPS-activated murine B-lymphocytes: correlation with the cell cycle." *Cytometry*, vol. 15, no. 1, pp. 35–45, 1994.

[135] A. Ivorra, J. Villemejane, and L. M. Mir, "Electrical modeling of the influence of medium conductivity on electroporation," *Physical Chemistry Chemical Physics*, vol. 12, no. 34, pp. 10 055–10 064, 2010.

[136] K. A. DeBruin and W. Krassowska, "Modeling electroporation in a single cell. I. Effects Of field strength and rest potential." *Biophysical journal*, vol. 77, no. 3, pp. 1213–1224, 1999.

[137] K. Kinosita and T. Y. Tsong, "Voltage-induced conductance in human erythrocyte membranes," *Biochimica et Biophysica Acta (BBA) - Biomembranes*, vol. 554, no. 2, pp. 479–497, jul 1979.

[138] J. Gimsa, T. Müller, T. Schnelle, and G. Fuhr, "Dielectric spectroscopy of single human erythrocytes at physiological ionic strength: dispersion of the cytoplasm," *Biophysical Journal*, vol. 71, no. 1, pp. 495–506, jul 1996.

[139] J. Li and H. Lin, "The current-voltage relation for electropores with conductivity gradients," *Biomicrofluidics*, vol. 4, no. 1, pp. 1–17, 2010.

[140] L. Rems, M. Ušaj, M. Kandušer, M. Reberšek, D. Miklavčič, and G. Pucihar, "Cell electrofusion using nanosecond electric pulses," *Scientific Reports*, vol. 3, p. 3382, nov 2013.

[141] L. Retelj, G. Pucihar, and D. Miklavčič, "Electroporation of Intracellular Liposomes Using Nanosecond Electric Pulses&amp – A Theoretical Study," *IEEE Transactions on Biomedical Engineering*, vol. 60, no. 9, pp. 2624–2635, sep 2013.

[142] G. Pucihar, D. Miklavčič, and T. Kotnik, "A time-dependent numerical model of transmembrane voltage inducement and electroporation of irregularly shaped cells," *IEEE Transactions on Biomedical Engineering*, vol. 56, no. 5, pp. 1491–1501, 2009.

[143] W. Krassowska and P. D. Filev, "Modeling electroporation in a single cell." *Biophysical journal*, vol. 92, no. 2, pp. 404–417, 2007.

[144] T. Kotnik and D. Miklavčič, "Theoretical Evaluation of Voltage Inducement on Internal Membranes of Biological Cells Exposed to Electric Fields," *Biophysical Journal*, vol. 90, no. 2, pp. 480–491, jan 2006.

[145] R. Benz and U. Zimmermann, "The resealing process of lipid bilayers after reversible electrical breakdown," *Biochimica et Biophysica Acta (BBA) - Biomembranes*, vol. 640, no. 1, pp. 169–178, jan 1981.

[146] P. Lindner, E. Neumann, and K. Rosenheck, "Kinetics of permeability changes induced by electric impulses in chromaffin granules." *Journal of Membrane Biology*, vol. 32, no. 3-4, pp. 231–254, 1977.

[147] J. Teissié and T. Y. Tsong, "Electric field induced transient pores in phospholipid bilayer vesicles." *Biochemistry*, vol. 20, no. 6, pp. 1548–1554, 1981.

[148] M. Rols and J. Teissié, "Electropermeabilization of mammalian

cells. Quantitative analysis of the phenomenon," *Biophysical Journal*, vol. 58, no. 5, pp. 1089–1098, nov 1990.

[149] G. Saulis, M. Venslauskas, and J. Naktinis, "Kinetics of pore resealing in cell membranes after electroporation," *Journal of Electroanalytical Chemistry and Interfacial Electrochemistry*, vol. 321, no. 1, pp. 1–13, 1991.

[150] M. Hibino, M. Shigemori, H. Itoh, K. Nagayama, and K. Kinosita, "Membrane conductance of an electroporated cell analyzed by submicrosecond imaging of transmembrane potential." *Biophysical journal*, vol. 59, no. 1, pp. 209–220, 1991.

[151] P.-O. Gendron, F. Avaltroni, and K. J. Wilkinson, "Diffusion Coefficients of Several Rhodamine Derivatives as Determined by Pulsed Field Gradient–Nuclear Magnetic Resonance and Fluorescence Correlation Spectroscopy," *Journal of Fluorescence*, vol. 18, no. 6, pp. 1093–1101, 2008.

[152] Z. Petrášek and P. Schwille, "Precise Measurement of Diffusion Coefficients using Scanning Fluorescence Correlation Spectroscopy," *Biophysical Journal*, vol. 94, no. 4, pp. 1437–1448, 2008.

[153] E. M. Renkin, "Filtration, diffusion, and molecular sieving through porous cellulose membranes," *Journal of General Physiology*, vol. 38, no. 1, pp. 225–243, 1954.

[154] A. J. Jimenez, P. Maiuri, J. Lafaurie-Janvore, S. Divoux, M. Piel, and F. Perez, "ESCRT Machinery Is Required for Plasma Membrane Repair," *Science*, vol. 343, no. 6174, pp. 1 247 136–1 247 136, feb 2014.

[155] B. Gabriel and J. Teissié, "Time Courses of Mammalian Cell Electropermeabilization Observed by Millisecond Imaging of Membrane Property Changes during the Pulse," *Biophysical Journal*, vol. 76, no. 4, pp. 2158–2165, apr 1999.

[156] H. He, D. C. Chang, and Y. K. Lee, "Using a micro electroporation chip to determine the optimal physical parameters in the uptake of biomolecules in HeLa cells," *Bioelectrochemistry*, vol. 70, no. 2, pp. 363–368, 2007.

[157] B. Poddevin, S. Orlowski, J. Belehradek, and L. Mir, "Very high cytotoxicity of bleomycin introduced into the cytosol of cells in culture," *Biochemical Pharmacology*, vol. 42, pp. S67–S75, dec 1991.

[158] A. Silve and L. M. Mir, "Cell Electropermeabilization and Cellular Uptake of Small Molecules: The Electrochemotherapy Con-

cept," in *Clinical Aspects of Electroporation*, T. S. Kee, J. Gehl, and W. E. Lee, Eds. New York, NY: Springer New York, 2011, pp. 69–82.

[159] O. Tounekti, G. Pron, J. Belehradek, and L. M. Mir, "Bleomycin, an apoptosis-mimetic drug that induces two types of cell death depending on the number of molecules internalized." *Cancer research*, vol. 53, no. 22, pp. 5462–9, nov 1993.

[160] M. Leguèbe, A. Silve, L. Mir, and C. Poignard, "Conducting and permeable states of cell membrane submitted to high voltage pulses: Mathematical and numerical studies validated by the experiments," *Journal of Theoretical Biology*, vol. 360, pp. 83–94, nov 2014.

[161] R. Lindner, M. E. Sluijter, and W. Schleinzer, "Pulsed radiofrequency treatment of the lumbar medial branch for facet pain: A retrospective analysis," *Pain Medicine*, vol. 7, no. 5, pp. 435–439, 2006.

[162] J. Van Zundert, J. Patijn, A. Kessels, I. Lamé, H. van Suijlekom, and M. van Kleef, "Pulsed radiofrequency adjacent to the cervical dorsal root ganglion in chronic cervical radicular pain: A double blind sham controlled randomized clinical trial," *Pain*, vol. 127, no. 1-2, pp. 173–182, 2007.

[163] P. M. Schianchi, M. E. Sluijter, S. E. Balogh, and S. A. Clinic, "The Treatment of Joint Pain with Intra-articular Pulsed Radiofrequency," *Anesthesiology and Pain Medicine*, vol. 3, no. 2, pp. 250–5, 2013.

[164] T. Vanneste, A. Van Lantschoot, K. Van Boxem, and J. Van Zundert, "Pulsed radiofrequency in chronic pain," *Current Opinion in Anaesthesiology*, vol. 30, no. 5, pp. 577–582, oct 2017.

[165] M. Protasoni, M. Reguzzoni, S. Sangiorgi, C. Reverberi, E. Borsani, L. F. Rodella, A. Dario, G. Tomei, and C. Dell'Orbo, "Pulsed radiofrequency effects on the lumbar ganglion of the rat dorsal root: a morphological light and transmission electron microscopy study at acute stage," *European Spine Journal*, vol. 18, no. 4, pp. 473–478, apr 2009.

[166] T. T. Simopoulos, J. Kraemer, J. V. Nagda, M. Aner, and Z. H. Bajwa, "Response to pulsed and continuous radiofrequency lesioning of the dorsal root ganglion and segmental nerves in patients with chronic lumbar radicular pain." *Pain Physician*, vol. 11, no. 2, pp. 137–144, 2008.

[167] K. Tun, B. Cemil, A. G. Gurcay, E. Kaptanoglu, M. F. Sargon, I. Tekdemir, A. Comert, and Y. Kanpolat, "Ultrastructural evaluation of pulsed radiofrequency and conventional radiofrequency lesions in rat sciatic nerve," *Surgical Neurology*, vol. 72, no. 5, pp. 496–500, nov 2009.

[168] D. Vatansever, I. Tekin, I. Tuglu, K. Erbuyun, and G. Ok, "A Comparison of the Neuroablative Effects of Conventional and Pulsed Radiofrequency Techniques," *The Clinical Journal of Pain*, vol. 24, no. 8, pp. 717–724, oct 2008.

[169] A. Cahana, J. Van Zundert, L. Macrea, M. Van Kleef, and M. Sluijter, "Pulsed Radiofrequency: Current Clinical and Biological Literature Available," *Pain Medicine*, vol. 7, no. 5, pp. 411–423, sep 2006.

[170] N. H. L. Chua, K. C. Vissers, and M. E. Sluijter, "Pulsed radiofrequency treatment in interventional pain management: Mechanisms and potential indications - A review," *Acta Neurochirurgica*, vol. 153, no. 4, pp. 763–771, 2011.

[171] J. Hata, D. Perret-Karimi, C. DeSilva, D. Leung, N. Betesh, Z. D. Luo, S. Dawodu, K. Sinavsky, O. J. Stokes, and S. English, "Pulsed Radiofrequency Current in the Treatment of Pain," *Critical Reviews in Physical and Rehabilitation Medicine*, vol. 23, no. 1-4, pp. 213–240, 2011.

[172] S. Choi, H. J. Choi, Y. Cheong, Y. J. Lim, and H. K. Park, "Internal-Specific Morphological Analysis of Sciatic Nerve Fibers in a Radiofrequency-Induced Animal Neuropathic Pain Model," *PLoS ONE*, vol. 8, no. 9, 2013.

[173] S. Choi, H. Choi, Y. Cheong, S. Chung, H. Park, and Y. Lim, "Inflammatory responses and morphological changes of radiofrequency-induced rat sciatic nerve fibres," *European Journal of Pain*, vol. 18, no. 2, pp. 192–203, feb 2014.

[174] S. Erdine, A. Bilir, E. R. Cosman, and E. R. Cosman Jr., "Ultrastructural Changes in Axons Following Exposure to Pulsed Radiofrequency Fields," *Pain Practice*, vol. 9, no. 6, pp. 407–417, nov 2009.

[175] J. Van Zundert, A. J. a. de Louw, E. a. J. Joosten, A. G. H. Kessels, W. Honig, P. J. W. C. Dederen, J. G. Veening, J. S. H. Vles, and M. van Kleef, "Pulsed and Continous Radiofrequency Current Adjacent to the Cervical Dorsal Root Ganglion of the Rat Induces Late Cellular Activity in the Dorsal Horn," *Anesthesiology*, vol. 102, no. 1, pp. 125–131, jan 2005.

[176] W. Hamann, S. Abou-Sherif, S. Thompson, and S. Hall, "Pulsed radiofrequency applied to dorsal root ganglia causes a selective increase in ATF3 in small neurons," *European Journal of Pain*, vol. 10, no. 2, pp. 171–176, 2006.

[177] Z. Jia, H. Ren, Q. Li, N. Ji, and F. Luo, "Pulsed radiofrequency reduced neuropathic pain behavior in rats associated with up-regulation of GDNF expression," *Pain Physician*, vol. 19, no. 2, pp. 49–58, 2016.

[178] Y. Liu, Y. Feng, and T. Zhang, "Pulsed Radiofrequency Treatment Enhances Dorsal Root Ganglion Expression of Hyperpolarization-Activated Cyclic Nucleotide-Gated Channels in a Rat Model of Neuropathic Pain," *Journal of Molecular Neuroscience*, vol. 57, no. 1, pp. 97–105, 2015.

[179] R. Vallejo, D. M. Tilley, J. Williams, S. Labak, L. Aliaga, and R. M. Benyamin, "Pulsed radiofrequency modulates pain regulatory gene expression along the nociceptive pathway." *Pain physician*, vol. 16, no. 5, pp. E601–13, 2013.

[180] C. C. Yeh, H. L. Sun, C. J. Huang, C. S. Wong, C. H. Cherng, B. K. Huh, J. S. Wang, and C. C. Chien, "Long-term anti-allodynic effect of immediate pulsed radiofrequency modulation through down-regulation of insulin-like growth factor 2 in a neuropathic pain model," *International Journal of Molecular Sciences*, vol. 16, no. 11, pp. 27 156–27 170, 2015.

[181] R.-Y. Huang, C.-C. Liao, S.-Y. Tsai, C.-T. Yen, C.-W. Lin, T.-C. Chen, W.-T. Lin, C.-H. Chang, and Y.-R. Wen, "Rapid and Delayed Effects of Pulsed Radiofrequency on Neuropathic Pain: Electrophysiological, Molecular, and Behavioral Evidence Supporting Long-Term Depression." *Pain physician*, vol. 20, no. 2, pp. E269–E283, 2017.

[182] E. Ewertowska, B. Mercadal, V. Muñoz, A. Ivorra, M. Trujillo, and E. Berjano, "Effect of applied voltage, duration and repetition frequency of RF pulses for pain relief on temperature spikes and electrical field: a computer modelling study," *International Journal of Hyperthermia*, vol. 6736, no. October, pp. 1–10, may 2017.

[183] E. R. Cosman and E. R. Cosman, "Electric and Thermal Field Effects in Tissue Around Radiofrequency Electrodes," *Pain Medicine*, vol. 6, no. 6, pp. 405–424, nov 2005.

[184] J. Schindelin, I. Arganda-Carreras, E. Frise, V. Kaynig, M. Longair, T. Pietzsch, S. Preibisch, C. Rueden, S. Saalfeld,

B. Schmid, J.-Y. J.-Y. Tinevez, D. J. White, V. Hartenstein, K. Eliceiri, P. Tomancak, A. Cardona, K. Liceiri, P. Tomancak, and C. A., "Fiji: An open source platform for biological image analysis." *Nature Methods*, vol. 9, no. 7, pp. 676–682, 2012.

[185] C. A. Schneider, W. S. Rasband, and K. W. Eliceiri, "NIH Image to ImageJ: 25 years of image analysis." *Nature methods*, vol. 9, no. 7, pp. 671–5, 2012.

[186] R Core Team, *R: A Language and Environment for Statistical Computing*, R Foundation for Statistical Computing, Vienna, Austria, 2014.

[187] R. Kubin and A. Fletcher, "Fluorescence quantum yields of some rhodamine dyes," *Journal of Luminescence*, vol. 27, no. 4, pp. 455–462, dec 1982.

[188] J. J. Shah, M. Gaitan, and J. Geist, "Generalized temperature measurement equations for rhodamine B dye solution and its application to microfluidics," *Analytical Chemistry*, vol. 81, no. 19, pp. 8260–8263, 2009.

[189] B. Schmid, J. Schindelin, A. Cardona, M. Longair, and M. Heisenberg, "A high-level 3D visualization API for Java and ImageJ," *BMC Bioinformatics*, vol. 11, no. 1, p. 274, 2010.

[190] J. Wells, C. Kao, P. Konrad, T. Milner, J. Kim, A. Mahadevan-Jansen, and E. D. Jansen, "Biophysical mechanisms of transient optical stimulation of peripheral nerve," *Biophysical Journal*, vol. 93, no. 7, pp. 2567–2580, 2007.

[191] H. T. Beier, G. P. Tolstykh, J. D. Musick, R. J. Thomas, and B. L. Ibey, "Plasma membrane nanoporation as a possible mechanism behind infrared excitation of cells," *Journal of Neural Engineering*, vol. 11, no. 6, 2014.

[192] S. Berjukow, F. Döring, M. Froschmayr, M. Grabner, H. Glossmann, and S. Hering, "Endogenous calcium channels in human embryonic kidney (HEK293) cells." *British journal of pharmacology*, vol. 118, no. 3, pp. 748–754, 1996.

[193] M. Shimazawa, H. Hara, T. Watano, and T. Sukamoto, "Effects of Ca2+ channel blockers on cortical hypoperfusion and expression of c-Fos-like immunoreactivity after cortical spreading depression in rats," *British Journal of Pharmacology*, vol. 115, no. 8, pp. 1359–1368, aug 1995.

[194] X. Tao, S. Finkbeiner, D. B. Arnold, A. J. Shaywitz, and M. E. Greenberg, "Ca2+ influx regulates BDNF transcription by a CREB family transcription factor-dependent mechanism," *Neu-*

*ron*, vol. 20, no. 4, pp. 709–726, 1998.

[195] S.-J. Zhang, M. Zou, L. Lu, D. Lau, D. A. W. Ditzel, C. Delucinge-Vivier, Y. Aso, P. Descombes, and H. Bading, "Nuclear Calcium Signaling Controls Expression of a Large Gene Pool: Identification of a Gene Program for Acquired Neuroprotection Induced by Synaptic Activity," *PLoS Genetics*, vol. 5, no. 8, p. e1000604, aug 2009.

[196] W. W. Schlaepfer and M. B. Hasler, "Characterization of the calcium-induced disruption of neurofilaments in rat peripheral nerve," *Brain Research*, vol. 168, no. 2, pp. 299–309, 1979.

[197] S. Deheshi, B. Dabiri, S. Fan, M. Tsang, and G. L. Rintoul, "Changes in mitochondrial morphology induced by calcium or rotenone in primary astrocytes occur predominantly through ros-mediated remodeling," *Journal of Neurochemistry*, vol. 133, no. 5, pp. 684–699, jun 2015.

[198] A. Cahana, L. Vutskits, and D. Muller, "Acute differential modulation of synaptic transmission and cell survival during exposure to pulsed and continuous radiofrequency energy," *The Journal of Pain*, vol. 4, no. 4, pp. 197–202, may 2003.

[199] G. Saulis and R. Saule, "Size of the pores created by an electric pulse: Microsecond vs millisecond pulses," *Biochimica et Biophysica Acta - Biomembranes*, vol. 1818, no. 12, pp. 3032–3039, 2012.

[200] T. Batista Napotnik, M. Reberšek, P. T. Vernier, B. Mali, and D. Miklavčič, "Effects of high voltage nanosecond electric pulses on eucaryotic cells (in vitro): A systematic review," *Bioelectrochemistry*, vol. 110, pp. 1–12, 2016.

[201] L. Fang, W. Tao, L. Jingjing, and J. Nan, "Comparison of High-voltage- with Standard-voltage Pulsed Radiofrequency of Gasserian Ganglion in the Treatment of Idiopathic Trigeminal Neuralgia," *Pain Practice*, vol. 15, no. 7, pp. 595–603, sep 2015.

[202] M. B. Sano, C. B. Arena, M. R. DeWitt, D. Saur, and R. V. Davalos, "In-vitro bipolar nano- and microsecond electro-pulse bursts for irreversible electroporation therapies," *Bioelectrochemistry*, vol. 100, pp. 69–79, dec 2014.

[203] M. B. Sano, C. B. Arena, K. R. Bittleman, M. R. DeWitt, H. J. Cho, C. S. Szot, D. Saur, J. M. Cissell, J. Robertson, Y. W. Lee, and R. V. Davalos, "Bursts of Bipolar Microsecond Pulses Inhibit Tumor Growth," *Scientific Reports*, vol. 5, p. 14999, 2015.

[204] D. C. Sweeney, M. Reberšek, J. Dermol, L. Rems, D. Miklavčič, and R. V. Davalos, "Quantification of cell membrane permeability induced by monopolar and high-frequency bipolar bursts of electrical pulses," *Biochimica et Biophysica Acta (BBA) - Biomembranes*, vol. 1858, no. 11, pp. 2689–2698, nov 2016.

[205] J. P. Reilly, "Electrical Models for Neural Excitation Studies," *John Hopkins APL Technical Digest*, vol. 9, no. 1, pp. 44–59, 1988.

[206] C. C. McIntyre, A. G. Richardson, and W. M. Grill, "Modeling the excitability of mammalian nerve fibers: influence of afterpotentials on the recovery cycle." *Journal of neurophysiology*, vol. 87, no. 2, pp. 995–1006, feb 2002.

[207] K. W. Altman and R. Plonsey, "Analysis of excitable cell activation: relative effects of external electrical stimuli," *Medical & Biological Engineering & Computing*, vol. 28, no. 6, pp. 574–580, nov 1990.

[208] J. P. Reilly and R. H. Bauer, "Application of a Neuroelectric Model to Electrocutaneous Sensory Sensitivity: Parameter Variation Study," *IEEE Transactions on Biomedical Engineering*, vol. BME-34, no. 9, pp. 752–754, sep 1987.

[209] J. N. Barrett and W. E. Crill, "Specific membrane properties of cat motoneurones," *The Journal of Physiology*, vol. 239, no. 2, pp. 301–324, jun 1974.

[210] C. H. Berthold and M. Rydmark, "Electron microscopic serial section analysis of nodes of Ranvier in lumbosacral spinal roots of the cat: ultrastructural organization of nodal compartments in fibres of different sizes," *Journal of Neurocytology*, vol. 12, no. 3, pp. 475–505, jun 1983.

[211] I. Nilsson and C. H. Berthold, "Axon classes and internodal growth in the ventral spinal root L7 of adult and developing cats." *Journal of anatomy*, vol. 156, no. 2, pp. 71–96, feb 1988.

[212] M. Rydmark, "Nodal axon diameter correlates linearly with internodal axon diameter in spinal roots of the cat," *Neuroscience Letters*, vol. 24, no. 3, pp. 247–250, jul 1981.

[213] F. Rattay, "Analysis of Models for External Stimulation of Axons," *IEEE Transactions on Biomedical Engineering*, vol. BME-33, no. 10, pp. 974–977, 1986.

[214] J. P. Reilly, "Survey of numerical electrostimulation models," *Physics in Medicine and Biology*, vol. 61, no. 12, pp. 4346–4363, jun 2016.

[215] J. P. Reilly, V. T. Freeman, and W. D. Larkin, "Sensory effects of transient electrical stimulation–evaluation with a neuroelectric model." *IEEE transactions on bio-medical engineering*, vol. 32, no. 12, pp. 1001–1011, 1985.

[216] D. Boinagrov, J. Loudin, and D. Palanker, "Strength-Duration Relationship for Extracellular Neural Stimulation: Numerical and Analytical Models," *Journal of Neurophysiology*, vol. 104, no. 4, pp. 2236–2248, oct 2010.

[217] D. Dean and P. D. Lawrence, "Optimization of Neural Stimuli Based Upon a Variable Threshold Potential," *IEEE Transactions on Biomedical Engineering*, vol. BME-32, no. 1, pp. 8–14, jan 1985.

[218] M. B. Sano, R. E. Fan, and L. Xing, "Asymmetric Waveforms Decrease Lethal Thresholds in High Frequency Irreversible Electroporation Therapies," *Scientific Reports*, vol. 7, no. May 2016, p. 40747, jan 2017.

[219] B. L. Ibey, J. C. Ullery, O. N. Pakhomova, C. C. Roth, I. Semenov, H. T. Beier, M. Tarango, S. Xiao, K. H. Schoenbach, and A. G. Pakhomov, "Bipolar nanosecond electric pulses are less efficient at electropermeabilization and killing cells than monopolar pulses," *Biochemical and Biophysical Research Communications*, vol. 443, no. 2, pp. 568–573, jan 2014.

[220] S. Corovic, I. Lackovic, P. Sustaric, T. Sustar, T. Rodic, and D. Miklavčič, "Modeling of electric field distribution in tissues during electroporation," *BioMedical Engineering OnLine*, vol. 12, no. 1, p. 16, 2013.

[221] S. P. Bhonsle, C. B. Arena, D. C. Sweeney, and R. V. Davalos, "Mitigation of impedance changes due to electroporation therapy using bursts of high-frequency bipolar pulses." *Biomedical engineering online*, vol. 14 Suppl 3, no. Suppl 3, p. S3, 2015.

[222] H. Meffin, B. Tahayori, D. B. Grayden, and A. N. Burkitt, "Modeling extracellular electrical stimulation: I. Derivation and interpretation of neurite equations." *Journal of neural engineering*, vol. 9, no. 6, p. 065005, 2012.

[223] T. Kotnik and D. Miklavčič, "Second-order model of membrane electric field induced by alternating external electric fields." *IEEE Transactions on Biomedical Engineering*, vol. 47, no. 8, pp. 1074–1081, 2000.

[224] M. S. Cooper, "Membrane potential perturbations induced in tissue cells by pulsed electric fields," *Bioelectromagnetics*,

vol. 16, no. 4, pp. 255–262, 1995.

[225] J. C. Weaver, K. C. Smith, A. T. Esser, R. S. Son, and T. R. Gowrishankar, "Bioelectrochemistry A brief overview of electroporation pulse strength – duration space : A region where additional intracellular effects are expected," *Bioelectrochemistry*, vol. 87, pp. 236–243, 2012.

[226] C. B. Arena, C. S. Szot, P. A. Garcia, M. N. Rylander, and R. V. Davalos, "A three-dimensional in vitro tumor platform for modeling therapeutic irreversible electroporation," *Biophysical Journal*, vol. 103, no. 9, pp. 2033–2042, 2012.

[227] J. W. Ivey, E. L. Latouche, M. L. Richards, G. J. Lesser, W. Debinski, R. V. Davalos, and S. S. Verbridge, "Enhancing Irreversible Electroporation by Manipulating Cellular Biophysics with a Molecular Adjuvant," *Biophysical Journal*, vol. 113, no. 2, pp. 472–480, jul 2017.

[228] E. M. Wasson, J. W. Ivey, S. S. Verbridge, and R. V. Davalos, "The Feasibility of Enhancing Susceptibility of Glioblastoma Cells to IRE Using a Calcium Adjuvant," *Annals of Biomedical Engineering*, vol. 45, no. 11, pp. 2535–2547, nov 2017.

[229] C. S. Szot, C. F. Buchanan, J. W. Freeman, and M. N. Rylander, "3D in vitro bioengineered tumors based on collagen I hydrogels," *Biomaterials*, vol. 32, no. 31, pp. 7905–7912, nov 2011.

[230] Q. Qin, Z. A. Xiong, Y. Liu, C. G. Yao, W. Zhou, Y. Y. Hua, and Z. L. Wang, "Effects of irreversible electroporation on cervical cancer cell lines in vitro," *Molecular Medicine Reports*, vol. 14, no. 3, pp. 2187–2193, 2016.

[231] O. N. Pakhomova, B. W. Gregory, and A. G. Pakhomov, "Facilitation of electroporative drug uptake and cell killing by electrosensitization," *Journal of Cellular and Molecular Medicine*, vol. 17, no. 1, pp. 154–159, 2013.

[232] T. Idziorek, J. Estaquier, F. De Bels, and J.-C. Ameisen, "YOPRO-1 permits cytofluorometric analysis of programmed cell death (apoptosis) without interfering with cell viability," *Journal of Immunological Methods*, vol. 185, no. 2, pp. 249–258, jan 1995.

[233] T. B. Napotnik, "Fluorescent Indicators of Membrane Permeabilization Due to Electroporation," in *Handbook of Electroporation*. Cham: Springer International Publishing, 2017, vol. 1-4, pp. 1305–1323.

[234] R. V. Davalos, S. Bhonsle, and R. E. Neal, "Implications and considerations of thermal effects when applying irreversible electroporation tissue ablation therapy," *The Prostate*, vol. 75, no. 10, pp. 1114–1118, jul 2015.

[235] J. A. Vogel, E. Van Veldhuisen, P. Agnass, J. Crezee, F. Dijk, J. Verheij, T. M. Van Gulik, M. R. Meijerink, L. G. Vroomen, K. P. Van Lienden, and M. G. Besselink, "Time-dependent impact of irreversible electroporation on pancreas, liver, blood vessels and nerves: A systematic review of experimental studies," *PLoS ONE*, vol. 11, no. 11, pp. 1–18, 2016.

[236] W. Chai, W. Zhang, Z. Wei, Y. Xu, J. Shi, X. Luo, J. Zeng, M. Cui, J. Li, and L. Niu, "Irreversible electroporation of the uterine cervix in a rabbit model," *Biomedical Microdevices*, vol. 19, no. 4, p. 103, dec 2017.

[237] H. B. Kim, C. K. Sung, K. Y. Baik, K. W. Moon, H. S. Kim, J. H. Yi, J. H. Jung, M. H. Moon, and O. K. Choi, "Changes of apoptosis in tumor tissues with time after irreversible electroporation," *Biochemical and Biophysical Research Communications*, vol. 435, no. 4, pp. 651–656, 2013.

[238] E. W. Lee, C. T. Loh, and S. T. Kee, "Imaging Guided Percutaneous Irreversible Electroporation: Ultrasound and Immunohistological Correlation," *Technology in Cancer Research & Treatment*, vol. 6, no. 4, pp. 287–293, aug 2007.

[239] W. Zhang, W. Chai, J. Zeng, J. Chen, L. Bi, and L. Niu, "Irreversible electroporation for the treatment of rabbit VX2 breast cancer," *Biomedical Microdevices*, vol. 19, no. 2, p. 29, jun 2017.

[240] Z. Zhang, W. Li, D. Procissi, P. Tyler, R. A. Omary, and A. C. Larson, "Rapid dramatic alterations to the tumor microstructure in pancreatic cancer following irreversible electroporation ablation," *Nanomedicine*, vol. 9, no. 8, pp. 1181–1192, jun 2014.

[241] Y. Fuchs and H. Steller, "Live to die another way: modes of programmed cell death and the signals emanating from dying cells." *Nature reviews. Molecular cell biology*, vol. 16, no. 6, pp. 329–44, jun 2015.

[242] L. Galluzzi, I. Vitale, S. A. Aaronson, J. M. Abrams, D. Adam, P. Agostinis, ..., and G. Kroemer, "Molecular mechanisms of cell death: recommendations of the Nomenclature Committee on Cell Death 2018." *Cell death and differentiation*, vol. 25, no. 3, pp. 486–541, 2018.

[243] B. López-Alonso, A. Hernáez, H. Sarnago, A. Naval, A. Güemes,

C. Junquera, J. M. Burdío, T. Castiella, E. Monleón, J. Gracia-Llanes, F. Burdio, E. Mejía, and O. Lucía, "Histopathological and Ultrastructural Changes after Electroporation in Pig Liver Using Parallel-Plate Electrodes and High-Performance Generator," *Scientific Reports*, vol. 9, no. 1, p. 2647, dec 2019.

[244] Y. Zhang, C. Lyu, Y. Liu, Y. Lv, T. T. Chang, and B. Rubinsky, "Molecular and histological study on the effects of non-thermal irreversible electroporation on the liver," *Biochemical and Biophysical Research Communications*, vol. 500, no. 3, pp. 665–670, 2018.

[245] S. Beebe, P. Fox, L. Rec, K. Somers, R. Stark, and K. Schoenbach, "Nanosecond pulsed electric field (nsPEF) effects on cells and tissues: apoptosis induction and tumor growth inhibition," *IEEE Transactions on Plasma Science*, vol. 30, no. 1, pp. 286–292, feb 2002.

[246] W. E. Ford, W. Ren, P. F. Blackmore, K. H. Schoenbach, and S. J. Beebe, "Nanosecond pulsed electric fields stimulate apoptosis without release of pro-apoptotic factors from mitochondria in B16f10 melanoma," *Archives of Biochemistry and Biophysics*, vol. 497, no. 1-2, pp. 82–89, may 2010.

[247] T. B. Napotnik, Y.-H. Wu, M. A. Gundersen, D. Miklavčič, and P. T. Vernier, "Nanosecond electric pulses cause mitochondrial membrane permeabilization in Jurkat cells," *Bioelectromagnetics*, vol. 33, no. 3, pp. 257–264, apr 2012.

[248] A. Pakhomov, A. Phinney, J. Ashmore, K. Walker, J. Kolb, S. Kono, K. Schoenbach, and M. Murphy, "Characterization of the Cytotoxic Effect of High-Intensity, 10-ns Duration Electrical Pulses," *IEEE Transactions on Plasma Science*, vol. 32, no. 4, pp. 1579–1586, aug 2004.

[249] W. Ren, N. M. Sain, and S. J. Beebe, "Nanosecond pulsed electric fields (nsPEFs) activate intrinsic caspase-dependent and caspase-independent cell death in Jurkat cells," *Biochemical and Biophysical Research Communications*, vol. 421, no. 4, pp. 808–812, may 2012.

[250] S. J. Beebe, "Regulated and Apoptotic Cell Death After Nanosecond Electroporation," in *Handbook of Electroporation*, D. Miklavčič, Ed. Cham: Springer International Publishing, 2017, vol. 1-4, pp. 511–528.

[251] L. W. Chou, J. Ding, A. S. Wexler, and S. A. Binder-Macleod, "Predicting optimal electrical stimulation for repetitive human

muscle activation," *Journal of Electromyography and Kinesiology*, vol. 15, no. 3, pp. 300–309, 2005.

[252] J. Ding, S. C. K. Lee, T. E. Johnston, A. S. Wexler, W. B. Scott, and S. A. Binder-Macleod, "Mathematical model that predicts isometric muscle forces for individuals with spinal cord injuries," *Muscle and Nerve*, vol. 31, no. 6, pp. 702–712, 2005.

[253] A. J. Fuglevand, D. A. Winter, and A. E. Patla, "Models of Recruitment and Rate Coding Organization in Motor-Unit Pools." *Journal of Neurophysiology*, vol. 70, no. 6, pp. 2470–2488, 1993.

[254] J. Z. Liu, R. W. Brown, and G. H. Yue, "A Dynamical Model of Muscle Activation, Fatigue, and Recovery," *Biophysical Journal*, vol. 82, no. 5, pp. 2344–2359, may 2002.

[255] J. R. Potvin and A. J. Fuglevand, "A motor unit-based model of muscle fatigue," *PLOS Computational Biology*, vol. 13, no. 6, p. e1005581, jun 2017.

[256] R. P. Joshi, F. Chen, and W. R. Rogers, "Modeling electrode-based stimulation of muscle and nerve by ultrashort electric pulses," *IEEE Transactions on Plasma Science*, vol. 32, no. 4 II, pp. 1687–1695, 2004.

[257] R. P. Joshi and J. Song, "Model analysis of electric fields induced by high-voltage pulsing in cylindrical nerves," *IEEE Transactions on Plasma Science*, vol. 38, no. 10 PART 2, pp. 2894–2900, 2010.

[258] J. H. Kim, J. B. Davidson, O. Röhrle, T. K. Soboleva, and A. J. Pullan, "Anatomically based lower limb nerve model for electrical stimulation," *BioMedical Engineering Online*, vol. 6, pp. 1–11, 2007.

[259] A. Kuhn, T. Keller, M. Lawrence, and M. Morari, "A model for transcutaneous current stimulation: simulations and experiments," *Medical & Biological Engineering & Computing*, vol. 47, no. 3, pp. 279–289, mar 2009.

[260] T. Peker, N. Gülekon, B. H. Turgut, A. Anil, M. Karaköse, T. Mungan, and N. Danişman, "Observation of the Relationship between the Shape of Skeletal Muscles and Their Nerve Distribution Patterns: A Transparent and Microanatomic Study," *Plastic and Reconstructive Surgery*, vol. 117, no. 1, pp. 165–176, jan 2006.

[261] A. Van Campenhout and G. Molenaers, "Localization of the motor endplate zone in human skeletal muscles of the lower limb: anatomical guidelines for injection with botulinum toxin,"

*Developmental Medicine & Child Neurology*, vol. 53, no. 2, pp. 108–119, feb 2011.

[262] S.-M. Aquilonius, H. Askmark, P.-G. Gillberg, S. Nandedkar, Y. Olsson, and E. Stårlberg, "Topographical localization of motor endplates in cryosections of whole human muscles," *Muscle & Nerve*, vol. 7, no. 4, pp. 287–293, may 1984.

[263] X. Zhang, L. Mu, H. Su, and S. Sobotka, "Locations of the Motor Endplate Band and Motoneurons Innervating the Sternomastoid Muscle in the Rat," *The Anatomical Record: Advances in Integrative Anatomy and Evolutionary Biology*, vol. 294, no. 2, pp. 295–304, feb 2011.

[264] X. Yin, T. Yu, B. Chen, J. Xu, W. Chen, Y. Qi, P. Zhang, Y. Li, Y. Kou, Y. Ma, N. Han, P. Wan, Q. Luo, D. Zhu, and B. Jiang, "Spatial Distribution of Motor Endplates and its Adaptive Change in Skeletal Muscle," *Theranostics*, vol. 9, no. 3, pp. 734–746, 2019.

[265] J. Liu, V. P. Kumar, Y. Shen, H. K. Lau, B. P. Pereira, and R. W. Pho, "Modified Sihler's technique for studying the distribution of intramuscular nerve branches in mammalian skeletal muscle," *Anatomical Record*, vol. 247, no. 1, pp. 137–144, jan 1997.

[266] E. Y. Loh, A. M. Agur, and N. H. Mckee, "Intramuscular Innervation of the Human Soleus Muscle : A 3D Model," *Clinical Anatomy*, vol. 382, no. February, pp. 378–382, 2003.

[267] S. Sekiya, "Muscle Architecture and Intramuscular Distribution of Nerves in the Human Soleus Muscle," *Cells Tissues Organs*, vol. 140, no. 3, pp. 213–223, 1991.

[268] J. Lu, J. C. Tapia, O. L. White, and J. W. Lichtman, "The Interscutularis Muscle Connectome," *PLOS Biology*, vol. 7, no. 2, p. e1000032, feb 2009.

[269] J. C. Tapia, J. D. Wylie, N. Kasthuri, K. J. Hayworth, R. Schalek, D. R. Berger, C. Guatimosim, H. S. Seung, and J. W. Lichtman, "Pervasive Synaptic Branch Removal in the Mammalian Neuromuscular System at Birth," *Neuron*, vol. 74, no. 5, pp. 816–829, jun 2012.

[270] E. Christensen, "Topography of terminal motor innervation in striated muscles from stillborn infants." *American journal of physical medicine*, vol. 38, no. 2, pp. 65–78, apr 1959.

[271] S. Deshpande, M. E. Gormley, and J. R. Carey, "Muscle fiber orientation in muscles commonly injected with botulinum toxin:

An anatomical pilot study," *Neurotoxicity Research*, vol. 9, no. 2-3, pp. 115–120, 2006.

[272] C. Coërs, "Structural organization of the motor nerve endings in mammalian muscle spindles and other striated muscle fibers." *American journal of physical medicine*, vol. 38, pp. 166–75, aug 1959.

[273] H. Vogel, "A better way to construct the sunflower head," *Mathematical Biosciences*, vol. 44, no. 3-4, pp. 179–189, jun 1979.

[274] J. W. Fleshman, J. B. Munson, G. W. Sypert, and W. A. Friedman, "Rheobase, input resistance, and motor-unit type in medial gastrocnemius motoneurons in the cat," *Journal of Neurophysiology*, vol. 46, no. 6, pp. 1326–1338, dec 1981.

[275] R. E. Burke and P. Tsairis, "Anatomy and innervation ratios in motor units of cat gastrocnemius," *The Journal of Physiology*, vol. 234, no. 3, pp. 749–765, nov 1973.

[276] W. Feindel, J. R. Hinshaw, and G. Weddell, "The pattern of motor innervation in mammalian striated muscle." *Journal of anatomy*, vol. 86, no. 1, pp. 35–48, 1952.

[277] W. Feindel, "Anatomical overlap of motor-units." *The Journal of comparative neurology*, vol. 101, no. 1, pp. 1–17, aug 1954.

[278] A. English and O. Weeks, "Compartmentalization of single muscle units in cat lateral gastrocnemius," *Experimental Brain Research*, vol. 56, no. 2, pp. 361–368, sep 1984.

[279] E. Smits, P. K. Rose, T. Gordon, and F. J. Richmond, "Organization of single motor units in feline sartorius," *Journal of Neurophysiology*, vol. 72, no. 4, pp. 1885–1896, oct 1994.

[280] M. Ounjian, R. R. Roy, E. Eldred, A. Garfinkel, J. R. Payne, A. Armstrong, A. W. Toga, and V. R. Edgerton, "Physiological and developmental implications of motor unit anatomy," *Journal of Neurobiology*, vol. 22, no. 5, pp. 547–559, jul 1991.

[281] S. Knott, D. Lewis, and J. Luck, "Motor unit areas in a cat limb muscle," *Experimental Neurology*, vol. 30, no. 3, pp. 475–483, mar 1971.

[282] A. W. English and W. D. Letbetter, "Anatomy and innervation patterns of cat lateral gastrocnemius and plantaris muscles," *American Journal of Anatomy*, vol. 164, no. 1, pp. 67–77, 1982.

[283] O. I. Weeks and A. W. English, "Cat triceps surae motor nuclei are organized topologically," *Experimental Neurology*, vol. 96, no. 1, pp. 163–177, apr 1987.

[284] B. Thomson, S. H. Scott, and F. J. Richmond, "Neuromuscular organization of feline anterior sartorius: I. Asymmetric distribution of motor units," *Journal of Morphology*, vol. 210, no. 2, pp. 147–162, 1991.

[285] D. C. Gordon, G. E. Loeb, and F. J. R. Richmond, "Distribution of motoneurons supplying cat sartorius and tensor fasciae latae, demonstrated by retrograde multiple-labelling methods," *The Journal of Comparative Neurology*, vol. 304, no. 3, pp. 357–372, feb 1991.

[286] C. G. Hammond, D. C. Gordon, J. T. Fisher, and F. J. Richmond, "Motor unit territories supplied by primary branches of the phrenic nerve," *Journal of Applied Physiology*, vol. 66, no. 1, pp. 61–71, jan 1989.

[287] J. C. Eccles and C. S. Sherrington, "Numbers and Contraction-Values of Individual Motor-Units Examined in some Muscles of the Limb," *Proceedings of the Royal Society B: Biological Sciences*, vol. 106, no. 745, pp. 326–357, jun 1930.

[288] S. Sunderland and J. O. Lavarack, "The branching of nerve fibers," *Acta anatomica*, vol. 17, no. 1, pp. 46–61, 1953.

[289] S. H. Wray, "Innervation ratios for large and small limb muscles in the baboon," *Journal of Comparative Neurology*, vol. 137, no. 2, pp. 227–250, 1969.

[290] S. Gabriel, R. W. Lau, and C. Gabriel, "The dielectric properties of biological tissues: III. Parametric models for the dielectric spectrum of tissues," *Physics in Medicine and Biology*, vol. 41, no. 11, pp. 2271–2293, nov 1996.

[291] E. J. Perreault, S. J. Day, M. Hulliger, C. J. Heckman, and T. G. Sandercock, "Summation of Forces From Multiple Motor Units in the Cat Soleus Muscle," *Journal of Neurophysiology*, vol. 89, no. 2, pp. 738–744, feb 2003.

[292] S. Ugrenović, I. Jovanović, L. Vasović, B. Kundalić, R. Čukuranović, and V. Stefanović, "Morphometric analysis of the diameter and g-ratio of the myelinated nerve fibers of the human sciatic nerve during the aging process," *Anatomical Science International*, vol. 91, no. 3, pp. 238–245, 2016.

[293] T. C. Hirst and R. R. Ribchester, "Segmentation of the mouse fourth deep lumbrical muscle connectome reveals concentric organisation of motor units," *The Journal of Physiology*, vol. 591, no. 19, pp. 4859–4875, oct 2013.

[294] A. J. Buckmire, D. R. Lockwood, C. J. Doane, and A. J. Fu-

glevand, "Distributed stimulation increases force elicited with functional electrical stimulation," *Journal of Neural Engineering*, vol. 15, no. 2, p. 026001, apr 2018.

[295] A. J. Buckmire, T. J. Arakeri, J. P. Reinhard, and A. J. Fuglevand, "Mitigation of excessive fatigue associated with functional electrical stimulation," *Journal of Neural Engineering*, vol. 15, no. 6, p. 066004, dec 2018.

[296] T. Cameron, F. J. R. Richmond, and G. E. Loeb, "Effects of Regional Stimulation Using a Miniature Stimulator Implanted in Feline Posterior Biceps Femoris," *IEEE Transactions on Biomedical Engineering*, vol. 45, no. 8, pp. 1036–1043, 1998.

[297] D. Popovic, T. Gordon, V. F. Rafuse, and A. Prochazka, "Properties of Implanted Electrodes for Functional Electrical Stimulation," *Annals of Biomedical Engineering*, vol. 19, pp. 303–316, 1991.

[298] K. Singh, F. J. R. Richmond, and G. E. Loeb, "Recruitment properties of intramuscular and nerve-trunk stimulating electrodes," *IEEE Transactions on Rehabilitation Engineering*, vol. 8, no. 3, pp. 276–285, 2000.

[299] R. E. Burke, "Motor Units: Anatomy, Physiology, and Functional Organization," in *Comprehensive Physiology*. Hoboken, NJ, USA: John Wiley & Sons, Inc., jan 2011, no. 543.

[300] S. Joucla, B. Yvert, A. Glière, and B. Yvert, "Current approaches to model extracellular electrical neural microstimulation," *Frontiers in neuroscience*, vol. 8, no. February, pp. 1–12, 2014.

# List of publications

### International journal articles

1. **B. Mercadal**, P. T. Vernier and A. Ivorra, "Dependence of electroporation detection threshold on cell radius: an explanation to observations non compatible with Schwan's equation model", *Journal of Membrane Biology*, vol. 249, no. 5, pp. 663-676, 2016.

2. **B. Mercadal**, C. B. Arena, R. V. Davalos and A. Ivorra, "Avoiding nerve stimulation in irreversible electroporation: a numerical modeling study", *Physics in Medicine and Biology*, vol. 62, no. 20, pp. 8060-8079, 2017.

3. E. Ewertowska, **B. Mercadal**, V. Muñoz, A. Ivorra, M. Trujillo and E. Berjano, "Effect of applied voltage, duration and repetition frequency of RF pulses for pain relief on temperature spikes and electrical field: A computer modeling study", *International Journal of Hyperthermia*, vol. 34, no. 1, pp. 112-121, 2018.

4. Q. Castellví, **B. Mercadal**, X. Moll, D. Fontdevila, A. Andaluz and A. Ivorra, "Avoiding neuromuscular stimulation in liver irreversible electroporation using radiofrequency electric fields", *Physics in Medicine and Biology*, vol. 63, no. 3, p. 035027, 2018.

5. T. García-Sánchez, **B. Mercadal**, M. Polrot, A. Muscat, H. Sarnago, O. Lucía and L. M. Mir, "Succesful tumor electrochemotherapy using sine waves", *IEEE Transactions on Biomedical Engineering* [Accepted, July 2019]

6. **B. Mercadal**, J. M. Phillips, A. Eladly. and A. Ivorra "Innervation model for the study of the recruitment patterns in intramuscular electrical stimulation" [Under review].

7. **B. Mercadal**, N. B. White, K. Aycock, Q. Castellví, R.V Davalos and A. Ivorra, "Immediate and delayed cell death after IRE and H-FIRE treatments" [Under review].

8. **B. Mercadal**, R. Vicente and A. Ivorra "The potential role of electroporation in Pulsed Radiofrequency treatments for chronic pain: exposure to radiofrequency bursts causes an uptake of calcium but not of Yo-Pro-1" [In preparation]

## Conference Abstracts

1. **B.Mercadal**,C. B. Arena,R. V. Davalos and A. Ivorra, "Avoiding nerve stimulation in irreversible electroporation: a numerical modeling study," in *2nd World Congress on Electroporation and Pulsed Electric Fields in Biology, Medicine and Food & Environmental Technologies*, 2017.

2. **B.Mercadal**, R. Vicente and A. Ivorra, "Pulsed Radiofrequency for Chronic Pain: An Electroporation Mediated Calcium Signaling Process?", *62nd Annual Meeting of the Biophysical Society*, 2018.

3. **B. Mercadal**, R. Vicente and A. Ivorra, "The potential role of electroporation in Pulsed Radiofrequency treatments for chronic pain: exposure to radiofrequency bursts causes an uptake of calcium but not of Yo-Pro-1" in *3rd World Congress on Electroporation and Pulsed Electric Fields in Biology, Medicine and Food & Environmental Technologies*, 2019.

## Book Chapters

1. Q. Castellví, **B. Mercadal** and A. Ivorra, "Assessment of Electroporation by Electrical Impedance Methods," in *Handbook of Electroporation*, D. Miklavčič, Ed. Springer International Publishing, pp. 1–20, 2016.